

STRANGE PARTICLE PRODUCTION IN HIGH-ENERGY  
ELECTRON PROTON COLLISION

ZUKHAIMIRA BINTI ZOLKAPLI

FACULTY OF SCIENCE  
UNIVERSITY OF MALAYA  
KUALA LUMPUR

2013

STRANGE PARTICLE PRODUCTION IN HIGH-ENERGY  
ELECTRON PROTON COLLISION

ZUKHAIMIRA BINTI ZOLKAPLI

DISSERTATION SUBMITTED IN FULFILMENT OF THE  
REQUIREMENTS FOR THE DEGREE OF MASTER OF  
SCIENCE

DEPARTMENT OF PHYSICS  
FACULTY OF SCIENCE  
UNIVERSITY OF MALAYA  
KUALA LUMPUR

2013

UNIVERSITI MALAYA

**ORIGINAL LITERARY WORK DECLARATION**

Name of Candidate: ZUKHAIMIRA BINTI ZOLKAPLI (I.C/Passport No: 870222-04-5140)

Registration/Matric No: SGR090118

Name of Degree: MASTER OF SCIENCE (EXCEPT MATHEMATICS AND SCIENCE  
PHYLOSOPHY)

Title of Project Paper/Research Report/Dissertation/Thesis: STRANGE PARTICLE  
PRODUCTION IN HIGH-ENERGY ELECTRON PROTON COLLISION

Field of Study: PARTICLE PHYSICS

I do solemnly and sincerely declare that:

- (1) I am the sole author/writer of this Work;
- (2) This Work is original;
- (3) Any use of any work in which copyright exists was done by way of fair dealing and for permitted purposes and any excerpt of extract from, or reference to or reproduction of any copyright work has been disclosed expressly and sufficiently and the title of the Work and its authorship have been acknowledged in this Work;
- (4) I do not have any actual knowledge nor do I ought reasonably to know that the making of this Work constitutes an infringement of any copyright work;
- (5) I hereby assign all and every rights in the copyright to this Work to the University of Malaya ("UM"), who henceforth shall be owner of the copyright in this Work and that any reproduction or use in any form or by any means whatsoever is prohibited without the written consent of UM having been first had and obtained;
- (6) I am fully aware that if in the course of making this Work I have infringed any copyright whether intentionally or otherwise, I may be subject to legal action or any other action as may be determined by UM.

Candidate's Signature

Date

Subscribed and solemnly declared before,

Witness's Signature

Date

Name:

Designation:

# ABSTRACT

The strangeness total cross sections for  $ep$  neutral current deep inelastic scattering (DIS) have been measured using HERA-II data at a center-of-mass energy of  $\sqrt{s} = 318$  GeV with the ZEUS detector at HERA. The 2003 & 2007 running period data were used with an integrated luminosity of  $4.6 \text{ pb}^{-1}$  and compared with ARIADNE Monte Carlo (MC) predictions. The differential production cross-sections of  $\Lambda$ ,  $\bar{\Lambda}$ ,  $\Lambda + \bar{\Lambda}$  and  $K_s^0$  were measured in two different kinematic regions,  $Q_{DA}^2 > 25 \text{ GeV}^2$  for high  $Q^2$  DIS sample and  $5 < Q_{DA}^2 < 25 \text{ GeV}^2$  for low  $Q^2$  DIS sample. The differential cross sections were measured as functions of  $\eta(\Lambda, \bar{\Lambda}, K_s^0)$ ,  $p_T(\Lambda, \bar{\Lambda}, K_s^0)$  and  $Q^2$  in the DIS samples. The baryon-antibaryon production asymmetry, defined as  $\frac{(\Lambda - \bar{\Lambda})}{(\Lambda + \bar{\Lambda})}$ , and the baryon-meson ratio  $\frac{(\Lambda + \bar{\Lambda})}{K_s^0}$  were studied and the results were compared with ARIADNE MC prediction. The baryon production process is not well understood yet and therefore it relies much on phenomenological models like the Cluster and String Models. The study on baryon antibaryon rapidity correlation in  $ep$  collision can answer these problems. The tracking information from the Micro Vertex Detector (MVD) was used to observe the effect on the strange particles production when using this extra tracking information during the observation of  $\Lambda$  baryons and  $K_s^0$  mesons production at the ZEUS detector, in addition to the Central Tracking Detector.

# ABSTRAK

Jumlah keratan rentas kuark ganjil untuk perlanggaran tak kenyal tanpa cas antara  $e$  dan  $p$  telah diukur menggunakan data HERA-II pada tenaga pusat  $\sqrt{s} = 318$  GeV di mesin pengesan zarah ZEUS di dalam mesen pemecut zarah HERA. Data tahun 2003 & 2007 dengan nilai kilauan bersepadu  $4.6 \text{ pb}^{-1}$  telah digunakan dan keputusan akhir dibandingkan dengan simulasi Monte Carlo. Pengkamiran penghasilan keratan rentas  $\Lambda$ ,  $\bar{\Lambda}$ ,  $\Lambda + \bar{\Lambda}$  dan  $K_s^0$  telah diukur dalam dua rantau yang berbeza kinematik di mana  $Q_{DA}^2 > 25 \text{ GeV}^2$  untuk sampel perlanggaran tak kenyal dengan nilai  $Q^2$  tinggi dan  $5 < Q_{DA}^2 < 25 \text{ GeV}^2$  untuk sampel perlanggaran tak kenyal dengan nilai  $Q^2$  rendah. Dalam sampel perlanggaran tak kenyal, pengkamiran penghasilan keratan rentas ini telah diukur sebagai fungsi  $p_T(\Lambda, \bar{\Lambda}, K_s^0)$ ,  $\eta(\Lambda, \bar{\Lambda}, K_s^0)$  dan  $Q^2$ . Penghasilan asimetri baryon-antibaryon yang dedifinasikan sebagai  $\frac{(\Lambda - \bar{\Lambda})}{(\Lambda + \bar{\Lambda})}$ , dan nisbah penghasilan baryon kepada meson  $\frac{(\Lambda + \bar{\Lambda})}{K_s^0}$  dikaji, dan kemudian keputusan kajian dibandingkan dengan simulasi Monte Carlo ARIADNE. Proses penghasilan baryon masih tidak difahami dan hanya bergantung kepada model fenomenologi seperti Cluster Model dan String Model. Kajian terhadap korelasi kepesatan baryon terhadap antibaryon dalam perlanggaran  $ep$  boleh menjawab persoalan tersebut. Maklumat penjejakan dari Pengesan Mikro Vertex (MVD) telah digunakan untuk melihat kesan ke atas pengeluaran zarah pelik apabila menggunakan maklumat penjejak tambahan semasa pemerhatian baryons dan pengeluaran meson pada pengesan ZEUS, di samping Pengesan Penjejak Tengah (CTD).

# ACKNOWLEDGEMENT

**Bismillahirrahmanirrahim,**

Alhamdulillah. First and foremost, thanks to Allah SWT, who with His willing giving me the opportunity to complete this Master dissertation. This dissertation was prepared for the Department of Physics, Faculty of Science, University of Malaya, Kuala Lumpur, Malaysia. I dedicate this dissertation to my father, En. Zolkapli Bin Shafie and to my mother, Puan Rohena Binti Lajis, for their motivation, love and patience. I am deeply indebted to my supervisor Prof. Dr. Wan Ahmad Tajuddin Bin Wan Abdullah whose help, guide, always be patience , stimulating suggestions and encouragement helped me in all the time of research for and writing of this thesis. Next, thank you so much to ZEUSMal colleagues, Dr. Faridah Mohd Idris, Prof. Dr. Zainol Abidin Ibrahim, to all my family members, ZEUS Collaboration members, UM Physics Department, and others for their corporation, encouragement, constructive suggestion and full of support for the dissertation completion, from the beginning till the end. Thank you to University of Malaya for supporting my financial problem by giving me a fellowship during this period of studies. Also thanks to all my friends and everyone, that has been contributed by supporting my work and helps me during this dissertation progress till it is fully completed. Last but not least, my deepest thanks and appreciation to the special mate of mine, Muhammad Azri Bin Zahari. Thank you all.

# TABLE OF CONTENTS

Original Literary Work Declaration.....	ii
Abstract.....	iii
Abstrak.....	iv
Acknowledgement.....	v
Table of Contents.....	vi
List of Figures.....	x
List of Tables.....	xvii
List of Symbols and Abbreviation.....	xxi

## **Chapter 1: Introduction**

1.1 Thesis outline.....	4
-------------------------	---

## **Chapter 2: Physics Overview**

2.1 The Standard Model.....	6
2.1.1 Quarks.....	8
2.2 Quark Parton Model.....	10
2.3 Quantum Chromodynamics (QCD).....	12
2.4 Deep Inelastic Scattering (DIS).....	13
2.4.1 Electron-Proton Scattering.....	14
2.5 HERA Kinematics.....	15
2.6 Baryon Production.....	19
2.6.1 Strange Quark Production.....	22
2.7 Physics Motivation of the Thesis.....	23

### Chapter 3: Experimental Set-up

3.1	The HERA <i>ep</i> Collider.....	26
3.2	The ZEUS Detector.....	29
3.2.1	The Central Tracking detector (CTD).....	32
3.3	HERA-II.....	33
3.3.1	Micro Vertex Detector (MVD).....	34
3.4	ZEUS Analysis and Computing Model.....	38
3.4.1	Data Processing: the ZEUS Reconstruction Factory.....	39
3.4.2	ZEUS Analysis Facility (ZARAH).....	39
3.4.3	ZEUS Analysis.....	40
3.4.3.1	ORANGE.....	41
3.4.4	Monte Carlo and Events Simulation.....	42
3.4.4.1	The Lund String Fragmentation Model in JETSET.....	44
3.4.4.2	Event Generators.....	44
3.4.4.2.1	ARIADNE/DJANGO.....	44
3.5	Events Reconstruction & Selection.....	45
3.5.1	Events Reconstruction.....	45
3.5.1.1	Deep Inelastic Scattering (DIS) Events Reconstruction.....	45
3.5.2	Events Selection.....	47
3.5.2.1	Online Event Selection.....	47
3.5.2.2	Offline Event Selection.....	48
3.5.2.2.1	High $Q^2$ DIS.....	48
3.5.2.2.2	Low $Q^2$ DIS.....	50



## Chapter 4: Tracking Enhancement with the Micro Vertex Detector (MVD)

4.1	Introduction.....	51
4.2	V0lite's Reconstruction.....	52
4.2.1	Tracking.....	52
4.3	Signals to Background Ratio.....	53
4.4	Discussion and Conclusion.....	54

## Chapter 5: $\Lambda$ and $K^0$ Selection

5.1	Strange Particle Reconstruction.....	56
5.2	Track Reconstruction.....	57
5.3	Identification of $\Lambda \rightarrow p\pi^-$ ( $\bar{\Lambda} \rightarrow \bar{p}\pi^+$ ) candidates.....	57
5.4	Identification of $K_s^0 \rightarrow \pi^+\pi^-$ candidates.....	63
5.5	Efficiency, Purity and Acceptance.....	66

## Chapter 6: Results and Discussion

6.1	Total Cross-Sections.....	68
6.2	Differential Cross-Sections.....	71
6.2.1	$5 < Q_{DA}^2 < 25 \text{ GeV}^2$ .....	71
6.2.1.1	Inclusive $\Lambda$ baryon cross-sections in bins of $Q^2$ , $p_T(\Lambda)$ and $\eta(\Lambda)$ .....	72
6.2.1.2	Inclusive $\bar{\Lambda}$ baryon cross-sections in bins of $Q^2$ , $p_T(\bar{\Lambda})$ and $\eta(\bar{\Lambda})$ .....	75
6.2.1.3	Inclusive $\Lambda + \bar{\Lambda}$ baryon cross-sections in bins of $Q^2$ , $p_T(\Lambda + \bar{\Lambda})$ and $\eta(\Lambda + \bar{\Lambda})$ .....	78
6.2.1.4	Inclusive $K_s^0$ meson cross-sections in bins of $Q^2$ , $p_T(K_s^0)$ and $\eta(K_s^0)$ .....	81
6.2.2	$Q_{DA}^2 > 25 \text{ GeV}^2$ .....	84

6.2.2.1 Inclusive $\Lambda$ baryon cross-sections in bins of $Q^2$ , $p_T(\Lambda)$ and $\eta(\Lambda)$ .....	85
6.2.2.2 Inclusive $\bar{\Lambda}$ baryon cross-sections in bins of $Q^2$ , $p_T(\bar{\Lambda})$ and $\eta(\bar{\Lambda})$ .....	88
6.2.2.3 Inclusive $\Lambda + \bar{\Lambda}$ baryon cross-sections in bins of $Q^2$ , $p_T(\Lambda + \bar{\Lambda})$ and $\eta(\Lambda + \bar{\Lambda})$ .....	91
6.2.2.4 Inclusive $K_s^0$ meson cross-sections in bins of $Q^2$ , $p_T(K_s^0)$ and $\eta(K_s^0)$ .....	94
6.3 Baryon-to-Antibaryon Production Asymmetry.....	97
6.3.1 Low $Q^2$ DIS Events ( $5 < Q_{DA}^2 < 25 \text{ GeV}^2$ ).....	99
6.3.2 High $Q^2$ DIS Events ( $Q_{DA}^2 > 25 \text{ GeV}^2$ ).....	101
6.4 Baryon-to-Meson Ratio.....	103
6.4.1 Low $Q^2$ DIS Events ( $5 < Q_{DA}^2 < 25 \text{ GeV}^2$ ).....	106
6.4.2 High $Q^2$ DIS Events ( $Q_{DA}^2 > 25 \text{ GeV}^2$ ).....	107
6.5 Baryon Antibaryon Rapidity Correlations.....	108
6.5.1 Rapidity Correlation.....	109
6.5.2 Events Selection and Strangeness Production.....	110
6.5.3 Results and Discussion.....	111
6.5.4 Conclusion.....	115
<b>Chapter 7: Conclusion.....</b>	<b>116</b>
<b>Bibliography.....</b>	<b>122</b>

# LIST OF FIGURES

**Figure 1:** Flow chart of the elementary particles studies.

**Figure 2.1:** The fundamental particles of the Standard Model.

**Figure 2.2:** Hierarchy of the quarks.

**Figure 2.3:** Quantum Chromodynamics process.

**Figure 2.4:** Lowest order Feynman diagrams for Charged Current and Neutral Current Deep Inelastic Scattering (DIS)

**Figure 2.5:** Feynman diagrams for a Neutral Current DIS collisions. a) The 4-vectors of incoming and outgoing particles. b) The Lorentz invariant scalar defining the events.

**Figure 2.6:** The simulated picture of Neutral Current and Charge Current process in Deep Inelastic electron-proton scattering in HERA.

**Figure 2.7:** String fragmentation in  $x-t$  space.

**Figure 2.8:** If a vertex pair  $q_2 \bar{q}_2$  is produced inside a colour fluctuation region spanned by  $q_1 \bar{q}_1$ , an effective diquark-antidiquark pair has “popped out” in a stepwise manner. The model allows for several breakups in the colour fluctuation region, creating one or some mesons among the antibaryon and baryon, as shown to the left.

**Figure 2.9:** A popcorn example with two curtain quark pairs.

**Figure 2.10:** Possible mechanism of the strange quark production.

**Figure 3.1:** Flow in the data processing process in High Energy Physics Experiments.

**Figure 3.2:** The data from HERA was stored here.

**Figure 3.3:** The HERA and PETRA accelerator aerial view at the DESY campus in Hamburg, Germany. HERA was at 15-30 m underground with circumference 6.3 km.

**Figure 3.4:** The HERA collider with the four experiments H1, ZEUS, HERMES and HERA-B.

**Figure 3.5:** A small segment of the HERA tunnel. The proton beam is travelling in the large vacuum tube in the middle to the right while the electron beam tube is below that.

**Figure 3.6:** Cutaway of the ZEUS detector

**Figure 3.7:** Cross section of the ZEUS detector in the vertical plane, side view.

**Figure 3.8:** Cross section of the ZEUS detector in the vertical plane, top view.

**Figure 3.9:** Cross section in transverse plane containing the nominal interaction point.

**Figure 3.10:** The ZEUS coordinate system.

**Figure 3.11:** Integrated luminosity collected by ZEUS for the 1993-2000 and 2002-2007 periods, shown separately for each year. The plots are taken from [57]

**Figure 3.12:** The ZEUS Micro Vertex Detector (MVD)

**Figure 3.13:** a) A section through the barrel MVD, showing the arrangement around the beam-pipe of each the MVD ladders. b) A photograph of one half of the MVD, showing the barrel ladders, one half of each of the forward “wheels” and the cables and services [10].

**Figure 3.14:** Flow diagram of event analysis in the ZEUS detector. Simulated and actual events were run concurrent and compared to extract correction factor from pQCD calculation.

**Figure 3.15:** The ZEUS analysis environment

**Figure 4.1:** Hadronic decay modes of  $\Lambda$

**Figure 5.1:** The  $\Lambda$ ,  $\bar{\Lambda}$  and  $\Lambda + \bar{\Lambda}$  invariant mass distribution for the high  $Q^2$  DIS events. Histograms on the left side represent the invariant mass plot for ZEUS data where the solid curve represents the fit of a Gaussian for the signal combined to a second order polynomial function for the background. The MC is normalized to the data and represents by the red line while the pulse represents the ZEUS data, is shows by the histograms on the right side.

**Figure 5.2:** The  $\Lambda$ ,  $\bar{\Lambda}$  and  $\Lambda + \bar{\Lambda}$  invariant mass distribution for the low  $Q^2$  DIS events. Histograms on the left side represent the invariant mass plot for ZEUS data where the solid curve represents the fit of a Gaussian for the signal combined to a second order polynomial function for the background. The MC is normalized to the data and represents by the red line while the pulse represents the ZEUS data, is shows by the histograms on the right side.

**Figure 5.3:** The  $K_s^0$  mass distribution for the high  $Q^2$  DIS events. The histogram on the left side represents the invariant mass plot for ZEUS data where the solid curve represents the fit of a Gaussian for the signal combined with a second order polynomial function for the background. The MC is normalized to the data and represents by the red line while the pulse represents the ZEUS data, is shows by the histograms on the right side.

**Figure 5.4:** The  $K_s^0$  mass distribution for the low  $Q^2$  DIS events. The histogram on the left side represents the invariant mass plot for ZEUS data where the solid curve represents the fit of a Gaussian for the signal combined with a second order polynomial function for the background. The MC is normalized to the data and represents by the red

line while the pulse represents the ZEUS data, is shown by the histograms on the right side.

**Figure 6.1:** Differential cross-sections for  $\Lambda$  production in low  $Q^2$  DIS events with  $5 < Q_{DA}^2 < 25 \text{ GeV}^2$  as a function of  $Q^2$ ,  $p_T(\Lambda)$  and  $\eta(\Lambda)$ . 2003 & 2007 HERA-II data and ARIADNE MC are shown.

**Figure 6.2:** Differential cross-sections for  $\bar{\Lambda}$  production in low  $Q^2$  DIS events with  $5 < Q_{DA}^2 < 25 \text{ GeV}^2$  as a function of  $Q^2$ ,  $p_T(\bar{\Lambda})$  and  $\eta(\bar{\Lambda})$ . 2003 & 2007 HERA-II data and ARIADNE MC are shown.

**Figure 6.3:** Differential cross-sections for  $\Lambda + \bar{\Lambda}$  production in low  $Q^2$  DIS events with  $5 < Q^2 < 25 \text{ GeV}^2$  as a function of  $Q^2$ ,  $p_T(\Lambda + \bar{\Lambda})$  and  $\eta(\Lambda + \bar{\Lambda})$ . 2003 & 2007 HERA-II data and ARIADNE MC are shown.

**Figure 6.4:** Differential cross-sections for  $K_s^0$  production in low  $Q^2$  DIS events with  $5 < Q_{DA}^2 < 25 \text{ GeV}^2$  as a function of  $Q^2$ ,  $p_T(K_s^0)$  and  $\eta(K_s^0)$ . 2003 & 2007 HERA-II data and ARIADNE MC are shown.

**Figure 6.5:** Differential cross-sections for  $\Lambda$  production in high- $Q^2$  DIS events with  $Q_{DA}^2 > 25 \text{ GeV}^2$  as a function of  $Q^2$ ,  $p_T(\Lambda)$  and  $\eta(\Lambda)$ . 2003 & 2007 HERA-II data and ARIADNE MC are shown.

**Figure 6.6:** Differential cross-sections for  $\bar{\Lambda}$  production in high  $Q^2$  DIS events with  $Q_{DA}^2 > 25 \text{ GeV}^2$  as a function of  $Q^2$ ,  $p_T(\bar{\Lambda})$  and  $\eta(\bar{\Lambda})$ . 2003 & 2007 HERA-II data and ARIADNE MC are shown.

**Figure 6.7:** Differential cross-sections for  $\Lambda + \bar{\Lambda}$  production in high  $Q^2$  DIS events with  $Q_{DA}^2 > 25 \text{ GeV}^2$  as a function of  $Q^2$ ,  $p_T(\Lambda + \bar{\Lambda})$  and  $\eta(\Lambda + \bar{\Lambda})$ . 2003 & 2007 HERA-II data and ARIADNE MC are shown.

**Figure 6.8:** Differential cross-sections for  $K_s^0$  production in high  $Q^2$  DIS events with  $Q_{DA}^2 > 25 \text{ GeV}^2$  as a function of  $Q^2$ ,  $p_T(K_s^0)$  and  $\eta(K_s^0)$ . 2003 & 2007 HERA-II data and ARIADNE MC are shown.

**Figure 6.9:** The  $\Lambda - \bar{\Lambda}$  asymmetry for ZEUS 2003 & 2007 data and ARIADNE Monte Carlo samples as a function of  $\eta$ ,  $Q^2$  and  $P_T$  in the laboratory frame for Low  $Q^2$  DIS events with  $5 < Q_{DA}^2 < 25 \text{ GeV}^2$ . The  $N(\Lambda)$ ,  $N(\bar{\Lambda})$  is the number of  $\Lambda$  and  $\bar{\Lambda}$  baryons, respectively. The error bars represent the statistical errors for the measurements.

**Figure 6.10:** The  $\Lambda - \bar{\Lambda}$  asymmetry for ZEUS 2003 & 2007 data and ARIADNE Monte Carlo samples as a function of  $\eta$ ,  $Q^2$  and  $P_T$  in the laboratory frame for Low  $Q^2$  DIS events with  $5 < Q_{DA}^2 < 25 \text{ GeV}^2$ . The  $\sigma(\Lambda)$ ,  $\sigma(\bar{\Lambda})$  is the differential cross section of  $\Lambda$  and  $\bar{\Lambda}$  baryons, respectively. The error bars represent the statistical errors for the measurements.

**Figure 6.11:** The  $\Lambda - \bar{\Lambda}$  asymmetry for ZEUS 2003 & 2007 data and ARIADNE Monte Carlo samples as a function of  $\eta$ ,  $Q^2$  and  $P_T$  in the laboratory frame for High  $Q^2$  DIS events with  $Q_{DA}^2 > 25 \text{ GeV}^2$ . The  $N(\Lambda)$ ,  $N(\bar{\Lambda})$  is the number of  $\Lambda$  and  $\bar{\Lambda}$  baryons, respectively. The error bars represent the statistical errors for the measurements.

**Figure 6.12:** The  $\Lambda - \bar{\Lambda}$  asymmetry for ZEUS 2003 & 2007 data and ARIADNE Monte Carlo samples as a function of  $\eta$ ,  $Q^2$  and  $P_T$  in the laboratory frame for High

$Q^2$  DIS events with  $Q_{DA}^2 > 25 \text{ GeV}^2$ . The  $\sigma(\Lambda)$ ,  $\sigma(\bar{\Lambda})$  is the differential cross section of  $\Lambda$  and  $\bar{\Lambda}$  baryons, respectively. The error bars represent the statistical errors for the measurements.

**Figure 6.13:** The  $(\Lambda + \bar{\Lambda})/K_s^0$  ratio for ZEUS 2003 & 2007 data and ARIADNE Monte Carlo samples as a function of  $\eta$ ,  $Q^2$  and  $P_T$  in the laboratory frame for Low  $Q^2$  DIS events with  $5 < Q_{DA}^2 < 25 \text{ GeV}^2$ . The  $\sigma(\Lambda)$ ,  $\sigma(\bar{\Lambda})$  and  $\sigma(K_s^0)$  is the differential cross section of  $\Lambda$  and  $\bar{\Lambda}$  baryons, and  $K_s^0$  meson respectively. The error bars represent the statistical errors for the measurements.

**Figure 6.14:** The  $(\Lambda + \bar{\Lambda})/K_s^0$  ratio for ZEUS 2003 & 2007 data and ARIADNE Monte Carlo samples as a function of  $\eta$ ,  $Q^2$  and  $P_T$  in the laboratory frame for High  $Q^2$  DIS events with  $Q_{DA}^2 > 25 \text{ GeV}^2$ . The  $\sigma(\Lambda)$ ,  $\sigma(\bar{\Lambda})$  and  $\sigma(K_s^0)$  is the differential cross section of  $\Lambda$  and  $\bar{\Lambda}$  baryons, and  $K_s^0$  meson respectively. The error bars represent the statistical errors for the measurements.

**Figure 6.15:** An illustration of the particle pair correlations proposed in the string model due to sharing of a common string break-up. The dotted line represents a string and the solid curves describe the development of a  $q\bar{q}$  or  $D\bar{D}$  pair created at some break-up points in a string. Here  $q$ ,  $\bar{q}$ ,  $D$ ,  $\bar{D}$ ,  $B$ ,  $\bar{B}$  and  $M$  denote a quark, antiquark, diquark, antidiquark, baryon, antibaryon and meson, respectively. Figure (a) shows the correlation between a baryon-antibaryon pair. The figures (b) and (c) show such correlation for baryon-meson and meson-meson pairs, respectively [42].

**Figure 6.16:** The  $\Lambda\bar{\Lambda}$  correlation for ZEUS 2003 & 2007 data compared to the ARIADNE data. The black triangles represent the data while the red circles for the MC. The figure clearly shows correlation between baryon and its antiparticle, antibaryon.



**Figure 6.17:** The  $\Lambda\bar{\Lambda}$  rapidity distribution for the Deep Inelastic Scattering events. The MC is normalized to the data and represents by the line while the pulse represents the ZEUS data.  $\Lambda\bar{\Lambda}$  clearly correlated at low rapidity difference.

**Figure 6.18:** Rapidity distributions for lambda vs antilambda. The upper figures represent the distribution for ZEUS 2003 & 2007 data sample while the below figures for ARIADNE MC data sample.

# LIST OF TABLES

**Table 1:** Classification of the elementary particles. The fermions constitute matter. The bosons are the force carriers.

**Table 2.1:** The Fundamental Forces in Nature.

**Table 4.1:** The signal to background ratio for the MVD+CTD compared to the CTD. The performance of the MVD+CTD detector is better than the CTD only detector.

**Table 5.1:** Properties of the strange particles.

**Table 5.2:** The number of reconstructed strange particles at the detector level in HERA-II.

**Table 5.3:** The  $\Lambda$ ,  $\bar{\Lambda}$ ,  $\Lambda + \bar{\Lambda}$  and  $K_s^0$  reconstruction acceptances for high  $Q^2$  DIS and low  $Q^2$  DIS events.

**Table 6.1:** Differential  $\Lambda$  baryon cross-sections,  $d\sigma$ , measured as a function of  $Q^2$ ,  $p_T(\Lambda)$  and  $\eta(\Lambda)$  in data. The number of  $\Lambda$  baryons,  $N_\Lambda$  and the differential cross section  $d\sigma$  are listed for each range of  $Q^2$ ,  $p_T(\Lambda)$  and  $\eta(\Lambda)$ .

**Table 6.2:** Differential  $\Lambda$  baryon cross-sections,  $d\sigma$ , measured as a function of  $Q^2$ ,  $p_T(\Lambda)$  and  $\eta(\Lambda)$  in MC. The number of  $\Lambda$  baryons,  $N_\Lambda$  and the differential cross section  $d\sigma$  are listed for each range of  $Q^2$ ,  $p_T(\Lambda)$  and  $\eta(\Lambda)$ .

**Table 6.3:** Differential  $\bar{\Lambda}$  baryon cross-sections,  $d\sigma$ , measured as a function of  $Q^2$ ,  $p_T(\bar{\Lambda})$  and  $\eta(\bar{\Lambda})$  in data. The number of  $\bar{\Lambda}$  baryons,  $N_{\bar{\Lambda}}$  and the differential cross section  $d\sigma$  are listed for each range of  $Q^2$ ,  $p_T(\bar{\Lambda})$  and  $\eta(\bar{\Lambda})$ .

**Table 6.4:** Differential  $\bar{\Lambda}$  baryon cross-sections,  $d\sigma$ , measured as a function of  $Q^2$ ,  $p_T(\bar{\Lambda})$  and  $\eta(\bar{\Lambda})$  in MC. The number of  $\bar{\Lambda}$  baryons,  $N_{\bar{\Lambda}}$  and the differential cross section  $d\sigma$  are listed for each range of  $Q^2$ ,  $p_T(\bar{\Lambda})$  and  $\eta(\bar{\Lambda})$ .

**Table 6.5:** Differential  $\Lambda + \bar{\Lambda}$  baryon cross-sections,  $d\sigma$ , measured as a function of  $Q^2$ ,  $p_T(\Lambda + \bar{\Lambda})$  and  $\eta(\Lambda + \bar{\Lambda})$  in data. The number of  $\Lambda + \bar{\Lambda}$  baryons,  $N_{\Lambda + \bar{\Lambda}}$  and the differential cross section  $d\sigma$  are listed for each range of  $Q^2$ ,  $p_T(\Lambda + \bar{\Lambda})$  and  $\eta(\Lambda + \bar{\Lambda})$ .

**Table 6.6:** Differential  $\Lambda + \bar{\Lambda}$  baryon cross-sections,  $d\sigma$ , measured as a function of  $Q^2$ ,  $p_T(\Lambda + \bar{\Lambda})$  and  $\eta(\Lambda + \bar{\Lambda})$  in MC. The number of  $\Lambda + \bar{\Lambda}$  baryons,  $N_{\Lambda + \bar{\Lambda}}$  and the differential cross section  $d\sigma$  are listed for each range of  $Q^2$ ,  $p_T(\Lambda + \bar{\Lambda})$  and  $\eta(\Lambda + \bar{\Lambda})$ .

**Table 6.7:** Differential  $K_s^0$  meson cross-sections,  $d\sigma$ , measured as a function of  $Q^2$ ,  $p_T(K_s^0)$  and  $\eta(K_s^0)$  in data. The number of  $K_s^0$  meson,  $N_{K_s^0}$  and the differential cross section  $d\sigma$  are listed for each range of  $Q^2$ ,  $p_T(K_s^0)$  and  $\eta(K_s^0)$ .

**Table 6.8:** Differential  $K_s^0$  meson cross-sections,  $d\sigma$ , measured as a function of  $Q^2$ ,  $p_T(K_s^0)$  and  $\eta(K_s^0)$  in MC. The number of  $K_s^0$  meson,  $N_{K_s^0}$  and the differential cross section  $d\sigma$  are listed for each range of  $Q^2$ ,  $p_T(K_s^0)$  and  $\eta(K_s^0)$ .

**Table 6.9:** Differential  $\Lambda$  baryon cross section,  $d\sigma$ , measured as a function of  $Q^2$ ,  $p_T(\Lambda)$  and  $\eta(\Lambda)$  in data. The number of  $\Lambda$  baryons,  $N_\Lambda$  and the differential cross section  $d\sigma$  are listed for each range of  $Q^2$ ,  $p_T(\Lambda)$  and  $\eta(\Lambda)$ .

**Table 6.10:** Differential  $\Lambda$  baryon cross section,  $d\sigma$ , measured as a function of  $Q^2$ ,  $p_T(\Lambda)$  and  $\eta(\Lambda)$  in MC. The number of  $\Lambda$  baryons,  $N_\Lambda$  and the differential cross section  $d\sigma$  are listed for each range of  $Q^2$ ,  $p_T(\Lambda)$  and  $\eta(\Lambda)$ .

**Table 6.11:** Differential  $\bar{\Lambda}$  baryon cross section,  $d\sigma$ , measured as a function of  $Q^2$ ,  $p_T(\bar{\Lambda})$  and  $\eta(\bar{\Lambda})$  in data. The number of  $\bar{\Lambda}$  baryons,  $N_{\bar{\Lambda}}$  and the differential cross section  $d\sigma$  are listed for each range of  $Q^2$ ,  $p_T(\bar{\Lambda})$  and  $\eta(\bar{\Lambda})$ .

**Table 6.12:** Differential  $\bar{\Lambda}$  baryon cross section,  $d\sigma$ , measured as a function of  $Q^2$ ,  $p_T(\bar{\Lambda})$  and  $\eta(\bar{\Lambda})$  in MC. The number of  $\bar{\Lambda}$  baryons,  $N_{\bar{\Lambda}}$  and the differential cross section  $d\sigma$  are listed for each range of  $Q^2$ ,  $p_T(\bar{\Lambda})$  and  $\eta(\bar{\Lambda})$ .

**Table 6.13:** Differential  $\Lambda + \bar{\Lambda}$  baryon cross section,  $d\sigma$ , measured as a function of  $Q^2$ ,  $p_T(\Lambda + \bar{\Lambda})$  and  $\eta(\Lambda + \bar{\Lambda})$  in data. The number of  $\Lambda + \bar{\Lambda}$  baryons,  $N_{\Lambda + \bar{\Lambda}}$  and the differential cross section  $d\sigma$  are listed for each range of  $Q^2$ ,  $p_T(\Lambda + \bar{\Lambda})$  and  $\eta(\Lambda + \bar{\Lambda})$ .

**Table 6.14:** Differential  $\Lambda + \bar{\Lambda}$  baryon cross section,  $d\sigma$ , measured as a function of  $Q^2$ ,  $p_T(\Lambda + \bar{\Lambda})$  and  $\eta(\Lambda + \bar{\Lambda})$  in MC. The number of  $\Lambda + \bar{\Lambda}$  baryons,  $N_{\Lambda + \bar{\Lambda}}$  and the differential cross section  $d\sigma$  are listed for each range of  $Q^2$ ,  $p_T(\Lambda + \bar{\Lambda})$  and  $\eta(\Lambda + \bar{\Lambda})$ .

**Table 6.15:** Differential  $K_s^0$  meson cross section,  $d\sigma$ , measured as a function of  $Q^2$ ,  $p_T(K_s^0)$  and  $\eta(K_s^0)$  in data. The number of  $K_s^0$  meson,  $N_{K_s^0}$  and the differential cross section  $d\sigma$  are listed for each range of  $Q^2$ ,  $p_T(K_s^0)$  and  $\eta(K_s^0)$ .

**Table 6.16:** Differential  $K_s^0$  meson cross section,  $d\sigma$ , measured as a function of  $Q^2$ ,  $p_T(K_s^0)$  and  $\eta(K_s^0)$  in MC. The number of  $K_s^0$  meson,  $N_{K_s^0}$  and the differential cross section  $d\sigma$  are listed for each range of  $Q^2$ ,  $p_T(K_s^0)$  and  $\eta(K_s^0)$ .

**Table 6.17:** The average  $\Lambda$  to  $K_s^0$  production ratio for HERA-II data compared to the previous HERA-I data. The statistical uncertainties are shown for the data.

**Table 6.18:** The number of  $\Lambda$  and  $\bar{\Lambda}$  for ZEUS 2003 & 2007 data.

**Table 6.19:** The number of  $\Lambda$  and  $\bar{\Lambda}$  for ARIADNE.

# LIST OF SYMBOLS AND ABBREVIATIONS

<b>HERA</b>	Hadron Electron Ring Accelerator
<b>DESY</b>	Deutsches Elektronen Synchrotron
<b>H1</b>	H1 Detector
<b>ZEUS</b>	ZEUS Detector
<b>HERMES</b>	HERMES Detector
<b>HERA-B</b>	HERA-B Detector
<b>HERA-II</b>	Hadron Electron Ring Accelerator-II
<b>PETRA</b>	Positron-Electron Tandem Ring Accelerator
<b>SM</b>	Standard Model
<b>DIS</b>	Deep Inelastic Scattering
<b>MVD</b>	Micro Vertex Detector
<b>QFD</b>	Quantum Flavor Dynamics
<b>QCD</b>	Quantum Chromodynamics
<b>QED</b>	Quantum Electrodynamics
<b>SLAC</b>	Stanford Linear Accelerator Center
<b>PDFs</b>	Parton Distribution Function

<b>PDF</b>	Parton Density Function
<b>CC</b>	Charged Current
<b>NC</b>	Neutral Current
$\Lambda$	Lambda Baryon
$\bar{\Lambda}$	Anti-Lambda Baryon
$K_s^0$	Kaon-Short
$p$	Proton
$\pi^+$	Pion Plus
$\pi^-$	Pion Minus
$Z^0$	$Z^0$ Gauge Boson
$W^\pm$	$W^\pm$ Gauge Boson
$e^-$	Electron
$e^+$	Positron
$\gamma$	Photon
$B$	B Meson
$\bar{B}$	Anti-B Meson
$q$	Quark
$\bar{q}$	Anti-Quark

$Q^2$	The square of the four-momentum transfer $q$ between the incoming electron and the scattered electron.
<b>CP</b>	Charge Parity
<b>CAL</b>	Uranium Scintillator Calorimeter
<b>UCAL</b>	Uranium-Scintillator Calorimeter
<b>FCAL</b>	Forward Uranium Scintillator Calorimeter
<b>BCAL</b>	Barrel Uranium Scintillator Calorimeter
<b>RCAL</b>	Rear Uranium Scintillator Calorimeter
<b>VXD</b>	Vertex Detector
<b>CTD</b>	Central Tracking Detector
<b>FTD</b>	Forward Tracking Detector
<b>RTD</b>	Rear Tracking Detector
<b>SRTD</b>	Small-angle Rear Tracking Detector
<b>TRD</b>	Transition Radiation Detector
<b>MVD</b>	Silicon Micro Vertex Detector
<b>FMVD</b>	Forward Micro Vertex Detector
<b>BMVD</b>	Barrel Micro Vertex Detector
<b>FMUI</b>	Forward Muon Detector (located inside)
<b>BMUI</b>	Barrel Muon Detector (located inside)
<b>RMUI</b>	Rear Muon Detector (located inside)



<b>FMUO</b>	Forward Muon Detector (located outside)
<b>BMUO</b>	Barrel Muon Detector (located outside)
<b>RMUO</b>	Rear Muon Detector (located outside)
<b>STT</b>	Straw Tube Tracker
<b>DCA</b>	Distance to the Closest Approached
<b>JB</b>	Jacquet-Blondel
<b>DA</b>	Double Angle
<b>MC</b>	Monte Carlo
<b>GEANT</b>	GEometry ANd Tracking
<b>VCTRAK</b>	V(XD)C(TD)TRA(C)K
<b>FORTTRAN</b>	FORmula TRANslation
<b>BN</b>	Baryon Number
<b>CP</b>	Charge Parity
<b>HERACLES</b>	NC and CC <i>ep</i> interactions (using parameterizations of structure functions or parton densities) with radiative corrections: single photon emission from the lepton line, self-energy corrections and the complete set of one-loop weak corrections can be included <a href="#">[50]</a> .
<b>DJANGO</b>	Interface between HERACLES (QED corrections to order $\alpha_{QED}$ ) and LEPTO/ARIADNE (QCD matrix elements and parton showers/colour dipole radiation) to give complete ep events <a href="#">[50]</a> .

<b>ARIADNE</b>	A program for simulation of QCD cascades implementing the color dipole model <a href="#">[50]</a> .
<b>LEPTO</b>	Deep inelastic lepton-nucleon scattering based on LO electroweak cross sections (incl. lepton polarization), first order QCD matrix elements, parton showers and Lund hadronization giving complete events. Soft colour interaction model gives rapidity gap events <a href="#">[50]</a> .
<b>JETSET</b>	The Lund string model for hadronization of parton systems <a href="#">[50]</a> .
<b>LO</b>	Lowest Order
<b>ZTT</b>	ZEUS software track finding packages

# CHAPTER 1

## Introduction

In recent year's physicist have uncovered a lot of information about the Universe that surrounds us. This search has revealed that, beyond the evidence of our eyes, there is a seething world of tiny particles and messengers that pass between them, endlessly changing in energy, in space, and in time. A large new idea on the matter structure understanding was made by physicist when it was later found out that the atom was made up of of electrons, protons and neutrons.

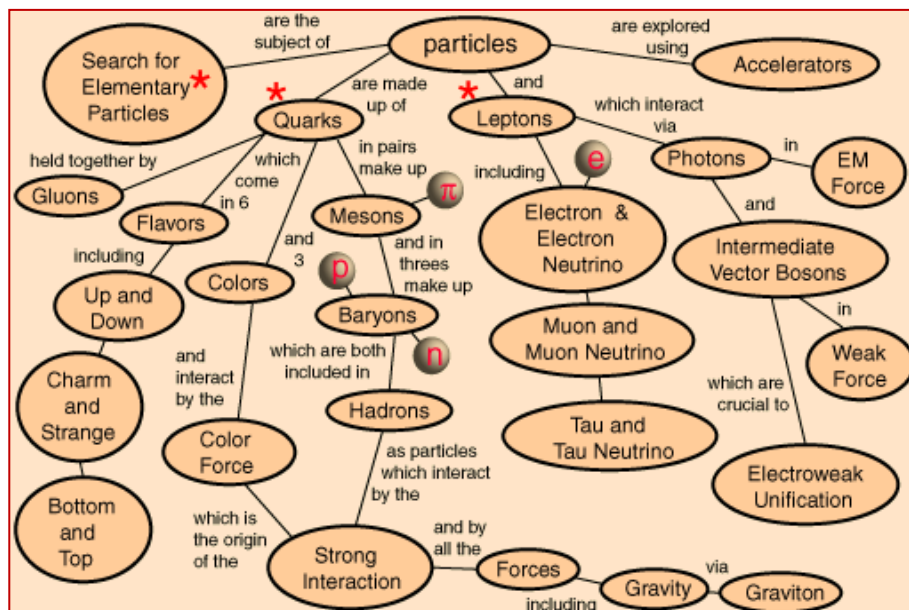


**Figure 1:** Flow chart of the elementary particles studies.

Particles are also the subject of searching for elementary particles. Particles are made up of quarks and leptons and were explored using particle accelerators and detected by particle detectors. Quarks held together by gluons and come in 6 flavors

including up, down, charm, strange, top and bottom and 3 colours and interact by the colour force which is the origin of the strong interaction. Quarks in pairs make up mesons and in threes make up baryons, which both are included in hadrons as particles and interact by the strong interaction. Leptons including electron, electron neutrino, muon, muon neutrino, tau and tau neutrino, interact via photons in electromagnetic force and intermediate vector bosons in weak force, which are crucial to electroweak unification.

The Standard Model is the most advanced quantum theory known yet which describes how elementary particles interact. The Standard Model Theory (SM) of particle physics provides a framework for explaining chemistry and nuclear physics (low energy process). It additionally provides an explanation for sub-nuclear physics and some aspects of cosmology in the earliest moments of the universe (high energy process). It is a simple and comprehensive theory that explains all the hundreds of particles and complex interactions with only 6 quarks (up, down, strange, charmed, top and bottom), 6 leptons (electron, muon, tau, electron neutrino, muon neutrino and tau neutrino) and 4 gauge bosons that act as the force carrier particles (photon, gluon,  $Z^0$  and  $W^\pm$ ). The Standard Model also describes the strong, weak and electromagnetic fundamental interactions, using mediating gauge bosons. All the known matter particles are composites of quarks and leptons, and they interact by exchanging force carrier particles. The Standard Model has been confirmed experimentally to the great accuracies. But it does not explain everything. For example, gravity is not included in the Standard Model. A classification of elementary particles is given in Table 1.

FERMIONS					
Leptons			Quarks		
$\nu_e$ (e-neutrino)	$\nu_\mu$ ( $\mu$ -neutrino)	$\nu_\tau$ ( $\tau$ -neutrino)	<b>u</b> (up)	<b>c</b> (charm)	<b>t</b> (top)
<b>e</b> (electron)	$\mu$ (muon)	$\tau$ (tau)	<b>d</b> (down)	<b>s</b> (strange)	<b>b</b> (beauty)
BOSONS					
Forces			Carrier particle		
Electromagnetic			$\gamma$ (photon)		
Weak nuclear			$W^+, W^-, Z^0$ (gauge bosons)		
Strong nuclear			<b>g</b> (gluon)		

**Table 1:** Classification of the elementary particles. The fermions constitute matter. The bosons are the force carriers.

Electromagnetic force is the force between 2 mass with electromagnetic charges, which attracts and/or repels each other. The strong force is the force that binds 2 or more protons against electric repulsion and forms a nucleus. The weak force is the force that causes the nuclear fission. Gravity is the force between 2 matters with mass, which attracts each other.

The first experiments which have been made in unravelling the structure of matter during the last century was the  $\alpha$ -particle scattering experiments on a metal foil, carried out by Ernest Rutherford in 1911. This experiment relies on the very basic concept that the angular and energy distribution of the scattered point-like test particles are related to and can reflect the inner structure of the target. The significance of this experiment is that it clearly showed that the atom has a hard compact component, the atomic nucleus. Many years later, nuclei were found to be composed of protons and neutrons. This brings our knowledge of the elementary block of matter from atom to proton and neutron.

To look inside the atomic nucleus requires special types of microscope known a particle detector. The Heisenberg uncertainty relationship tells us that higher energy is required in order to probe smaller size of matter. By the use of electric fields,

electrically charged particles such as electrons or protons were accelerated to within the fraction of the speed of light and then smashed into targets of matter or head on into one another. The results of such collisions can reveal the deep structure of matter. They show not only the quarks that seed the atomic nucleus, but have also revealed exotic forms of matter with weird names - strange, charm, bottom, and top – and heavier forms of the electron, known as muon and tau.

The Hadron Electron Ring Accelerator, HERA was the first and so far the only electron-proton collider in the world situated at DESY in Hamburg, Germany. The HERA project has been in operation since 1992 with two general purpose detectors, H1 and ZEUS, and two dedicated purpose detectors, HERMES and HERA-B. The latter two experiments are the fixed targets experiments that were started in 1995 and 2002.

During its operation, the HERA collider produced two types of data, HERA-I and HERA-II that runned in different periods. The HERA-I data were collected during the running period from 1992 to 2000 while the HERA-II data were collected during the running period from 2003 to 2007. This thesis is based on the HERA-II data, selected by the ZEUS detector at HERA collider with a total integrated luminosity of  $4.60\text{pb}^{-1}$ , during the running period between 2003 & 2007.

The objectives of this thesis are (i) to study the correlation on baryon-antibaryon production in  $ep$  collision based on the LUND string model and (ii) to study the effect of using Micro Vertex Detector (MVD) tracking information to find tracks in addition to the Central Tracking Detector (CTD) for the searches of strange particles  $\Lambda$ ,  $\bar{\Lambda}$  and  $K_s^0$ .

## 1.1 THESIS OUTLINE

The thesis was arranged as follows. An introduction is given in this chapter. The second chapter gives an overview of the physics concept which describes all the processes that happened during the particle collisions. The HERA physics, strangeness physics, particle correlation physics and the motivations of the thesis are presented in this chapter, as well as describing the quark parton model and models to simulate strange quarks production in DIS and photoproduction events. Chapter 3 goes on with the explanation about the experimental set-up, the descriptions of the HERA collider, the ZEUS detector and its components that are relevant to the analysis, the Micro Vertex detector (MVD) components, offline selection of events, describing the triggers and cuts used in the particle reconstruction, as well as a brief description of the Monte Carlo data sets used to compare the different sets of results. The fourth chapter reviews the usage and the effect of the Micro Vertex Detector in the production of strange particles  $\Lambda$ ,  $\bar{\Lambda}$  and  $K_s^0$ . The strange particle reconstruction, baryon characteristics and identification of  $\Lambda \rightarrow p\pi^-$ ,  $\bar{\Lambda} \rightarrow p\pi^+$  and  $K_s^0 \rightarrow \pi^-\pi^+$  candidates were discussed in Chapter 5. Chapter 6 discusses on the total cross-sections, differential cross-sections, baryon-to-antibaryon production asymmetry, baryon-to-meson ratio and the baryon antibaryon rapidity correlations in  $ep$  collision results of the measurement and the corresponding discussion and Chapter 7 concludes the thesis.

# CHAPTER 2

## Physics Overview

### 2.1 The Standard Model

The Standard Model of particle physics is a very successful theory to describe the fundamental constituents of matter and the interactions between them. As of right now, we know of 12 fundamental particles: six quarks and six leptons as shown in the Figure 2.1 below. There are currently hundreds of identified particles made from combinations of these twelve fundamental particles and scientists are still finding more.

Model of Elementary Particles									
			Three Generations of Matter(Fermions)						Force Carriers (Gauge Bosons)
			I	II	III				
Q u a r k s	(Name)	Electric Charge	Up u +2/3 3 ~ 5	Charm c +2/3 3 ~ 1350	Top/ Truth t +2/3 3 > 131000				
	(Symbol)	Number of Color Charges	Down d -1/3 3 ~ 9	Strange s -1/3 3 ~ 175	Bottom/ Beauty b -1/3 3 ~ 4500				
	Mass in MeV								
L e p t o n s	Electron Neutrino $\nu_e$ < .0000070	0	Muon Neutrino $\nu_\mu$ < .27	0	Tau Neutrino $\nu_\tau$ < 31				
	Electron e .511	-1	Muon $\mu$ 105.66	-1	Tau $\tau$ 1777.1				
						Photon $\gamma$ 0	0	Electro-magnetism	
						Gluon g 8 0	0	Strong Interactions	
						Z zero Z <sup>0</sup> 91187	0	Weak Interactions	
						W plus minus W <sup>±</sup> 80220	±1		

Figure 2.1: The fundamental particles of the Standard Model



	Messenger Particle(s) (Bosons)	Range	Acts On:
Gravity	Graviton (Hypothetical)	Indefinitely Long	All Particles
Weak Nuclear Force	W and Z	Short ( $>10^{-17}$ meters)	All Particles Except Photons
Electromagnetic Force	Photons	Indefinitely Long	All Particles with Electromagnetic Charge
Strong Nuclear Force	Gluons	Short ( $10^{-15}$ meters)	Quarks and Gluons

**Table 2.1:** The Fundamental Forces in Nature

According to the Standard Model, particles and forces are both manifestations of the underlying quantum fields. Since these fields can be seen as particles, we can say that all matter and forces are made of a few kinds of particles. The Standard Model predicts that there are three basic forces, and two families of matter. The forces include the electromagnetic force and the weak force (which can be seen as a unified electroweak force) and the strong force. They work over different ranges and have different strengths.

Gravity is the weakest but it has an infinite range. The electromagnetic force also has infinite range but it is many times stronger than gravity. The weak and strong forces are effective only over a short range and dominate only at the level of subatomic particles. The weak force is much stronger than gravity but it is indeed the weakest of the other three. The strong force is the strongest force among all the four fundamental interactions. Each of these forces is carried by particles, as shown in Table 2.1. Of these particles, only the gravitons have not yet been found, although most physicists are fairly confident that they will be.

The gravitational force, mediated by gravitons is the force of attraction between all masses in the universe, especially the attraction of the earth's mass for bodies near its surface. The electromagnetic interaction describes the quark-lepton interaction, and it is mediated by photons. The electromagnetic force and the weak force are unified into the electroweak force, described by the Quantum Flavor Dynamics (QFD). The weak interaction describes transition between quark or lepton generations, and it is mediated by vector bosons,  $W^\pm$  when the interaction involves a charge transfer, and  $Z^0$  when it is a neutral transfer. The Strong interactions are mediated by gluons and is responsible for the binding of quarks into hadrons and it is described by Quantum Chromodynamics (QCD) [18].

The Standard Model provides a quantum field theory of the first three forces, taking special relativity into account. Gravity is the odd force out, because there is no verified quantum theory of gravity. The quantum theory used to describe the micro world, and the general theory of relativity used to describe the macro world. No one has managed to make the two mathematically compatible in the context of the Standard Model.

### 2.1.1 Quarks

In the mid-1960s, Gell-Mann introduced the concept that point-like particles (“quarks”) existed inside the proton [13]. This idea was mainly based on the effort to describe the rich spectrum of meson and hadrons resonance that were discovered during the 1950s, which was interpreted as excited bound states of these point-like constituents.

Later, in 1968, new data from SLAC electron scattering experiments hinted that the proton was in fact built up out of point-like particles which physicist at that time called partons. The experiments proved that high-energy electrons have a large

probability of scattering with large energy transfer and into large angles. The existence and properties of quarks were first inferred from hadron spectroscopy by Gell-Mann and independently by Zweig in 1964 and the close correspondence between the experimentally observed hadrons and those predicted by the quark model remains one of the strongest reasons for the belief in the existence of quarks. Quarks and antiquarks are the particles which carry electric charge.

Since pions were first produced in the laboratory in the early 1950s, several hadrons then have been observed and all have zero or integer electric charges: 0,  $\pm 1$  or  $\pm 2$  in units of  $e$ , where  $e$  is the fundamental unit of electrical charge. They are all bound state of the fundamental spin  $\frac{1}{2}$  quarks, whose electric charges are either  $+\frac{2}{3}$  or  $-\frac{1}{3}$ , and/or antiquarks, with charges  $-\frac{2}{3}$  or  $+\frac{1}{3}$ . The quarks themselves have never been directly observed as single, free particles and this fact initially make it difficult for quarks to be accepted as anything other than convenient mathematical quantities for performing calculations. In order to study the quarks, we need to study the hadron first. Hadrons are important because free quarks are unobservable in nature and so to deduce their properties, we are forced to study hadrons [13].

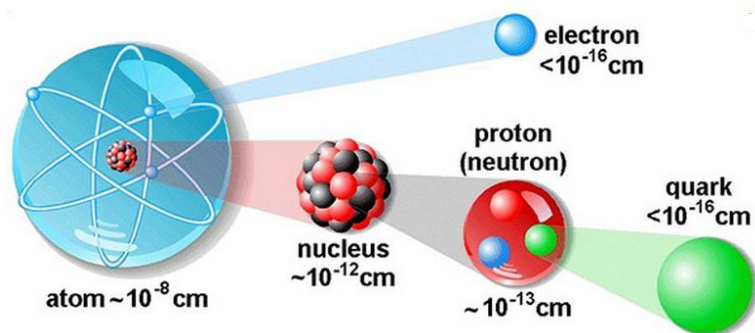


**Figure 2.2:** Hierarchy of the quarks

## 2.2 Quark Parton Model

Even though the quarks model was successful in describing the variety of baryons, there was a period of time when physicist debated whether these quarks were really physical entities and not just non-physical artifacts required by calculations. During this period, Feynman introduced the so-called Parton Model [35] which gave the best description of what the experiments really revealed. In this Parton Model, the scaling behavior of the structure functions were quickly understood as scattering on charged point-like particles in the proton. The essential idea is that the photon is interacting with free charged point-like particles inside the proton which is called partons.

In the Parton Model, we accept that the quarks are the building blocks of hadrons and play a direct role in the short distance dynamics. The knowledge about the structure of hadrons is described from the Parton Distributions Function (PDFs) and the parton fragmentation function. The basic idea of the Parton Model is that at high energy-momentum transfer  $Q^2$ , an electron scatters from an effectively free quark or antiquark and the scattering process is completed before the recoiling quark or antiquark has time to interact with its environment of quarks, antiquarks and gluons. Proton consists of 3 partons, identified with the QCD quarks. During the interactions, the proton is “frozen”. Electron proton scattering is the sum of incoherent electron quarks scattering.

The PDFs can explain the proton structure and is defined as the probability density for finding a particle with a certain longitudinal momentum fraction  $x$  at momentum transfer  $Q^2$ . This PDFs describe the distribution of short distance partons within hadrons, while the parton fragmentation function was describing the distribution of long distance hadrons within the fragmentation debris of an essentially isolated parton.

The experiments at Stanford confirmed the anticipated [19] phenomenon called scale invariance (Bjorken scaling) which proved that the scattering of high-energy electrons on the proton was independent of  $Q^2$ . The fact that the structure functions at very high energies become less dependent on  $Q^2$  and only dependent on the single variable  $\omega$  was predicted by Bjorken in the late 60's. Bjorken said that if large  $Q^2$  (high-energy) photons resolved point-like constituents in proton, the structure functions would become

$$MW_1(v, Q^2) \rightarrow F_1(\omega), \quad (2.1)$$

$$vW_2(v, Q^2) \rightarrow F_2(\omega), \quad (2.2)$$

where  $\omega = 2q \cdot p / Q^2 = 2Mv / Q^2$  is the dimensionless variable. The structure functions  $F_{1,2}$  are independent of  $Q^2$  for fixed value of  $\omega$ . This is the analogue to the  $\sin^{-4}(\theta/2)$  behavior of the momentum transfer in the famous Rutherford experiments, which led to the identification of the atomic nuclei and was the main argument that the photon is interacting with point-like particles, partons, since many physicists at that time did not believe that quarks were real physical objects.

The coming years after the Stanford experiments, many experimental results indicated that these partons had quantum numbers from the quarks model and as for today it has become clear that the partons in Feynman's parton model can be identified as quarks.

## 2.3 Quantum Chromodynamics (QCD)

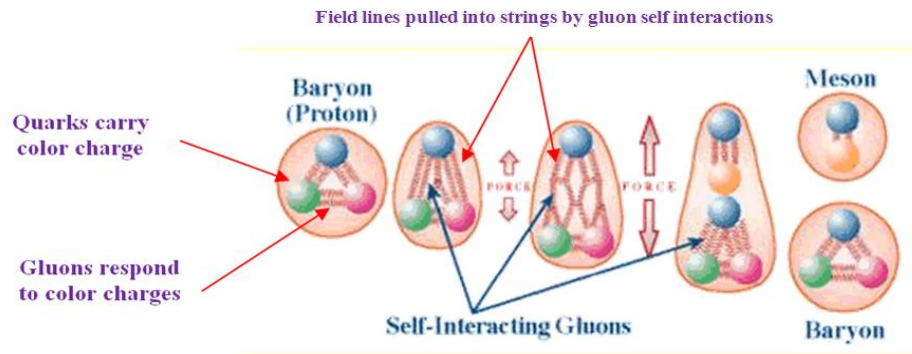


**Figure 2.3:** Quantum Chromodynamics process

Quantum chromodynamics, familiarly called QCD, is the modern theory of the strong interaction. Nowadays QCD is used to describe most of what goes on at high energy accelerators, trying to understanding what protons and neutrons are and how they interact. Quantum chromodynamics appears as an expanded version of Quantum electrodynamics (QED) whereas in QED there is just one kind of charge, while QCD has three kinds of charges, labeled by “color”. QED is the theory of light interacting with charged matter, where photon responds to the presence or motion of electric charge [18].

QCD states that quarks are confining, where gluons and quarks cannot exists as isolated particles. A baryon cannot be fragmented into its constituents, the quarks even if the strongest forces are applied. Instead of breaking into parts, the baryon creates one or several additional particles via the self-interacting and quantum-mechanical dynamics of the gluons field that connects the quarks within the baryon [47].

The color charges of QCD, red, green and blue have properties analogous to the electric charge. In particular, the color charges are conserved in all physical process and there are photon-like massless particles called gluons, which respond in appropriate

ways to the presence or motion of color charge, very similar to the way photons respond to an electric charge.

For all their similarities, there are several differences between QED and QCD. First of all, the response of gluons to color charge, as measured by the QCD coupling constant, is much more energetic than the response of photons to electric charge. The second one is that gluons can also change one color charge into another, in addition to just responding to the color charge and yet the color charge is conserved [18]. The third difference between QCD and QED is that gluons respond directly to one another, quite unlike photons. This is because gluons respond to the presence and motion of color charge and they carry unbalanced color charge while photons are electrically neutral.

Colored particles are always produced with their corresponding anti-colored particles, by symmetry. If these particles move away from each other it becomes energetically favorable to produce new quark-antiquark pairs which then combine to form the colorless observables known as hadrons.

## **2.4 Deep Inelastic Scattering (DIS)**

When a high-energy electron (or positron) collides with a proton, as in HERA collider, the simplest nuclear reaction that can occur is that a quark is ejected to give a high-energy jet of particles. This is Deep Inelastic Scattering (DIS) and is mediated by the exchange, between the electron and the quark, of a virtual photon;  $\gamma$ ,  $W$  or  $Z$  [53]. In this process, we call it deep because the photon penetrates the proton deeply and inelastic because the proton breaks up.

The scattering process not only involves valence quarks, but can also occur by means of virtual quark-antiquark pairs that appear temporarily within the proton.

Indeed, the proton may be considered as consisting of a continuum of different combinations of partons, that is to say (anti)quarks and gluons, and depending on how violently it is struck by the exchanged boson [18]. Thus the PDFs of the proton are functions both of the fraction  $x$  of the protons taken by a given parton and of the virtuality  $Q^2$  of the exchanged boson [53]. The DIS experiments paved the way for understanding the structure of the proton and neutron which was interpreted in the parton model.

### 2.4.1 Electron-Proton Scattering

In electron proton collision, electron was used as a probe of the proton structure. At HERA collider, the physics was preliminary focused on testing our comprehension of the strong force, providing us information of the multihadrons production; help us to identify separate hadrons and resonance. The electron-proton interaction continues via the exchange of a virtual vector boson, either a  $\gamma$  or a  $Z^0$  or a  $W^\pm$  as shown in Figure 2.4. During this process, when the energy transfer  $Q^2$  becomes larger, the proton breaks up, first into resonant baryon states and later (higher  $Q^2$ ) to complicated multi-particles states as is illustrated in Figure 2.4.

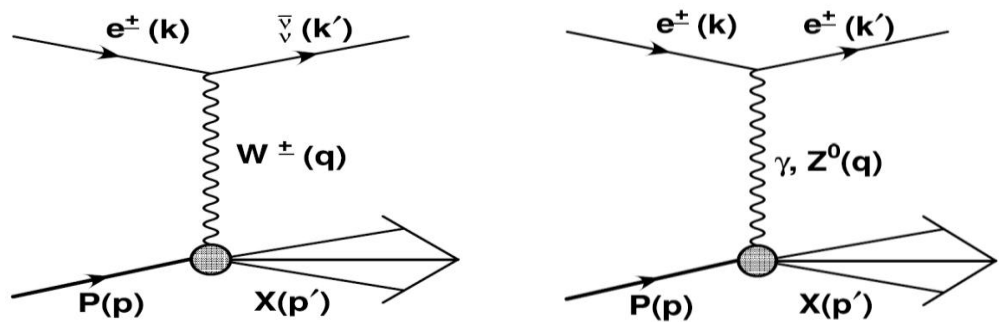


**Figure 2.4:** Lowest order Feynman diagrams for Charged Current and Neutral Current Deep Inelastic Scattering (DIS)



There are two types of interaction during the Deep Inelastic Scattering (DIS) process. The first one is the Charged Current (CC) process. This process occurs when the exchanged boson emitted from the electron is a charged  $W^\pm$  particle, which collides with the proton, consequently leaving a neutrino in the final states. The second interaction is the Neutral Current (NC) process. During this process, the electron will emit an electrically neutral exchange-boson, such as  $\gamma$  or  $Z^0$  particle, to collide with a quark (or gluon) within the protons.

The interactions are generally of the form shown in Eqn. 2.3. Here,  $X$  is generally a high multiplicity hadronic system.

$$e + P \rightarrow e' X \quad (\text{NC}); \quad e^+(e^-) + P \rightarrow \bar{\nu}(\nu) X \quad (\text{CC}) \quad (2.3)$$

## 2.5 HERA Kinematics

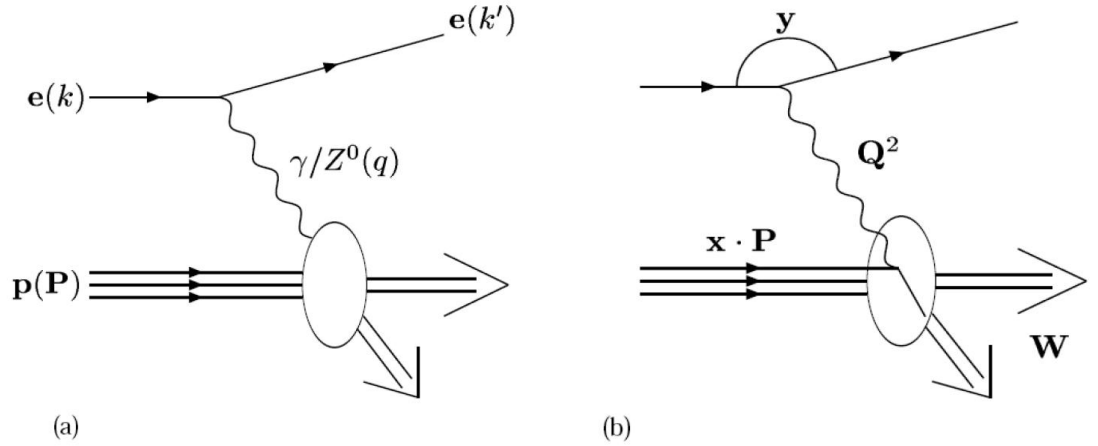


**Figure 2.5:** Feynman diagrams for a Neutral Current DIS collisions. a) The 4-vectors of incoming and outgoing particles. b) The Lorentz invariant scalar defining the events.

Figure 2.5 shows an electron proton scattering interaction schematically in HERA. During the head-on electron and proton collisions at high energy, the electron will emit a gauge boson (neutral boson, photon or  $Z^0$  for the Neutral Current DIS interaction, and charge boson,  $W^\pm$  for the Charge Current interaction). This gauge boson will interact with the partons inside the proton structure, and then produce new hadrons. This process is called Deep Inelastic Scattering process.

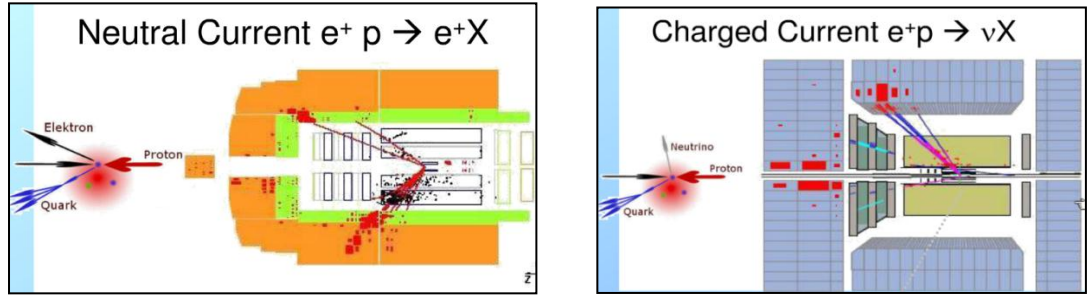


**Figure 2.6:** The simulated picture of Neutral Current and Charge Current process in Deep Inelastic electron-proton scattering in HERA.

From the Figure 2.6 above, we can see that the Neutral Current interaction will produce electron and hadrons in the final state, while the Charge Current interaction will produce neutrino and hadrons in the end of the process. For this thesis, we will study the NC DIS interaction.

In the Figure 2.5(a), the 4-vectors  $k$  and  $k'$  describe the incoming and outgoing electrons,  $P$  describe the proton and  $q$  is for the exchange bosons. The NC DIS interaction can be written as:

$$e(k) + p(P) \rightarrow e'(k') + X(P') \quad (2.4)$$

Assuming that  $k$ ,  $k'$ ,  $P$  and  $P'$  are the four vectors of the initial and final electron of the incoming proton and of the outgoing hadronic system, the usual variables describing the properties of electron-proton scattering [16] are

$$Q^2 = -q^2 = -(k - k')^2, \quad (2.5)$$

$$s = (k + P)^2, \quad (2.6)$$

$$W^2 = (q + P)^2 = p^2, \quad (2.7)$$

$$x = \frac{Q^2}{2P \cdot q}, \quad (2.8)$$

$$y = \frac{q \cdot P}{k \cdot P}, \quad (2.9)$$

$$v = \frac{q \cdot P}{m_N}, \quad (2.10)$$

where  $q = k - k'$  defines the 4-momentum transfer from the lepton to the proton from which follows that  $P' = P + q$ ,  $P$  describe the proton and  $q$  is for the exchanged photon.  $Q^2$  is the square of the four-momentum transfer  $q$  between the incoming electron and the scattered electron.  $x$  is the fraction of the longitudinal momentum of the struck quark in the proton, if it is assumed that the parton transverse momenta inside the proton and the parton masses can be neglected compared to  $Q^2$ .  $y$  is the relative energy transfer of the electron to the proton, with respect to the proton rest frame. The dimensionless variables  $x$  and  $y$  will be useful in characterizing the high energy limit and correspond to the fractions of the incident energies carried by the interacting particles.

The centre-of-mass energy squared of the proton system is:

$$s = (k + P)^2 \cong 2k \cdot P = \frac{Q^2}{xy} \quad (2.11)$$

where the approximation is that the particle masses are small compared to the centre-of-mass energy and this approximation is very good for the HERA machine. Hence, for a given centre-of-mass energy, any two of  $x$ ,  $y$  and  $Q^2$  fully defined the  $eP$  scattering kinematics.

The centre-of-mass energy,  $W$ , of the hadronic system is:

$$W^2 = (q + P)^2 \cong 2P \cdot q + q^2 \quad (2.12)$$

The inclusive differential cross section, integrated over all possible hadronic final state, is a function of two variables which uniquely determine the kinematics of the events. These variables are most easily recognizable as the energy and the production angle of the scattered lepton. However, the differential cross section is usually expressed in terms of two variables,  $x$  and  $Q^2$ , defined in Eq. (2.6) and Eq. (2.9) [16],

$$\frac{d^2\sigma}{dx dQ^2} = A \left\{ \frac{y^2}{2} 2xF_1(x, Q^2) + (1-y)F_2(x, Q^2) \pm (y - \frac{y^2}{2})xF_3(x, Q^2) \right\} \quad (2.13)$$

where, for  $Q^2 < M_{W,Z}^2$  (the mass squared of the intermediate vector bosons),  $A = G_F^2 / 2\pi x$  for neutrinos and anti-neutrinos with  $G_F$  the Fermi constant, and  $A = 4\pi\alpha^2 / xQ^4$  for charged leptons with  $\alpha$  the electromagnetic coupling constant. The structure functions,  $F_i$ , may depend on the kinematics of the scattering and the chosen variables are  $x$  and  $Q^2$  [16].

## 2.6 Baryon Production

The string fragmentation model [6] is able to give generally very good description of the distribution of hadrons in quark and gluon jets [1]. In the Lund String Hadronization model, the confining field is expected to behave as a relativistic string, i.e. like a vortex line in a superconductor. The model contains first a description of the decay of a straight string, and secondly the assumption that gluons behave as transverse excitations or kinks on the string. The gluon kinks have no inherent influence on particle compositions.

The string can break by the production of  $q\bar{q}$  pairs, which are pulled apart by the string tension. As the  $q$  and  $\bar{q}$  move apart, the potential energy stored in the string increases, and the string may break by the production of new  $q'\bar{q}'$  pair, so that the system splits into two color-singlet systems  $q\bar{q}'$  and  $q'\bar{q}$ . If the invariant mass of either of these string pieces is large enough, further breaks may occur. In the Lund string model, the string break-up process is assumed to proceed until only on-mass-shell hadrons remain, each hadrons corresponding to a small piece of string with a quark in one end and an antiquark in the other [52]. When a quark meets an antiquark from a neighboring pair, they can form a final state meson, as shown in Figure 2.7 [31].

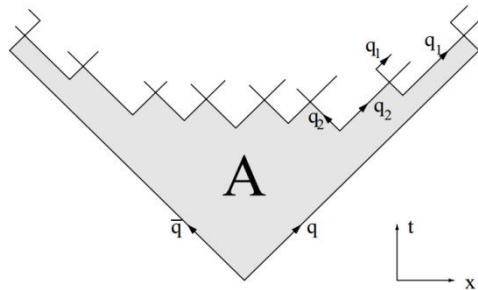


**Figure 2.7:** String fragmentation in  $x-t$  space.

Baryon production is a more complex process than the production of mesons.  $B\bar{B}$  correlations in rapidity are in agreement with the assumption that the  $B$  and the  $\bar{B}$  are produced as neighbours or next to neighbours in a string break-up. The distribution in the angle between the baryon and the thrust axis (i.e. the general string direction) in the  $B\bar{B}$  is not spherically symmetric [40, 2].

Recent data from polarized  $e^+e^-$  annihilations show that baryons are more frequent in quark jets than in antiquark jets [37]. Thus baryon-antibaryon pairs do not originate from isotropically decaying clusters. Instead the distribution can be understood if the  $B$  and  $\bar{B}$  are pulled in opposite directions at the string break-up. The string breaks by the production of a diquark-antidiquark pair in a  $\bar{3}-3$  color state, which becomes constituents in the baryon and the antibaryon [7].

To improve agreement with experiments, a more general framework for baryon production was presented in the “popcorn” model [8], in which diquarks as such are never produced, but rather baryons appear from the successive production of several  $q\bar{q}$  pairs [52]. Assume that a color field is stretched between e.g. a red quark,  $r$  and an antired antiquark,  $\bar{r}$ . The string can break if a  $r\bar{r} q\bar{q}$  pair is produced and pulled apart by the string tension. We can also imagine that a  $b\bar{b}$  pair is produced as a virtual fluctuation. If the  $rb(\bar{r}\bar{b})$  is in a color antitriplet  $\bar{g}$  (triplet  $g$ ) state, the color field between the produced quark and antiquark will correspond to a triplet color field with the same strength as the original field. Thus equal forces in opposite directions act on the new quark and the new antiquark.

In accordance with the uncertainty principle, they can move around freely for a time inversely proportional to their energy. These quarks are called “curtain quarks”, from the picture of rings on a curtain-rod, sliding back and forth with no frictional

losses and without changing the properties of the rod. In distinction to curtain quarks, the quarks that cause the string to break are called “vertex quarks”. If the string breaks within the color fluctuation region, an effective diquark-antidiquark pair is produced, see Figure 2.8 and Figure 2.9 [31].

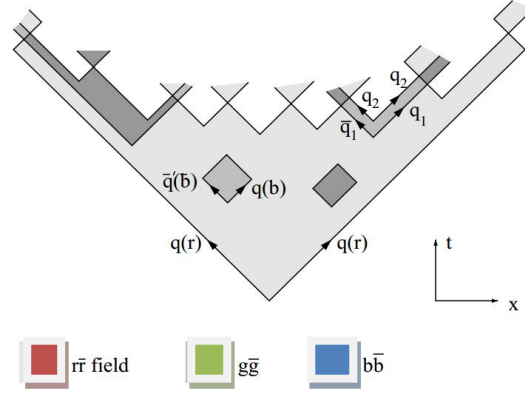


**Figure 2.8:** If a vertex pair  $q_2 \bar{q}_2$  is produced inside a color fluctuation region spanned by  $q_1 \bar{q}_1$ , an effective diquark-antidiquark pair has “popped out” in a stepwise manner. The model allows for several breakups in the color fluctuation region, creating one or some mesons among the antibaryon and baryon, as shown to the left.

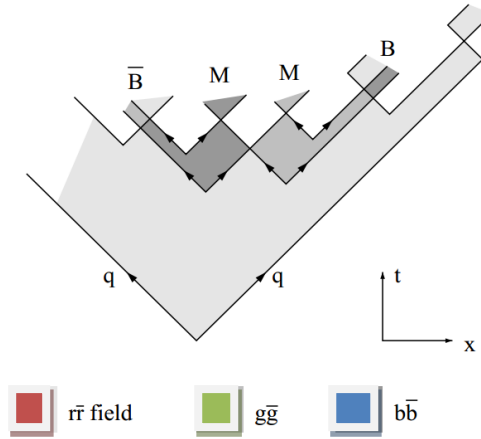


**Figure 2.9:** A popcorn example with two curtain quark pairs.

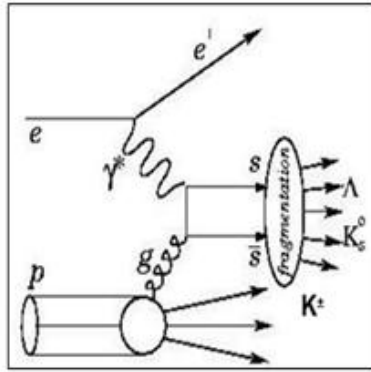
### 2.6.1 Strange Quark Production

The production of the strange quarks can be either from the hard interactions or from pure fragmentation process. The fragmentation process becomes important for strangeness production at HERA. Production of the strange quarks during the electron proton collisions at HERA can be explained by various mechanisms.

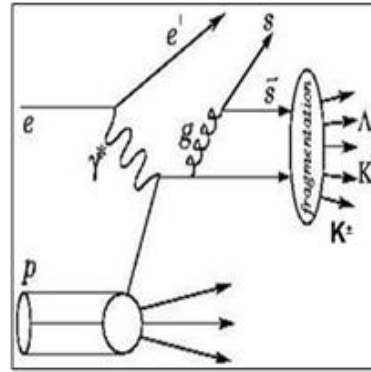
The first mechanism is Boson-Gluon fusion process, as shown in Figure 2.10(i). During this process, the  $s(\bar{s})$  quarks are produced when the exchange boson couples with a gluon from the proton. This is the major channel to produce strange quarks. The second strange quarks production mechanism is given in Figure 2.10(ii), describing the gluon-splitting process. In this process, photon interacts with parton from proton, produced gluon, and gluon split into  $s(\bar{s})$  quarks.

The third mechanism is hard scattering of  $s$  sea quark, as shown in Figure 2.10(iii). In this process, there is no  $s$  valence quark among proton constituents. But as the  $Q^2$  increase, the  $s(\bar{s})$  quarks can be resolved by the virtual photon and can be knocked out to form a final strange hadron. The fourth strangeness production channel is the heavy flavor decay. In this process, strange quarks were produced from the decay of heavy quarks such as charm or beauty quarks. However, the strange production from this mechanism is constrained by the low rates of the heavy flavor production. Strange quarks could also originate from fragmentation process, where the strange quarks emerge from gluon fluctuations in the parton shower instead of being directly involved in the hard scattering process.

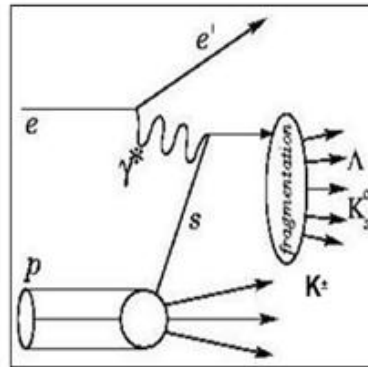




i) Boson-gluon fusion



ii) Gluon-splitting



iii) Flavor excitation-hard  
scattering of  $S$  sea quark

**Figure 2.10:** Possible mechanism of the strange quark production

## 2.7 Physics Motivations of the Thesis

Particle physics is the study of the basic elements of matter and the force acting among them. It aims to determine the fundamental laws that control the character of matter and the physical universe.

Strange hadron productions in particularly baryons are not well understood but these strange particles are interesting because of their behaviour such as low mass, high statistics and clean signal. Due to the conservation of strangeness, lightweight particles do not decay as quickly if they exhibit strangeness. The particles lifetime will be longer when the number of strangeness is high.

The measurements of the strange hadron can answer several physics problems and can show that strange quarks are like other quarks, behave as point-like particles. The obvious way to determine if the proton is built up out of point-like particles is to compare the way the cross-section behaves, since it depends heavily on the proton structure functions. By measuring the total cross-sections, we can know the probability of interaction between small particles. The baryon-antibaryon production asymmetry could give a hint on how the presence of the initial proton affects the  $\Lambda$  production in the final state. While study on baryon to meson ratio can answer the question on how do baryons and mesons formed and the question on how does quarks become hadrons can be answered by studying the rapidity particle correlation between baryon and antibaryon.

## CHAPTER 3

### Experimental Set-up

In order to explore the structure of hadrons in particle physics, it requires projectiles whose wavelengths are at least as small as the effective radii of the nuclei or hadrons. This determines the minimum value of the momentum  $p = h/\lambda$  and hence the energy required. In particle physics experiments, particle accelerators were used to collide two particles at high energy and at speed near to the speed of light. High energy was required in order to produce new and unstable particles.

This reveals a disadvantage of fixed-target experiments when large centre-of-mass energies are required. The centre-of-mass energy is important because it is a measure of the energy available to create new particles. In the laboratory frame, at least some of the final state particle must be in motion to conserve momentum. Particle physics experiments are a modern version of Rutherford's table-top experiments, on scattering of alpha particles with thin metal foils.

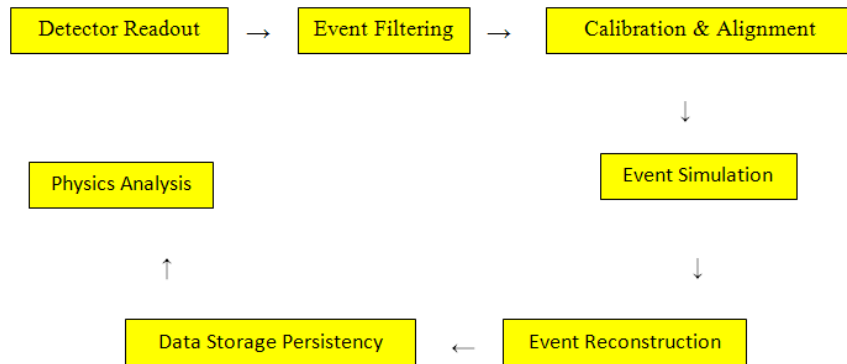


**Figure 3.1:** Flow in the data processing process in High Energy Physics Experiments.



**Figure 3.2:** The data from HERA was stored here.

### 3.1 The HERA *ep* Collider

The Hadron Electron Ring Accelerator, HERA was the first and so far the only electron-proton collider in the world situated at DESY in Hamburg, Germany. The DESY (Deutsches Elektronen Synchrotron, “German Electron Synchrotron”) is the biggest research center for particle physics, with sites in Hamburg and Zeuthen [16]. The main purposes of DESY are fundamental research in particle physics and research with synchrotron radiation.

HERA is located under the DESY site nearby Volkspark around 15 to 30 m underground and has a circumference of 6.3 km and consists of two separate accelerators, HERA and PETRA. The construction of these two-ring accelerators took from May 1984 until November 1990. The beams were segmented into 180 colliding bunches each, providing a bunch crossing rate of 10 MHz. There are four experiments situated at HERA. The two collider experiments H1 and ZEUS were the main general multi-purpose detectors in HERA and have been in operation since 1992. In 1995 the HERMES experiment started the data taking using the polarized electron beam on a

fixed polarized gas target. This detector was designed for investigating the spin distribution of the quarks in protons and neutrons. The HERA-B is a proton-proton fixed target experiment, operated between 1998- 2003 and was constructed in order to measure the Charge Parity violation in B-meson system.

HERA consists of two storage rings mounted on top of one another, except at the interaction points inside the detectors ZEUS and H1. One ring is for electron/positron, operates at room temperature with normal conductors, while the other one is proton storage rings, and required superconducting magnets operating at a temperature of 4.4 K. Those temperatures were required to produce magnetic field of 4.65 T which was necessary to bend the high momentum protons in the arcs of the ring. This magnetic field limited the proton energy to 920 GeV. The proton and electron/positron beams in the storage rings were not continuous, but rather grouped into bunches which collide every 96 ns, thereby setting the maximum rate of collisions.

At very high energies with collisions of electrons/positrons at energy of 27.5 GeV with protons at 920 GeV, HERA offered physicist to study the unique possibility of physics topics. The structure of the proton constituents (quarks and gluon), as well as other interesting physics topics such as photon structure, perturbative Quantum Chromodynamics (jets and heavy quarks), neutral, charged current and electroweak process was studied in HERA.

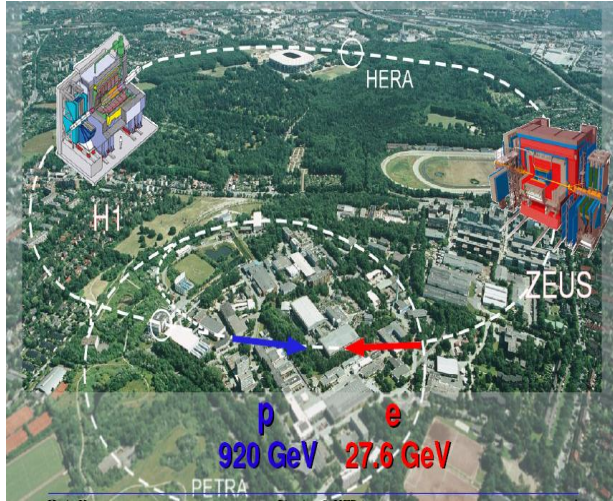


**Figure 3.3:** The HERA and PETRA accelerator aerial view at the DESY campus in Hamburg, Germany. HERA was at 15-30 m underground with circumference 6.3 km.

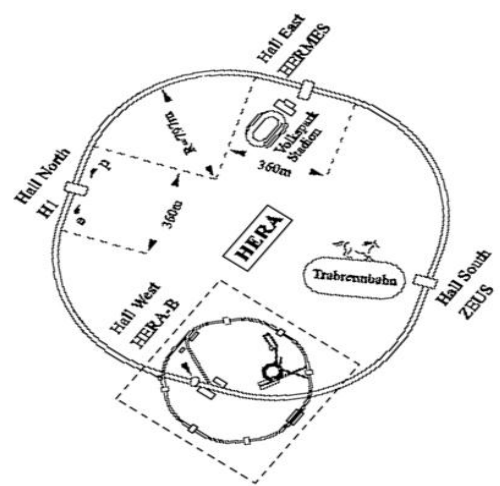


**Figure 3.4:** The HERA collider with the four experiments H1, ZEUS, HERMES and HERA-B.



**Figure 3.5:** A small segment of the HERA tunnel. The proton beam is travelling in the large vacuum tube in the middle to the right while the electron beam tube is below that.

### 3.2 The ZEUS Detector

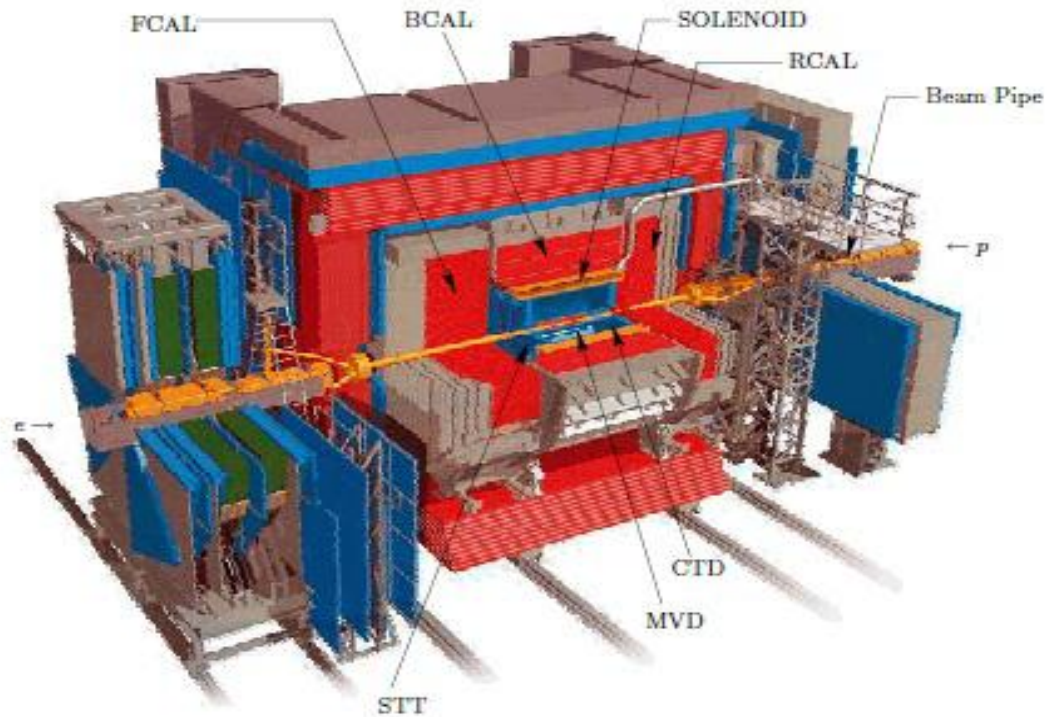


**Figure 3.6:** Cutaway of the ZEUS detector

The ZEUS experiment was one of two general purpose  $e^-p$  colliding beam experiments at the Hadron Electron Ring Accelerator (HERA) at Deutsches Elektronen Synchrotron (DESY) in Hamburg, Germany. The goal of the ZEUS detector was to determine with high precision the energies, directions and nature of single particles and particle jets created in the interactions. The ZEUS detector was located in the South Hall of HERA with dimensions  $12\text{ m} \times 10\text{ m} \times 19\text{ m}$  and its total weight was 3600 tons.

The overview of the ZEUS detector in various cross section cuts can be found below.



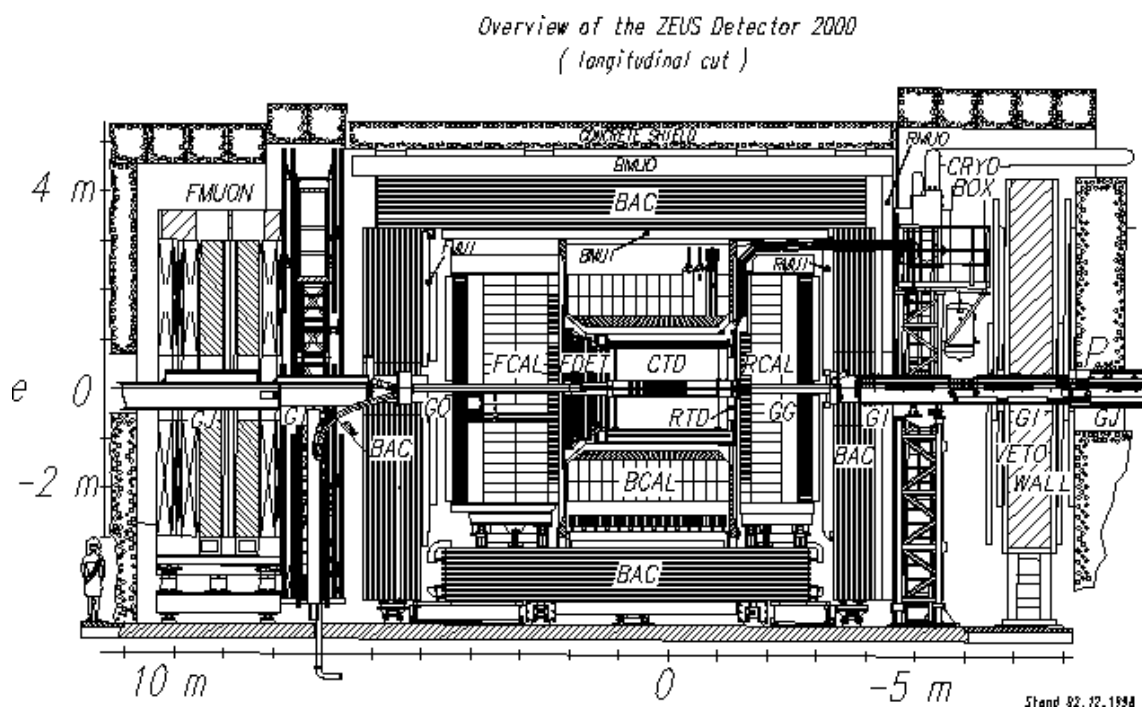


**Figure 3.7:** Cross section of the ZEUS detector in the vertical plane, side view.

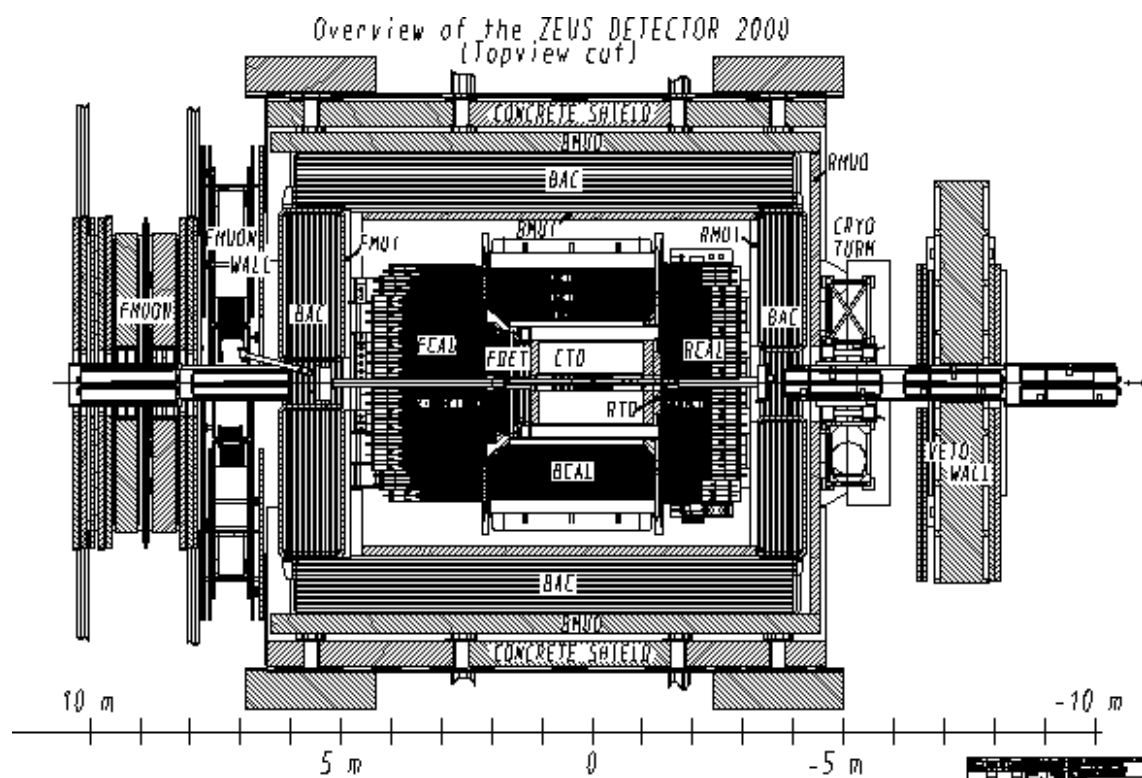


**Figure 3.8:** Cross section of the ZEUS detector in the vertical plane, top view.



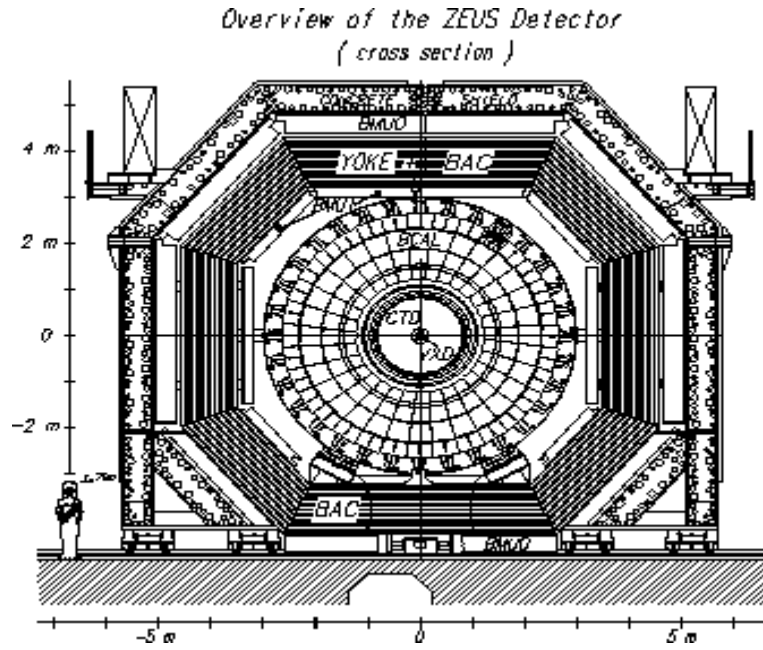


**Figure 3.9:** Cross section in transverse plane containing the nominal interaction point.

The heart of the ZEUS detector was the uranium scintillator calorimeter (CAL) which measured energies and directions of particles and particle jets with high precision. This hermetically enclosed the tracking detector which measured the tracks of charged particles using wire chambers and which consisted of: a vertex detector (VXD), the central tracking detector (CTD), forward (FTD) and backward (RTD) drift chambers and in the forward direction a transition radiation detector (TRD) to identify high energy electrons/positrons. These chambers were surrounded by a thin superconducting solenoid coil producing an axial magnetic field of 1.43 Tesla for determining the momentum of charged particles from back curvature [16].

The ZEUS detector main parts as shown in Figure 3.6, Figure 3.7 and Figure 3.8 are as follows;

- The high-resolution Uranium-Scintillator Calorimeter (UCAL) [34]: was used to measure energies and directions of particles and jets with high precision. CAL consisted of three parts: the forward (FCAL), the barrel (BCAL) and the rear

(RCAL) calorimeters. Each part is subdivided into towers and each tower is longitudinally segmented into one electromagnetic section and either one (in RCAL) or two (in BCAL and FCAL) hadronic sections. The smallest subdivision of the calorimeter is called a cell. The CAL energy resolutions, measured under test-beam conditions, are  $\sigma(E)/E = 0.18/\sqrt{E}$  for positron and  $\sigma(E)/E = 0.35/\sqrt{E}$  for hadrons, with  $E$  in GeV. The timing resolution of the CAL is  $\sim 1$  ns for energy deposits greater than 45 GeV;

- Central Tracking Detector (CTD) [26], aided by an axial magnetic field of 1.43 T;
- Micro Vertex Detector (MVD) [4], installed in 2000 after the reconstruction. MVD is designed for more precise measurements of the track reconstruction and track momentum values;
- 3-component (forward, barrel and rear) system of muon chambers; 3 inner chambers (FMUI, BMUI, RMUI) and 3 outer (FMUO, BMUO, RMUO);
- Small-angle Rear Tracking Detector (SRTD) which improves the angular resolution on the scattered electron in the rear direction.

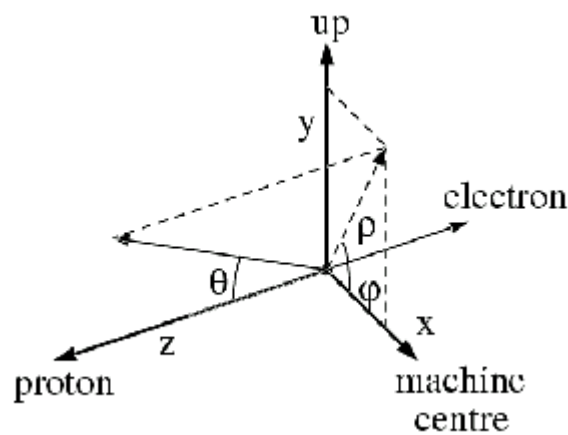


**Figure 3.10:** The ZEUS coordinate system.

The ZEUS coordinate system is a right-handed Cartesian system, with the  $z$  axis pointing in the proton beam direction, referred to as the “forward direction”, and the  $x$

axis pointing towards the center of HERA. The coordinate origin is at the nominal interaction point. The polar angle,  $\theta$ , is measured with respect to the proton beam direction. The azimuthal angle in the  $x$ - $y$  plane is called  $\phi$ . A full description of the ZEUS detector is given in [45].

A brief description of the components that are most relevant for this analysis is given below. The main components of the ZEUS detector that are used in this analysis are the tracking detectors, especially the central tracking detector (CTD) [26] and the microvertex detector (MVD) [4].

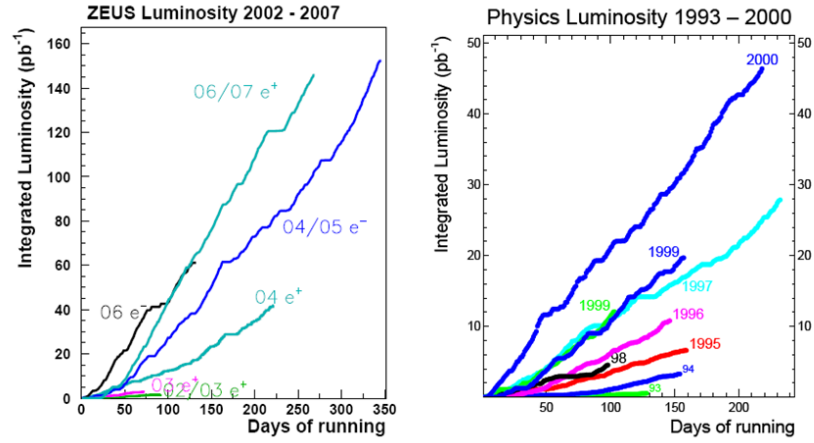


**Figure 3.11:** Integrated luminosity collected by ZEUS for the 1993-2000 and 2002-2007 periods, shown separately for each year.

### 3.2.1 The Central Tracking Detector (CTD)

The Central Tracking Detector provides the measurements of particles momentum, vertexing, particle id via energy loss and also participates in the trigger at all levels. Energy loss happened when charge tracks were crossing some materials, it will lose some energy per unit length. The ZEUS CTD was conceived to detect and identify the charged particles with high precision over a wide range of  $Q^2$ .

The CTD operated in a magnetic field of 1.43 T provided by a thin superconducting solenoid and CTD consisted of 72 cylindrical drift-chamber layers, organized in nine superlayers covering the polar angle region  $15^\circ < \theta < 164^\circ$ .

The CTD was filled with a gas mixture of 82% Argon (Ar), 13% Carbon-dioxide (CO<sub>2</sub>) and 5% Ethane (C<sub>2</sub>H<sub>6</sub>). When charged particles pass through the gas, the gas will ionized into negatively charged electrons and positively charged ions. The electrons moved to the positively charged sense wires and the ions drift towards the negatively charged sense wire because of the presence of electromagnetic fields in the detector. The subsequent collection and amplification of the signal pulse creates a detectable signal (indicating the passing of the charged particles). The electronic read out collected these signals.

The pulse measured with the sense wires was proportional to the energy loss of particles passing through the CTD. Particle identification was possible using measurements of the mean energy loss,  $dE/dx$ , of charged particles in the gas of the active volume. The odd numbered (axial) superlayers contain drift wires that run parallel to the z-axis. The even numbered (stereo) superlayers are oriented at a small angle with respect to the z-axis (please refer Figure 3.9). This allows both  $r\phi$  and  $z$  coordinates to be measured.

The hits in CTD were combined to reconstruct particle trajectories. The transverse momentum resolution for full-length CTD tracks was  $\sigma(p_T)/p_T \approx 0.0058p_T \oplus 0.0065 \oplus 0.0014/p_T$ , with  $p_T$  in GeV. The average resolution that has passed through all super layers in  $r\phi$  plane in CTD was  $\sigma(\phi) \approx (2 \times 180 \mu m) / 63.2 cm$ . While the average resolution that had passed through all superlayers in z-direction in CTD is  $\sigma(\theta) \approx (2 \times 2 mm) / 63.2 cm$  [26].

### 3.3 HERA-II

The ZEUS detector was upgraded at that time in a number of areas to prepare for the physics opportunities of HERA-II. The HERA upgrade produced about a factor of five in improvements in luminosity delivered to the experiments and aimed to accumulate  $1 \text{ fb}^{-1}$  of data in the HERA-II program. In order to take advantage of this, the ZEUS detector was upgraded in several areas: the silicon microvertex detector (MVD); the straw-tube tracker (STT); and the luminosity monitor [10].

HERA-I produced deep insights into QCD and laid the foundations for the study of the space-like electroweak interaction at high  $Q^2$ . HERA-II promised to build on those foundations to open new fields of precision electroweak study and searches for the physics beyond the Standard Model [10].

#### 3.3.1 The Micro Vertex Detector (MVD)

The Micro Vertex Detector was installed in 2000/2001 for HERA-II data in order to be useful for tagging heavy flavor mesons. This detector provided the capability to reconstruct secondary vertices displaced from the primary by distance of the order  $100 \text{ }\mu\text{m}$ . Its central barrel consisted of 30 “ladders”, each of which contain five modules of four single-sided silicon microstrip detectors arranged in pairs with orthogonal strip directions. The elliptical shape of the beam pipe is necessary to avoid the intense synchrotron radiation generated by the new superconducting quadrupoles. This shape implied a complex geometry in which ladders were placed such that most emerging charged particles intersected the three detector layers.

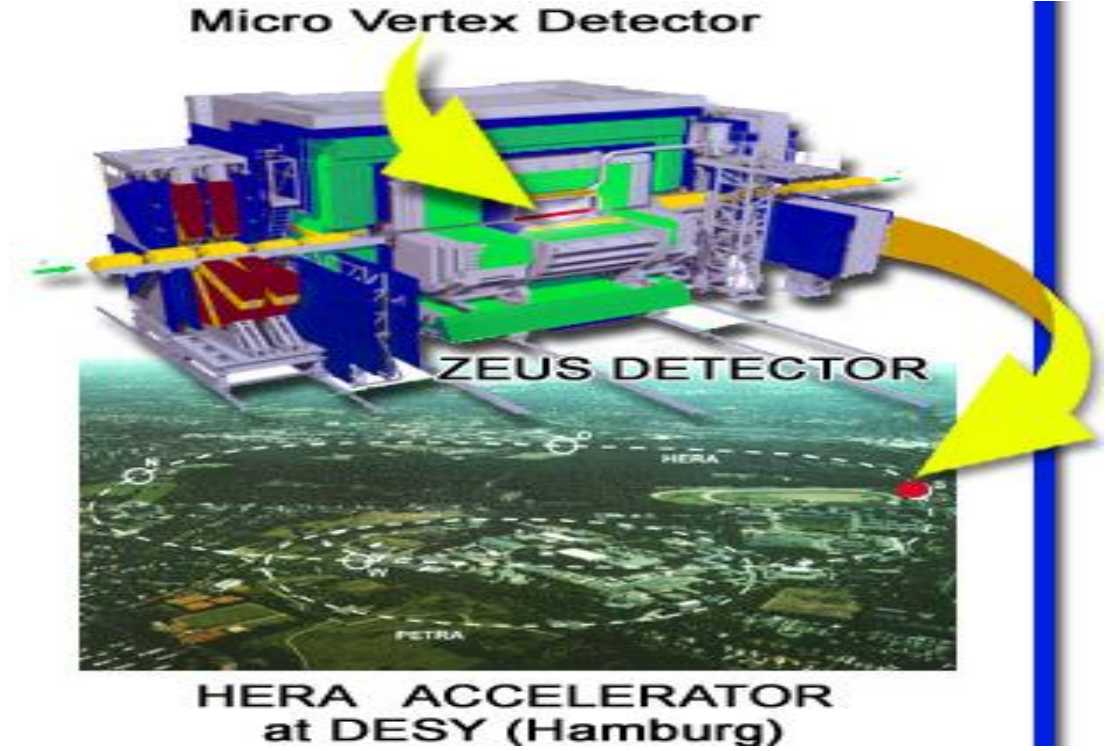


**Figure 3.12:** The ZEUS Micro Vertex Detector (MVD)

The MVD silicon tracker consisted of a barrel (BMVD) and a forward (FMVD) section [4]. The BMVD contained three layers and provided polar-angle coverage tracks from  $30^\circ$  to  $150^\circ$ . The four-layer FMVD extended the polar-angle coverage in the forward region to  $7^\circ$ . After alignment, the single-hit resolution of the MVD was  $24 \mu\text{m}$ . The transverse distance of closest approach (DCA) to the nominal vertex in  $XY$  was measured to have a resolution, averaged over the azimuthal angle of  $(46 \oplus 122/p_T) \mu\text{m}$ , with  $p_T$  in GeV.

The Micro Vertex Detector was aligned with a combination of tracks from cosmic events and  $ep$  events in the HERA collider. MVD could only detect the charge particles. As charged particles passing through the silicon strips, they cause small ionization currents which can be detected and measured. In this analysis  $\Lambda$ ,  $\bar{\Lambda}$  and  $K_0^s$

are neutral, so we cannot observe them directly by the CTD and the MVD. However we can observe them through their decay products.

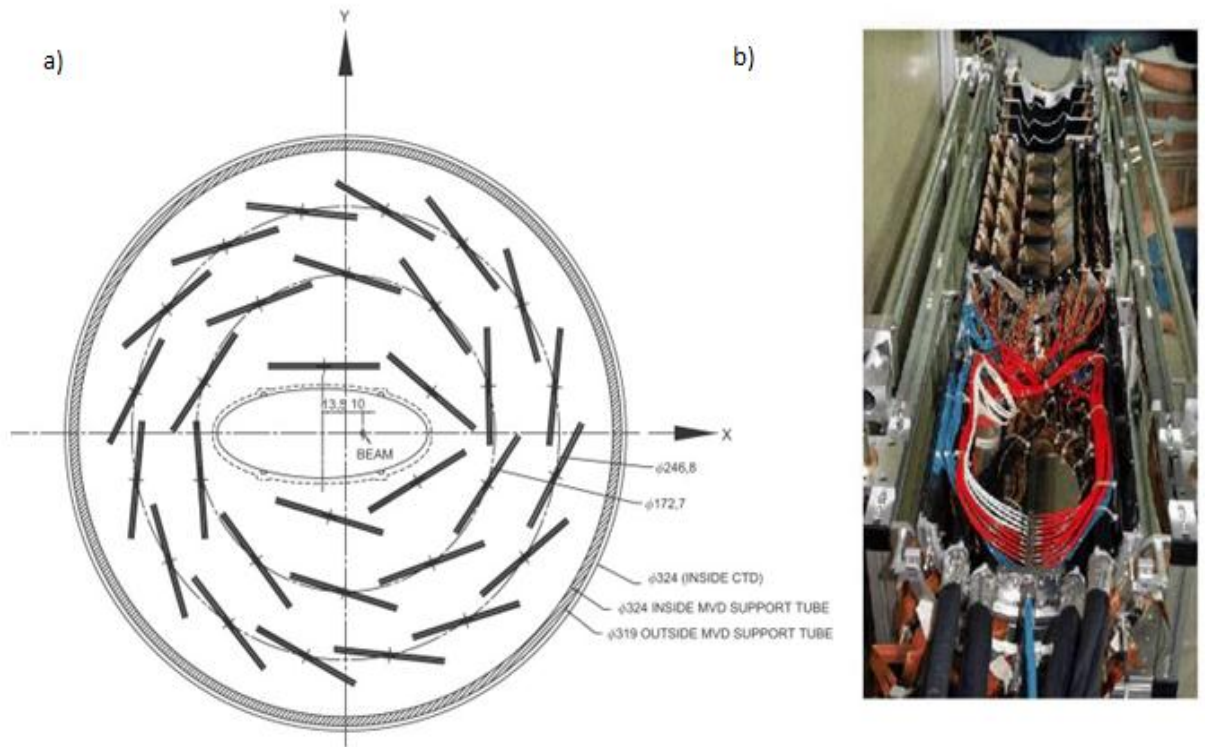


**Figure 3.13:** a) A section through the barrel MVD, showing the arrangement around the beam-pipe of each the MVD ladders. b) A photograph of one half of the MVD, showing the barrel ladders, one half of each of the forward “wheels” and the cables and services [10].

### 3.4 ZEUS Analysis and Computing Model

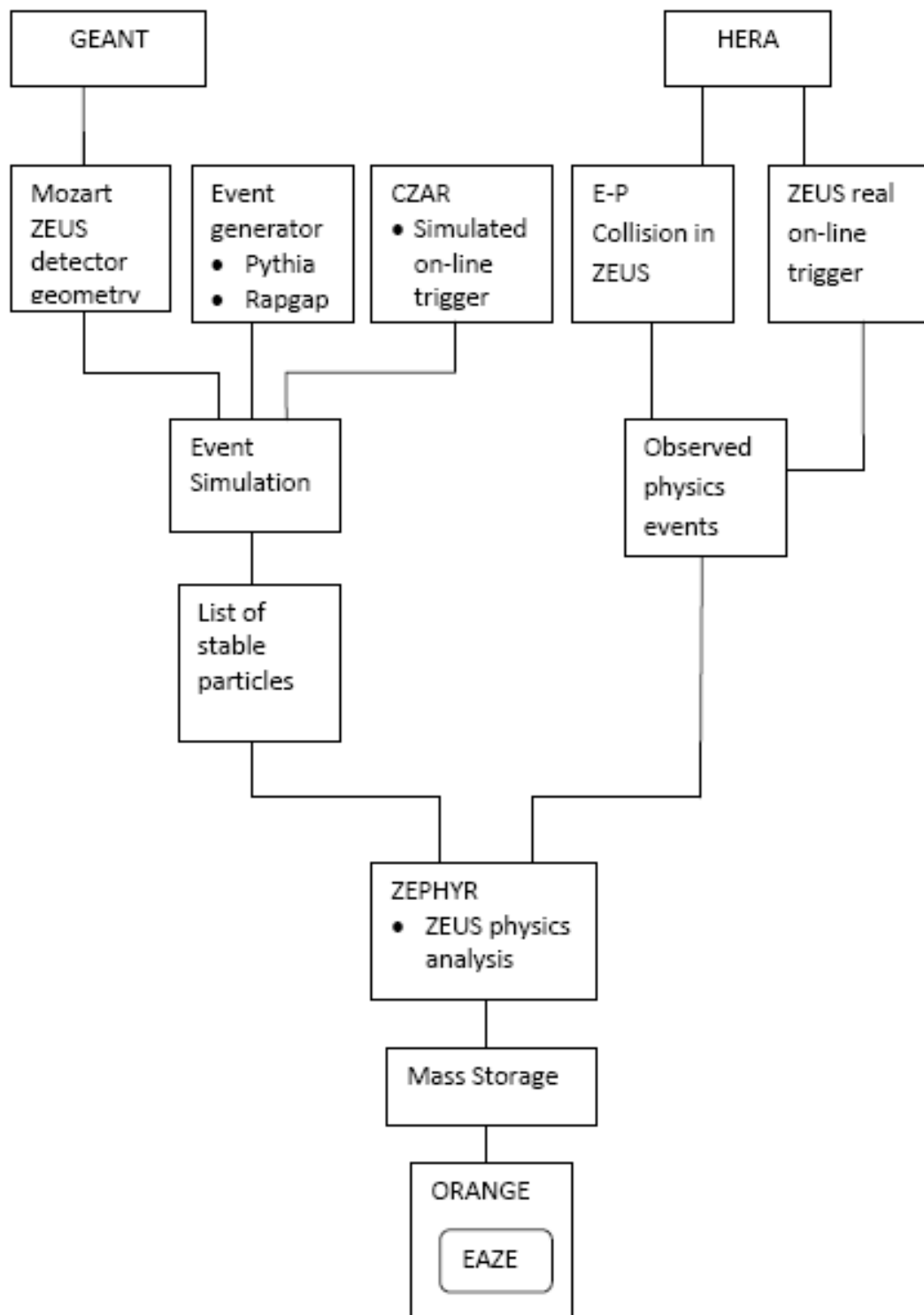


**Figure 3.14:** Flow diagram of event analysis in the ZEUS detector. Simulated and actual events were run concurrent and compared to extract correction factor from pQCD calculation.



### **3.4.1 Data processing: the ZEUS Reconstruction Factory**

The data taken by the ZEUS experiment are processed on a PC farm running Linux as operating system. Reconstruction is performed in a semi-automated way under the ZEUS Reconstruction Factory (ZRF), a framework based on MySQL, PHP4 and Apache with LSF as the underlying batch system.

The production system has the flexibility to use also resources of the ZEUS analysis facility (ZARAH) when they are free. After the end of ZEUS data taking period all datasets have been reconstructed and then re-processed with improved calibration constants and reconstruction software [57].

### **3.4.2 ZEUS Analysis Facility (ZARAH)**

ZARAH is the central ZEUS data analysis facility. It provides the computing infrastructure & support for batch data analysis ("data mining") and the event data storage facilities of the experiment.

The core of the ZARAH facility is a computation cluster which consists of the PC based batch farm and the storage facilities of the experiment. The access to the ZEUS event repository is highly optimized through the implementation and usage of the special services like zesLite tag database for an efficient event selection and a disk cache system for the data storage and transfer between the tape repository and the farm nodes.

The present ZARAH PC farm consists of 60 dual-processor nodes, where 20 nodes have 2.6 GHz Opteron CPU on a Tyan motherboard, 20 are based on Intel Xeon 3.06 GHz and 20 nodes have Xeon 2.2 GHz, . The LSF batch system integrates this

facility with the reconstruction farm. I/O from & to mass storage relies heavily on the dCache system [57].

### 3.4.3 ZEUS Analysis

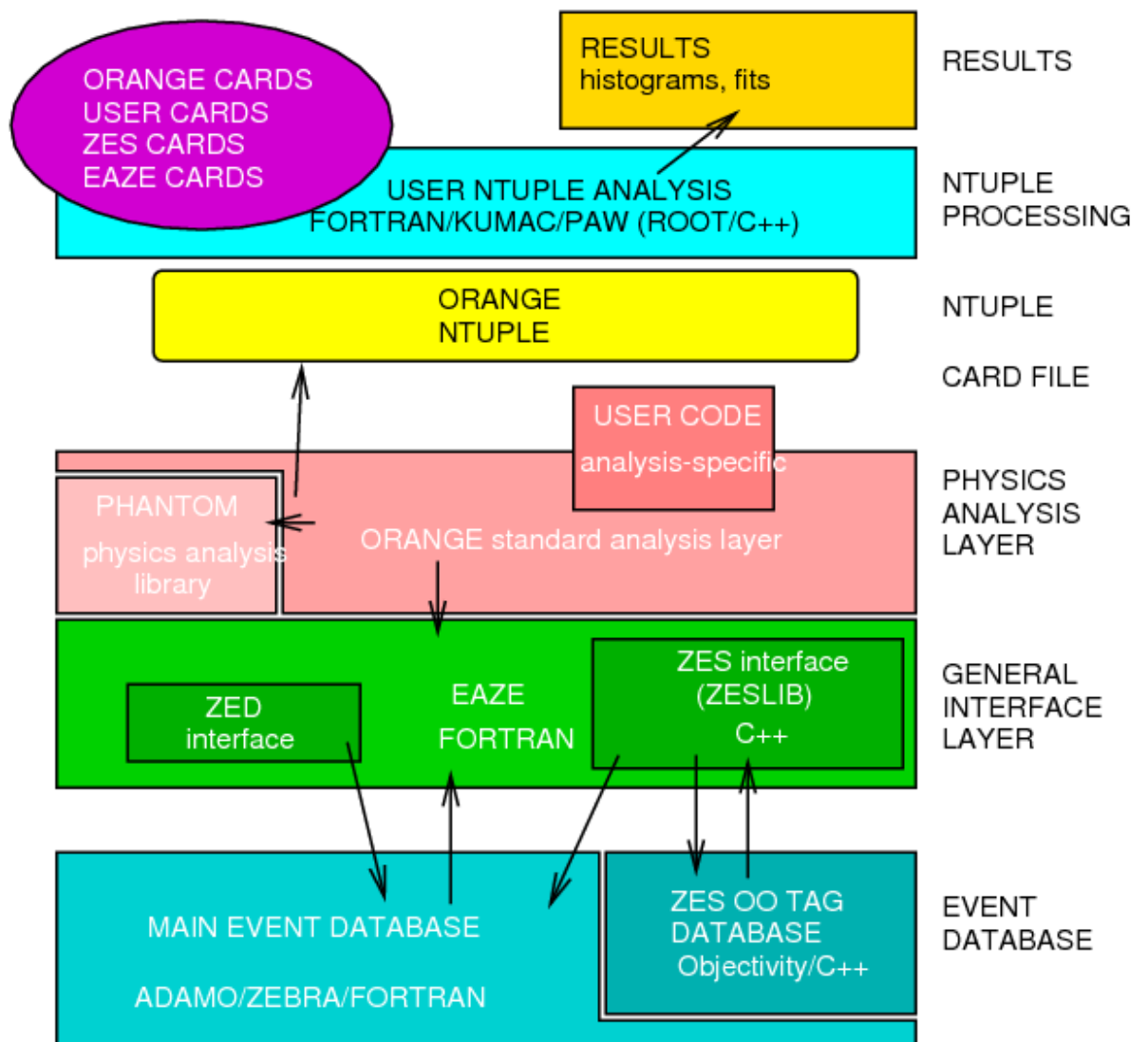


**Figure 3.15:** The ZEUS Analysis Environment

### 3.4.3.1 ORANGE

To a large extent ZEUS analyses are similar to each other -- there are many tasks which must be done in each one of them in similar ways. These include not just initialisation and termination, but also the bulk of the particle and jet finding and corrections. That is, there are many areas for which a consensus has been reached on the best techniques to use for performing each task [58].

ORANGE (Overlying Routine for Analysis Ntuple Generation) is a new way to do analysis. It is a software library which, when activated, executes a user-selected subset of a broad core set of analysis routines -- the ones most commonly called by ZEUS analysis jobs. It is available to all ZEUS users as a standard ZSMSM software package -- it only needs to be activated using the appropriate control card [58].

It is sufficiently broad in scope to be able to form the basis of almost all new analyses started within ZEUS. It is designed to take care of typically 90% of the common calls made by an analysis, allowing the user to concentrate on developing the 10% of user code which is specific to his analysis (which is then linked with ORANGE during compilation).

The user selects which routines are executed by means of control cards, and the results of the calculations may be written to a user-configurable ntuple of any chosen size. In this way the user is able to quickly obtain results and avoids much of the time-consuming effort required to write an analysis job from scratch. This will make analysis in ZEUS simpler, more reliable and more easily reproducible [58].

The ORANGE ntuple is made up of blocks of variables. These are described in the ntuple documentation which appears with each release and. The VOlite and the

Tracking block that we were used during the events reconstruction and selections in Section 3.5 were took from this ORANGE ntuple blocks.

#### 3.4.4 Monte Carlo and Events Simulation

Monte Carlo methods are very important in computational physics, physical chemistry and related applied fields. It has diversified applications from complicated quantum chromodynamics calculations to designing heat shields and aerodynamic forms.

In experimental particle physics, Monte Carlo (MC) simulations were used to evaluate the efficiency for selecting events, to estimate the background rate, to determine the accuracy of the kinematic reconstruction, and to extrapolate the measured cross section to the full kinematic range. Samples of MC events were produced to determine the response of the detector, to correct the data to the hadron level and to compute predictions to be compared to the measurements. A sufficient number of events were generated to ensure that statistical uncertainties from MC samples were negligible in comparison to those of the data [55].

A program based on GEANT [33] was used to simulate the ZEUS detector response. The generated events were passed through the simulated detector, subjected to the same trigger requirements as the data, and processed by the same reconstruction programs [51].

The vertex distribution is an important input to the MC as this is necessary to estimate the event selection efficiency. The latter is strongly correlated with the  $z$ -coordinate of the event vertex, as the reconstructed values of  $Q^2$ ,  $E_T$  and other quantities depend on the measured vertex position. The uncertainty in the shape of the vertex  $z$ -distribution is related to the fraction of  $ep$  collisions from RF buckets adjacent

to that containing the main proton beam. The effect of this uncertainty on the normalization of the data sample in the vertex range -50 to +50 cm is estimated to be less than 0.4% [51].

There are several MC models in the ZEUS experiments including HERACLES, DJANGO, LEPTO, ARIADNE, MEPS and JETSET. The HERACLES simulate NC and CC  $ep$  interactions (using parameterizations of structure functions or parton densities) with radiative corrections: single photon emission from the lepton line, self-energy corrections and the complete set of one-loop weak corrections can be included [50]. The DJANGO model simulate interface between HERACLES (QED corrections to order  $\alpha_{QED}$ ) and LEPTO/ARIADNE (QCD matrix elements and parton showers/colour dipole radiation) to give complete  $ep$  events [50].

The ARIADNE is a program for simulation of QCD cascades implementing the color dipole model [50] and the LEPTO model simulate deep inelastic lepton-nucleon scattering based on LO electroweak cross sections (incl. lepton polarization), first order QCD matrix elements, parton showers and Lund hadronization giving complete events. Soft colour interaction model gives rapidity gap events [50]. The JETSET model simulates the Lund string model for hadronization of parton systems [50].

Using the HERACLES 4.5.2 [3] program with the DJANGO 6 2.4 [22], the neutral current Deep Inelastic Scattering events including radiative effects are simulate. DJANGO interface between HERACLES (QED corrections to order  $\alpha_{QED}$ ) and LEPTO/ARIADNE (QCD matrix elements and parton showers/colour dipole radiation) to give complete  $ep$  events [50]. In HERACLES, corrections for initial and final state radiation, vertex and propagator corrections, and two-boson exchange are included. The QCD cascade and the hadronic final state are simulated using the color-dipole model of ARIADNE 4.08 [23] and as a systematic check, with the MEPS model of LEPTO 6.5

[15]. Both programs use the Lund string model of JETSET 7.4 [38] for the hadronization.

#### **3.4.4.1 The Lund String Fragmentation Model in JETSET**

The Lund String Fragmentation Model is implemented in the JETSET Monte Carlo packet in order to model the hadronization process in parton systems and contains a set of simple assumptions [48]. In this string model, the hadronization is described by several string breaks-up whereby quark-antiquark ( $q\bar{q}$ ) or diquark-antidiquark ( $D\bar{D}$ ) pairs are created at two ends of each string break-up. The hadron was formed when quarks or antiquarks combined with other neighbouring pairs by color force.

In JETSET Monte Carlo packet, the popcorn and diquarks (defined in Section 2.6) was two main mechanisms used to describe the hadronization process.

#### **3.4.4.2 Event Generators**

##### **3.4.4.2.1 ARIADNE/DJANGO**

DJANGO is a Monte Carlo event generator that was designed specifically to simulate lepton proton collision. It includes the program HERACLES, which generates Neutral Current DIS events. The DJANGO generator is incorporated into the ARIADNE program.

## 3.5 Events Reconstruction & Selection

### 3.5.1 Events Reconstruction

#### 3.5.1.1 Deep Inelastic Scattering (DIS) Events Reconstruction

ZEUS provided several methods to reconstruct the DIS event variables namely  $Q^2$ ,  $x$  and  $y$ . The three main methods that are generally used for this thesis studies are the Electron method (e), the Jacquet-Blondel method (JB) [12] and the Double Angle method [21,36]. The Electron method depends exclusively on the measurement of the scattered electron, and is very sensitive to the initial state radiation where a photon is emitted by the incident electron.

The Jacquet-Blondel method relies entirely on the measurement of the energies of all hadronic system (also known as the hadron method). Lastly, the Double Angle method takes information from both the scattered electron and hadronic final system for the event variable reconstruction process.

- The Electron method

The electron method uses the energy  $E_{e'}$  and the polar angle  $\theta$  of the scattered electron (please refer Figure 3.10) :

$$Q_e^2 = 2E_e E_{e'}(1 + \cos \theta_{e'}) \quad (3.1)$$

$$x_e = \frac{E_e}{E_p} \frac{E_{e'}(1 + \cos \theta_{e'})}{2E_e - E_{e'}(1 - \cos \theta_{e'})} \quad (3.2)$$

$$y_e = 1 - \frac{E_{e'}}{2E_e}(1 - \cos \theta_{e'}) \quad (3.3)$$

- The Jacquet-Blondel (JB) method

This method allows the reconstruction of the event kinematics purely from the hadronic system, particularly for the photoproduction process, where the electron is not detected as it continues down the beam pipe. The variables are estimated as follows:

$$Q_{JB}^2 = \frac{(\sum p_x)_h^2 + (\sum p_y)_h^2}{1 - y_{JB}} \quad (3.4)$$

$$x_{JB} = \frac{Q_{JB}^2}{s y_{JB}} \quad (3.5)$$

$$y_{JB} = \frac{\sum (E - p_z)_h}{2E_e} \quad (3.6)$$

where the sum here ideally runs over final state particles, but in practice runs over calorimeter cells or some other measurement of the final state momenta.

- The Double Angle method

The double angle method is based on the scattering angle of the electron  $\theta_e$  and the polar angle  $\gamma_h$  of an object to conserve the four momentum of the outgoing electron (Please refer Figure 3.10) . This avoids, to first order, any dependence on the energy scale of the calorimeter:

$$\cos \gamma_h = \frac{(\sum p_x)_h^2 + (\sum p_y)_h^2 - (\sum (E - p_z))_h^2}{(\sum p_x)_h^2 + (\sum p_y)_h^2 + (\sum (E - p_z))_h^2} \quad (3.7)$$

$$Q_{DA}^2 = 4E_e^2 \frac{\sin \gamma_h (1 + \cos \theta_e)}{\sin \gamma_h + \sin \theta_e - \sin(\gamma_h + \theta_e)} \quad (3.8)$$

$$x_{DA} = \frac{E_e}{E_p} \frac{\sin \gamma_h + \sin \theta_e + \sin(\gamma_h + \theta_e)}{\sin \gamma_h + \sin \theta_e - \sin(\gamma_h + \theta_e)} \quad (3.9)$$

$$y_{DA} = \frac{\sin \theta_e (1 - \cos \gamma_h)}{\sin \gamma_h + \sin \theta_e - \sin(\gamma_h + \theta_e)} \quad (3.10)$$



where  $\sum$  is the sum over all hadronic cells  $h$  in the calorimeter with four-momentum  $(E, p_x, p_y, p_z)$ .

The offline selection of charged currents in DIS events was characterized by the scattered electron detected in the central tracking detector (CTD) [27,9,43], which operated in a magnetic field of 1.43T provided by a thin superconducting coil.

### 3.5.2 Events Selection

The data used in this analysis were HERA-II data, collected during the running period between 2003 and 2007 when HERA operated with protons of energy  $E_p = 920$  GeV and electrons of energy  $E_e = 27.5$  GeV, and correspond to an integrated luminosity of  $4.60 \text{ pb}^{-1}$  and center-of-mass energy  $\sqrt{s} = 318$  GeV. The criteria to select DIS events are described below.

During the events selection, there were two steps involves. The first step is the online selection, where this is the real time process, the decision that has been made is irreversible and the data will be lost forever. The second step is the offline selection, where in this process, decisions can be reconsidered and the data can be and is frequently processed.

#### 3.5.2.1 Online Event Selection

During the online events selection, ZEUS operates a three-level trigger system [44] to pick the interesting physics events. It relied on the presence of an energy deposition in the CAL compatible with that of a scattered electron. At the first-level trigger, only

coarse calorimeter and tracking information is available. Events were selected using criteria based on an energy deposit in the CAL consistent with an isolated positron. In addition, events with high transverse energy,  $E_T$  in coincidence with a CTD track were accepted [55].

At the second level, a requirement on Energy-Momentum conservation,  $\delta$  was used to select NC DIS events and timing information from the calorimeter was used to reject events not in agreement with the bunch-crossing time. At the third level, events were fully reconstructed on a computer farm. The requirements were similar to, but looser than the offline cuts described below [55].

### **3.5.2.2 Offline Event Selection**

During the offline events selection, the neutral current Deep Inelastic Scattering events were characterized by the scattered electron/positron detected in the uranium scintillator calorimeter, CAL by using Sinistra blocks. Sinistra is a neural-network based electron finder [24] and an electron finder is a piece of software that finds electrons. Only good photon and electron/positron candidates are identified using Sinistra. However, the goal of electron finders is not just to find any electron but the scattered electron. The electron finder looks for certain detector signatures which a priori are not unique to electrons.

#### **3.5.2.2.1 High $Q^2$ DIS**

High  $Q^2$  Deep Inelastic Scattering events were selected by considering the following:-

- i) To reject the photoproduction events where the scattered electrons have lower energy, the following cuts were applied:-

- At least one electron found by Sinistra with probability  $> 0.9$ . A scattered electron is the characteristic signature of DIS events. This is to make sure that the events are not photoproduction events.
  - The energy of the scattered electron,  $E_e$  must be  $\geq 10$  GeV. This cut ensures a high reconstruction efficiency and purity of the scattered electrons. The presence of the scattered electron in the main detector also suppresses the photoproduction background;
  - Cuts on Energy-Momentum conservation;  $38 \leq \delta \leq 65$  GeV, where  $\delta = \sum (E_i - P_{z_i})$  and  $E_i$  is the energy of the  $i$ -th CAL cell,  $P_{z_i}$  is the momentum along the  $z$ -axis and the sum runs over all CAL cells. This cut will eliminate the background from photoproduction events and events with initial-state radiations. If there is no track associated with the electron, the cut is raised to  $\delta > 44$  GeV.
  - Cut on energy in a cone of  $\eta - \phi$  of radius 0.8 around electron not from electron  $\leq 5$  GeV.
- ii) To reduce the background from events not originating from  $ep$  collisions, the following cuts were included:-
- $|z_{vertex}| < 50$  cm, where  $z_{vertex}$  is the  $z$  component of the position of the primary vertex. The beams collide at a nominal value of  $z = 0$  with a Gaussian spread  $\sigma \sim 12$  cm. This cut therefore reduces beam-gas background events and events with an incorrectly measured vertex.
  - An electron track is required if the electron was found in the main detector region or outside this region but with  $\delta > 44$  GeV. The main detector covering the polar angle  $\theta_e$  where  $17.2^\circ \leq \theta_e \leq 150^\circ$ . This aids the correct electron identification in the region of good tracking acceptance. It removes background from halo muons, cosmic rays and good physics events with misidentified scattered electron.

iii) To remove events where fake electrons are found in FCAL;

- $y_e \leq 0.95$ , where  $y_e$  is the inelasticity estimated from the energy and angle of the scattered electron, shown in equation 3.3. This cut also defines one boundary of the kinematic region.

iv) To improve the accuracy of the DA reconstruction;

- $y_{JB} \geq 0.04$ , where  $y_{JB}$  is the inelasticity, estimated using the Jacquet-Blondel method [12], shown in equation 3.6. Below this value, a significant fraction of the hadronic system is lost, hence requiring a more detailed simulation of the beam pipe region than currently exist.

v) The high  $Q^2$  DIS events were restricted to events with  $Q_{DA}^2 > 25 \text{ GeV}^2$ . The  $Q^2$  separation allows the dependence of many measurements on the hard scattering process to be investigated.

#### 3.5.2.2.2 Low $Q^2$ DIS

The same selection criteria were used to select the low  $Q^2$  Deep Inelastic Scattering events, except for the cut on  $Q^2$  which was instead as follow:-

- $5 < Q_{DA}^2 < 25 \text{ GeV}^2$

# CHAPTER 4

## Tracking Enhancement with the Micro Vertex Detector (MVD)

### 4.1 Introduction

The tracking information from the MVD was used to observe the effect on the strange particles production. This extra tracking information was used during the observation of  $\Lambda$  baryons and  $K_s^0$  mesons production at the ZEUS detector.

The presence of  $\Lambda$  baryons and  $K_s^0$  mesons produced at the ZEUS detector, and the effect of using MVD tracking information to find tracks in addition to the CTD were studied. The overall performance of the tracking at ZEUS with addition of the Micro-Vertex Detector (MVD) is also of interest to many other ZEUS analyses, particularly those involving heavy flavors.

The MVD was part of the ZEUS experiment and had been in operation since the luminosity upgrade in 2000-2001 [42]. It had been operating reliably in the HERA-II run period. The aim of the HERA luminosity upgrade was to increase the design luminosity from  $1.5 \times 10^{31} \text{ cm}^{-2}\text{s}^{-1}$  to about  $7 \times 10^{31} \text{ cm}^{-2}\text{s}^{-1}$ , which was almost reached at the current run period then [46].

Unfortunately, this luminosity upgrade resulted in a large amount of background beam gas events and synchrotron radiation such that the experiment needed to be modified to take useful physics data. This was perhaps due to the increasing multiple

scattering process due to the additional material from the MVD. Finding the configuration of the experiment that gets the most physics with least background is obviously very important, especially the operating condition of the central tracking detector (CTD). We need a direct test of MVD's effectiveness without patchwork due to the luminosity upgrade.

The neutral strange particles  $K_s^0$ ,  $\Lambda$  and  $\bar{\Lambda}$  have a distinctive secondary vertex signature, for which good tracking ability is important for their observation. They are produced in abundance in the  $ep$  collisions in ZEUS [39]. As such, they provide a good test ground for this analysis. Information from the MVD is combined with other tracking detector such as the central tracking drift chamber (CTD). This enables us to achieve a high precision estimate of track trajectory parameters at the interaction point and greatly improving the resolution for the reconstructed vertices [25]. The design of the MVD was described briefly in Section 3.3.1.

## 4.2 V0lite's Reconstruction

### 4.2.1 Tracking

The tracking detectors, the CTD and MVD were the main components of the ZEUS detector that are used in this analysis. The information for these detectors was described briefly in Section 3.2.1 and Section 3.3.1. The MVD allows a closer look at the primary vertex which reveals in the direct neighborhood satellite vertices with few tracks. The momentum of the particles can be measured via their curvature due to the existence of an axial magnetic field of 1.43T around both of the CTD and MVD.

The same selection criteria were used to select the events for this analysis as in Section 3.5.1 and Section 3.5.2, except with additional steps for the tracks selection in the MVD. The V0lite block was used because it gives us the information of the daughter particles. The type of the tracks in the MVD must be ZTT (ZEUS software track finding packages) type with at least 2 hits in the MVD for both  $p$  and  $\pi$  for  $\Lambda + \bar{\Lambda}$  baryons and  $\pi^+\pi^-$  for  $K_s^0$  meson.

For accurate invariant mass reconstruction, the momentum vectors need to be given at the decay vertex. All tracks used in invariant mass reconstruction must be vertex tracks.

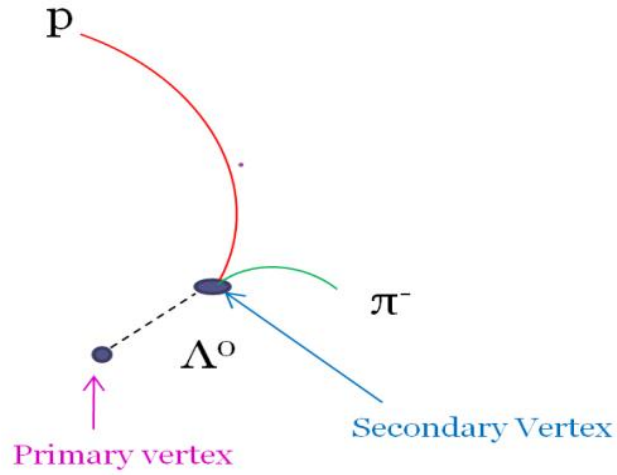


**Figure 4.1:** Hadronic decay modes of  $\Lambda$

### 4.3 Signal to Background Ratio

In order to study the performance and the effect of MVD tracking information in the production of strange particles, the signal to background ratio were investigated. The signal to background ratio of  $\Lambda$ ,  $\bar{\Lambda}$ ,  $\Lambda + \bar{\Lambda}$  baryon and  $K_s^0$  meson has been measured and shown in Table 4.1 and compared to MC prediction from ARIADNE.

KINEMATICS RANGES	PARTICLES	DATA	MVD + CTD	CTD
Low $Q^2$ DIS	$\Lambda + \bar{\Lambda}$	ZEUS 2003 & 2007	$5.01 \pm 0.25$	$3.73 \pm 0.10$
		ARIADNE	$7.30 \pm 0.20$	$4.76 \pm 0.06$
	$\Lambda$	ZEUS 2003 & 2007	$6.67 \pm 0.42$	$4.66 \pm 0.16$
		ARIADNE	$7.08 \pm 0.27$	$4.84 \pm 0.08$
	$\bar{\Lambda}$	ZEUS 2003 & 2007	$5.73 \pm 0.39$	$4.70 \pm 0.16$
		ARIADNE	$7.79 \pm 0.30$	$4.69 \pm 0.08$
	$K_s^0$	ZEUS 2003 & 2007	$10.77 \pm 0.31$	$8.78 \pm 0.12$
		ARIADNE	$13.69 \pm 0.21$	$11.21 \pm 0.07$
High $Q^2$ DIS	$\Lambda + \bar{\Lambda}$	ZEUS 2003 & 2007	$3.06 \pm 0.30$	$2.26 \pm 0.10$
		ARIADNE	$4.91 \pm 0.25$	$2.89 \pm 0.06$
	$\Lambda$	ZEUS 2003 & 2007	$3.45 \pm 0.44$	$2.57 \pm 0.16$
		ARIADNE	$4.88 \pm 0.33$	$3.00 \pm 0.09$
	$\bar{\Lambda}$	ZEUS 2003 & 2007	$2.90 \pm 0.41$	$2.06 \pm 0.13$
		ARIADNE	$5.55 \pm 0.39$	$2.80 \pm 0.09$
	$K_s^0$	ZEUS 2003 & 2007	$16.15 \pm 0.65$	$7.26 \pm 0.16$
		ARIADNE	$10.40 \pm 0.27$	$8.61 \pm 0.09$

**Table 4.1:** The signal to background ratio for the MVD+CTD compared to the CTD. The performance of the MVD+CTD detector is better than the CTD only detector.

#### 4.4 Discussion and Conclusion.

$K_s^0$  mesons,  $\Lambda$ ,  $\bar{\Lambda}$  and  $\Lambda + \bar{\Lambda}$  baryons have been found at the ZEUS detector. The effect of using MVD to find tracks in addition to the CTD has been investigated. By studying the MVD effect, we can compare the performance of MVD + CTD in tracking charged particle compared to the performance of CTD only.

For Low  $Q^2$  DIS events, the background for the events with MVD cuts got to be the small values of background to signal ratio compared to the mass plot without MVD cut and for the High  $Q^2$  DIS events, cuts on MVD give improvements for both meson and baryon production.



The signal to background ratio in Table 4.1 shows that the number of particles produced after the MVD cuts applied was higher than the value before the cuts. It proved that the performance of using the MVD as the extra tracking information gives a higher number of strange particles production compared to the CTD only.

In conclusion, the MVD improves the tracking information and gives a good result to find tracks in addition to the CTD in the ZEUS detector. The performance of MVD + CTD in tracking charged particle is better than the performance of CTD only. The number of strange particle produced with this additional MVD tracking information was higher than the previous CTD only tracking information. Micro Vertex Detector (MVD) improves tracking resolution and allows us to reconstruct strange particles decay vertex.

# CHAPTER 5

## $\Lambda$ and $K_s^0$ Selection

### 5.1 Strange Particle Reconstruction

The neutral strange hadrons have a distinctive secondary vertex signature, for which good tracking ability is crucial for their observation. They are produced in abundance in the  $ep$  collisions in ZEUS. Strange hadrons are relatively easy to identify in ZEUS detector using CTD due to their long lifetime and light masses. The particles considered in this analysis are  $\Lambda$ ,  $\bar{\Lambda}$  and  $K_s^0$  whose properties are listed in Table 5.1.

	Contents	Mass (MeV)	$I(J^P)$	$c\tau$ (cm)	Decay Mode (BR %)
$K_s^0$	$d\bar{s}/\bar{d}s$	$497.672 \pm 0.031$	$\frac{1}{2}(0^-)$	2.6786	$\pi^+\pi^-$ ( $68.6 \pm 0.3$ )
$\Lambda(\bar{\Lambda})$	$uds(\bar{u}d\bar{s})$	$1115.683 \pm 0.006$	$0(\frac{1}{2}^+)$	7.89	$p\pi$ ( $63.9 \pm 0.5$ )

**Table 5.1:** Properties of the strange particles

The following decay modes of  $\Lambda$  and  $K_s^0$  were observed;

$$\Lambda \rightarrow p\pi^- \quad (5.1)$$

$$\bar{\Lambda} \rightarrow \bar{p}\pi^+ \quad (5.2)$$

$$K_s^0 \rightarrow \pi^+\pi^- \quad (5.3)$$

The identification of strange particles requires the presence of tracks and the subsequent combination of tracks into secondary vertices.

## 5.2 Track Reconstruction

The vertex and track finding for ZEUS is performed by VCTRACK software package. A full description of the track reconstruction program can be found elsewhere [13]. VCTRACK is a FORTRAN package which finds tracks, the primary vertex, and secondary vertices for events in the ZEUS experiment at HERA. Each reconstructed track must use CTD hits, although information from other tracking detectors may also be exploited.

The events were required to have at least one strange hadrons candidates, decay to two charged particles. The candidates were recognized by choosing pairs of oppositely charged tracks, fitted to a displaced secondary vertex.

## 5.3 Identification of $\Lambda \rightarrow p\pi^-$ ( $\bar{\Lambda} \rightarrow \bar{p}\pi^+$ ) candidates

Since  $\Lambda(\bar{\Lambda})$  is a neutral hadron, it cannot be observed directly by the CTD or MVD. However, it can be observed through its decay products, a proton and a  $\pi^-$ . These charged decay products are visible to the CTD and MVD. The  $\Lambda(\bar{\Lambda})$  baryon is a weakly decaying particle with a lifetime of the order of  $10^{-10}$  sec. If a  $\Lambda(\bar{\Lambda})$  is produced with a small GeV energy, then it will travel several cm before decaying, and a distinct secondary vertex can be seen. During the reconstruction of  $\Lambda(\bar{\Lambda})$  candidates, all secondary vertex tracks were taken into account. In order to limit the combinatorial

background and remove poorly measured secondary vertices, secondary vertex tracks are required to satisfy the following constraints:-

- The first requirement on events is that there is at least one secondary vertex;
- The secondary vertex is required to have exactly two oppositely charged tracks coming from it. The proton or antiproton mass were assigned to the track with larger momentum and the pion mass to the other track for each V0lite candidate in order to reconstruct the  $\Lambda(\bar{\Lambda})$ 's;
- In order for the algorithms to reconstruct the secondary tracks with an enhanced resolution, and to restrict the study of the CTD region where track acceptance is high, the tracks fitted to this secondary vertex were obligatory to pass through at least the 3<sup>rd</sup> superlayer of the Central Tracking Detector;
- $p_T(\pi, p) > 0.15$  GeV: The transverse momentum,  $p_T$  of the tracks from the secondary vertex must be greater than 0.15 GeV. This is because the tracks with smaller  $p_T$  are not well measured, as the tracks are caused to spiral by the B field so close to the beam axis as not to leave the CTD;
- $|\eta(\pi, p)| < 1.75$ : The value for absolute pseudorapidity was required to be less than 1.75;

The momentum of the original decaying particle is then calculated to be the vector sum of the momenta of the two secondary tracks. The momentum at the vertex is then required to satisfy the following criteria:

- $0.6 < p_T(\Lambda, \bar{\Lambda}) < 2.5$  GeV, where  $p_T(\Lambda, \bar{\Lambda})$  indicate the transverse momentum of the reconstructed candidate in the laboratory frame;
- $|\eta(\Lambda, \bar{\Lambda})| < 1.2$ , where  $\eta(\Lambda, \bar{\Lambda})$  is the pseudorapidity of the reconstructed candidate in the laboratory frame;

The  $p_T(\Lambda, \bar{\Lambda})$  and  $\eta(\Lambda, \bar{\Lambda})$  selection criteria were determined by studying the reconstruction efficiency and acceptance in different  $p_T$  and  $\eta$  regions. The  $\Lambda$  invariant mass,  $M(p\pi^-)$  and  $\bar{\Lambda}$  invariant mass,  $M(\bar{p}\pi^+)$  is derived from the reconstructed four-momentum of the V0like candidate. Additional requirements to select  $\Lambda(\bar{\Lambda})$  are given in the following:

- $M(e^+e^-) > 0.05$  GeV: To remove electron pairs from photon conversions and photon conversions to  $e^+e^-$  are removed by requiring the invariant mass of the electron is greater than 50 MeV. Electron pair production from photon conversion is a type of background to the strange particle reconstruction;
- $M(\pi^+\pi^-) > 0.475$  GeV was applied to remove  $K_s^0$  contamination from the  $\Lambda(\bar{\Lambda})$  signal. In order to qualify as a  $\Lambda$  candidates, the mass must lie within  $1.112 < M(\Lambda) < 1.121$  GeV.

Figure 5.1 shows the  $\Lambda$ ,  $\bar{\Lambda}$  and  $\Lambda + \bar{\Lambda}$  invariant mass distributions reconstructed for the high  $Q^2$  events after these requirements. The mass peak of the reconstructed  $\Lambda$ ,  $\bar{\Lambda}$  and  $\Lambda + \bar{\Lambda}$  is around 1.116 GeV. Figure 5.2 shows the  $\Lambda$ ,  $\bar{\Lambda}$  and  $\Lambda + \bar{\Lambda}$  invariant mass distributions reconstructed for the low  $Q^2$  events. The mass peak of the reconstructed  $\Lambda$ ,  $\bar{\Lambda}$  and  $\Lambda + \bar{\Lambda}$  is around 1.116 GeV. A small background is observed for both kinematic regions.

In order to fit the whole region of the histogram, we use a second order polynomial function plus a Gaussian function. To perform the fit on the invariant mass distribution, the following parameterization was used:

$$f(x) = a_0 e^{\frac{-(x-a_1)^2}{(2a_2)^2}} + \text{Polynomial function} \quad (5.4)$$

The number of observed particles,  $N_{particles} = \int f(x)dx = \frac{\sqrt{2\pi}a_0' a_2}{w}$

where  $a_0$  and  $a_2$  represent the values of the zero and second parameters, respectively and  $w$  represents the bin width.

Substitute  $a_0' \equiv \frac{a_0}{\sqrt{2\pi}a_2}$

So,  $f(x) = (\frac{a_0}{\sqrt{2\pi}a_2})e^{\frac{-(x-a_1)^2}{(2a_2)^2}} + a_3 + a_4x + a_5x^2$

$a_0, a_1$  and  $a_2$  are the fit parameters of the Gaussian distribution, where  $a_0$  is the height of the peak,  $a_1$  is the peak position of the Gaussian and  $a_2$  is the bin width of the histogram. The number of observed particles under the Gaussian distribution can then be found by

$$N_{particles} = \int f(x)dx = \frac{a_0}{w} \quad (5.5)$$

where  $a_0$  is the value of the zero Gaussian parameter after the fitting process and  $w$  is the bin width of the histogram.

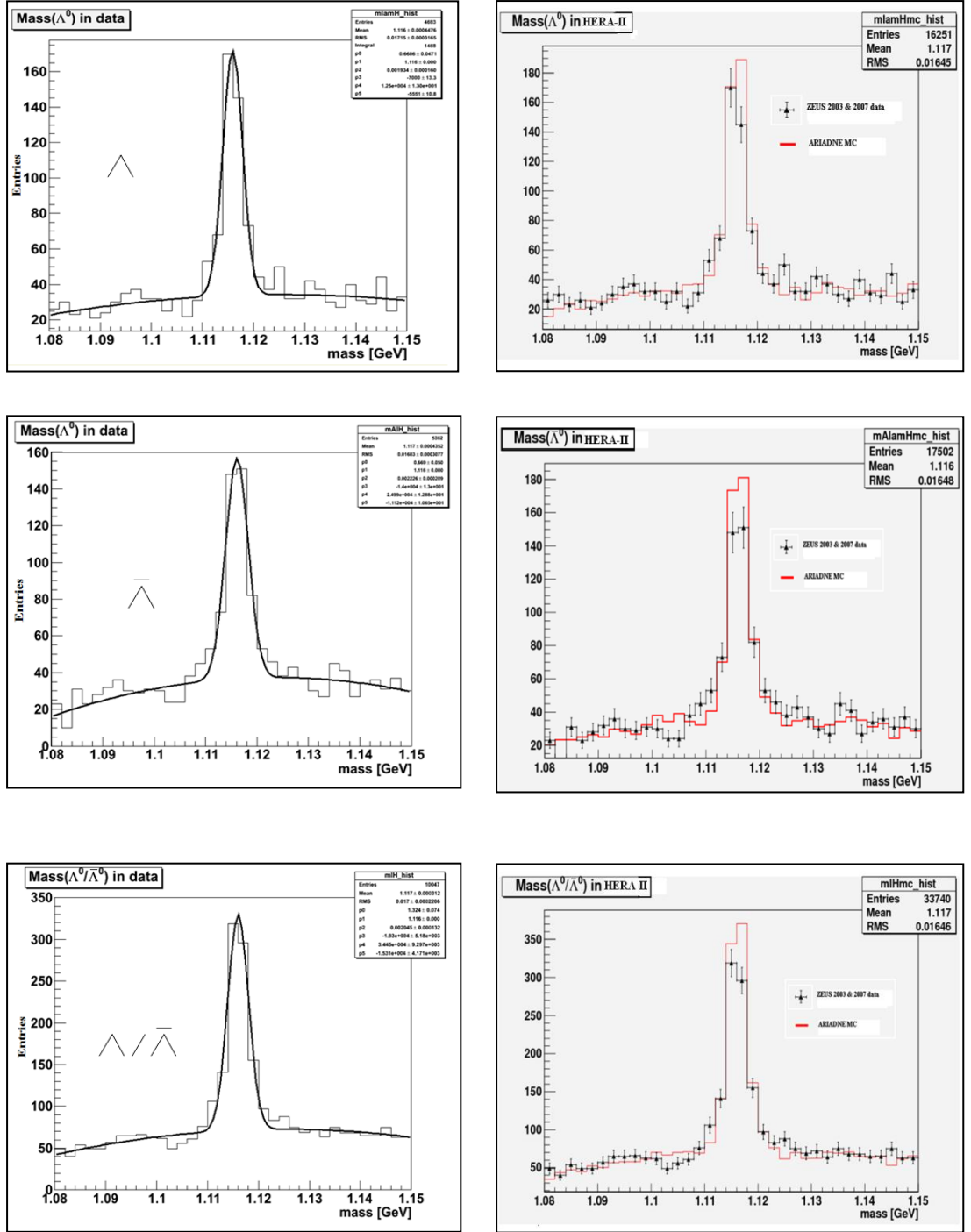


**Figure 5.1:** The  $\Lambda$ ,  $\bar{\Lambda}$  and  $\Lambda + \bar{\Lambda}$  invariant mass distribution for the high  $Q^2$  DIS events. Histograms on the left side represent the invariant mass plot for ZEUS data where the solid curve represents the fit of a Gaussian for the signal combined to a second order polynomial function for the background. The MC is normalized to the data and represents by the red line while the pulse represents the ZEUS data, is shown by the histograms on the right side.

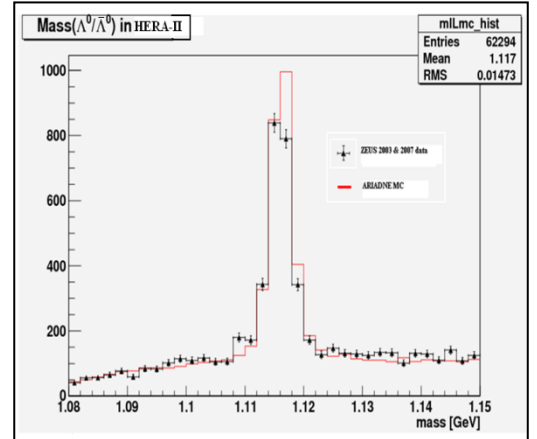
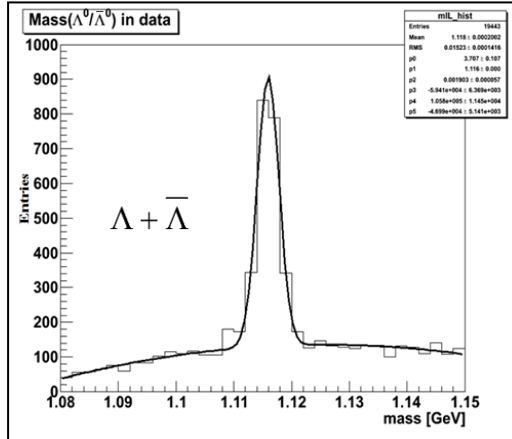
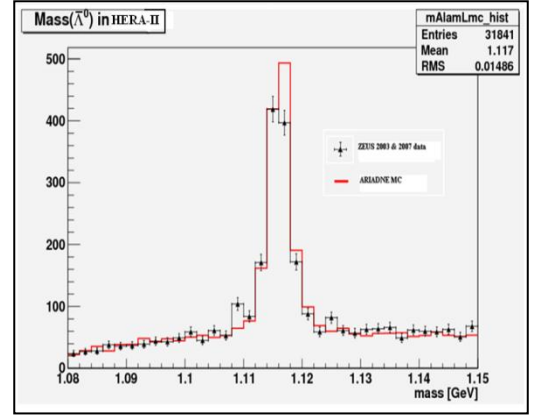
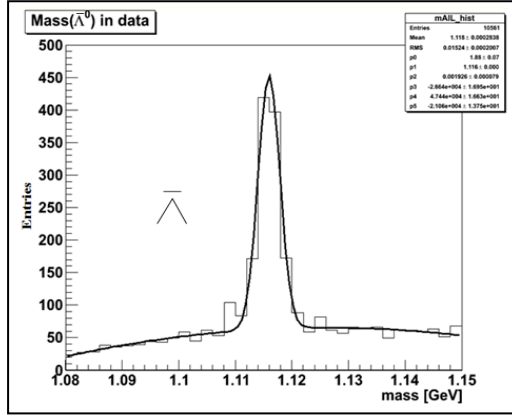
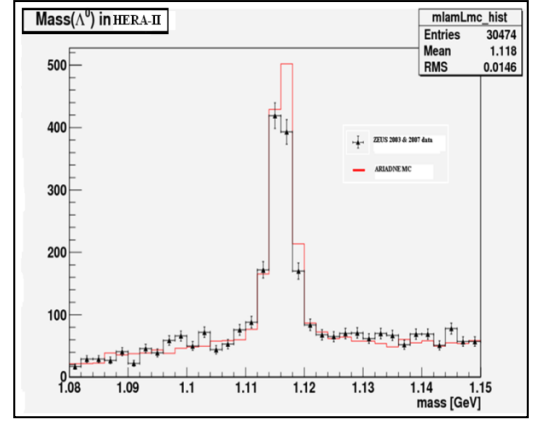
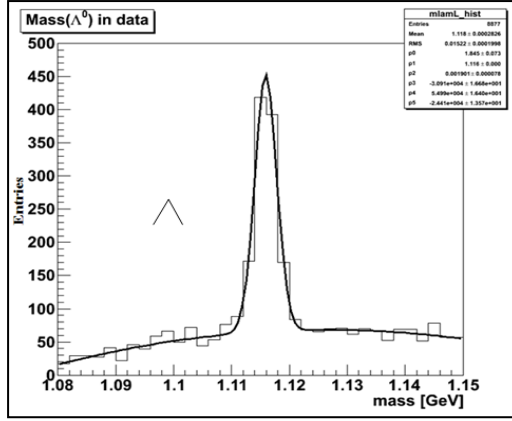


**Figure 5.2:** The  $\Lambda$ ,  $\bar{\Lambda}$  and  $\Lambda + \bar{\Lambda}$  invariant mass distribution for the low  $Q^2$  DIS events. Histograms on the left side represent the invariant mass plot for ZEUS data where the solid curve represents the fit of a Gaussian for the signal combined to a second order polynomial function for the background. The MC is normalized to the data and represents by the red line while the pulse represents the ZEUS data, is shows by the histograms on the right side.



#### 5.4 Identification of $K_s^0 \rightarrow \pi^+\pi^-$ candidates

For the  $K_s^0$  identification, only  $K_s^0$  candidates decaying into  $\pi^+\pi^-$  with branching ratio  $68.6 \pm 0.27\%$  were reconstructed. Both tracks from the same V0lite block were assigned as the mass of the charged pion. Additional requirements are listed below:

- $0.6 < p_T(K_s^0) < 2.5$  GeV, where  $p_T(K_s^0)$  indicate the transverse momentum of the reconstructed candidate in the laboratory frame;
- $|\eta(K_s^0)| < 1.2$ , where  $\eta(K_s^0)$  is the pseudorapidity of the reconstructed candidate;
- $M(p\pi) > 1.121$  GeV was applied to remove  $\Lambda/\bar{\Lambda}$  impurity from the  $K_s^0$  signal. Here the proton mass was apportioned to the track with larger momentum and the pion mass to the other track. In order to qualify as a  $K_s^0$  candidates, the mass must lie within  $0.48 < M(K_s^0) < 0.52$  GeV.
- $M(e^+e^-) > 0.05$  GeV: To exclude the electron pair production from photons;

Figure 5.3 shows the  $K_s^0$  invariant mass distributions reconstructed for the high  $Q^2$  events after these requirements. The mass peak of the reconstructed  $K_s^0$  is around 0.4977 GeV. Figure 5.4 shows the  $K_s^0$  invariant mass distributions reconstructed for the low  $Q^2$  events. The mass peak of the reconstructed  $K_s^0$  is around 0.4979 GeV. Small backgrounds are observed for both kinematic regions.

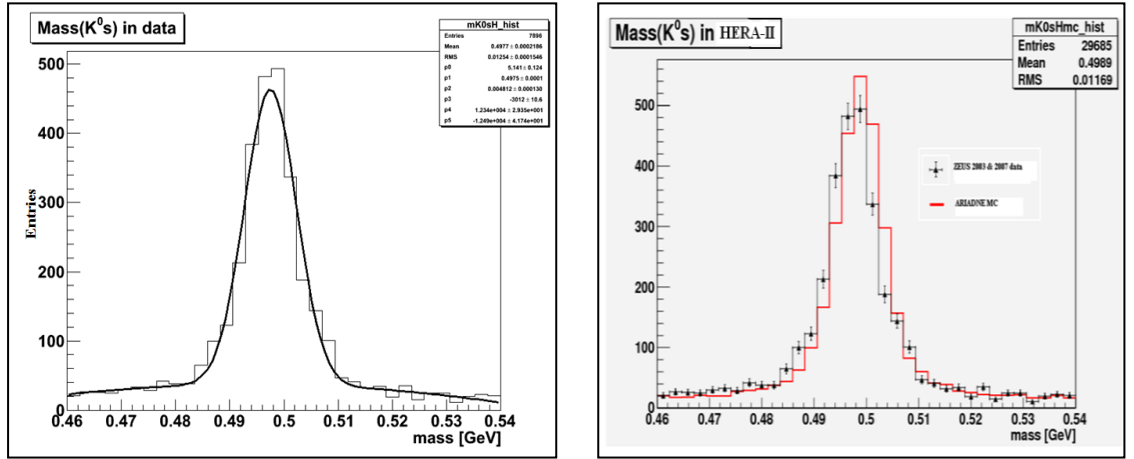


**Figure 5.3:** The  $K_s^0$  mass distribution for the high  $Q^2$  DIS events. The histogram on the left side represents the invariant mass plot for ZEUS data where the solid curve represents the fit of a Gaussian for the signal combined with a second order polynomial function for the background. The MC is normalized to the data and represents by the red line while the pulse represents the ZEUS data, is shows by the histograms on the right side.

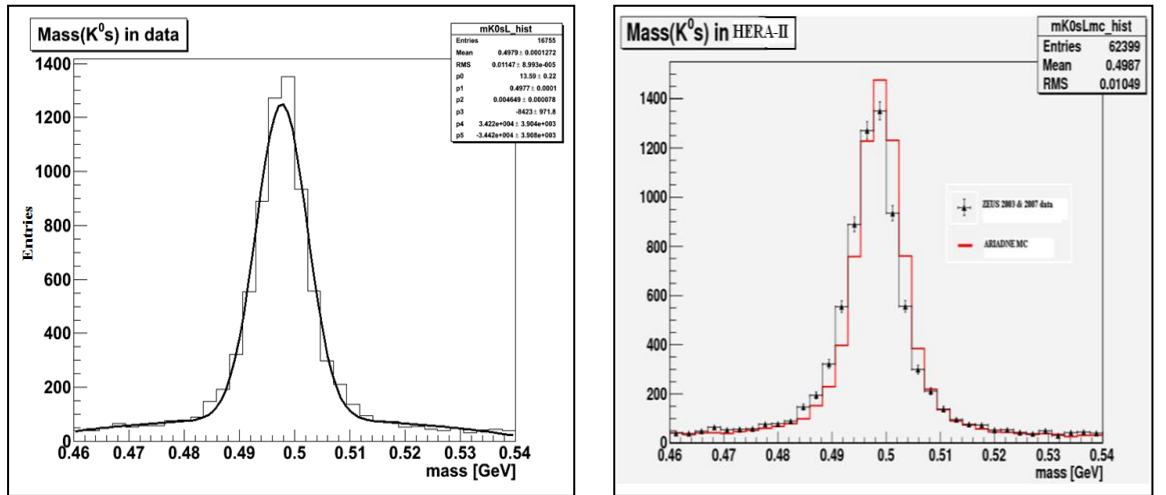


**Figure 5.4:** The  $K_s^0$  mass distribution for the low  $Q^2$  DIS events. The histogram on the left side represents the invariant mass plot for ZEUS data where the solid curve represents the fit of a Gaussian for the signal combined with a second order polynomial function for the background. The MC is normalized to the data and represents by the red line while the pulse represents the ZEUS data, is shows by the histograms on the right side.

Figure 5.1 and Figure 5.3 shows the mass distribution of the secondary vertex candidates in the  $\Lambda$ ,  $\bar{\Lambda}$ ,  $\Lambda + \bar{\Lambda}$  and  $K_s^0$  samples assuming  $p\pi$  and  $\pi\pi$  decays respectively for the high  $Q^2$  DIS events. The figure shows candidates in the range  $|\eta| < 1.2$  and  $0.6 < P_T < 2.5$  GeV for events with  $Q^2 > 25$  GeV<sup>2</sup> and  $0.04 \leq y \leq 0.95$ . The total number of  $\Lambda$ ,  $\bar{\Lambda}$ ,  $\Lambda + \bar{\Lambda}$  and  $K_s^0$  within the peaks are estimated to be  $334.29 \pm 23.55$ ,  $334.52 \pm 24.98$ ,  $661.87 \pm 36.95$  and  $2,187.86 \pm 52.88$  respectively, after background subtraction.

Figure 5.2 and Figure 5.4 shows the mass distribution of the secondary vertex candidates in the  $\Lambda$ ,  $\bar{\Lambda}$ ,  $\Lambda + \bar{\Lambda}$  and  $K_s^0$  samples assuming  $p\pi$  and  $\pi\pi$  decays respectively for the low  $Q^2$  DIS events. The figure shown candidates in the range  $|\eta| < 1.2$  and  $0.6 < P_T < 2.5$  GeV for events with  $5 < Q^2 < 25$  GeV<sup>2</sup> and  $0.04 \leq y \leq 0.95$ . The total number of  $\Lambda$ ,  $\bar{\Lambda}$ ,  $\Lambda + \bar{\Lambda}$  and  $K_s^0$  within the peaks are estimated to be  $922.43 \pm 13.62$ ,  $940.15 \pm 36.55$ ,  $1,853.36 \pm 53.57$  and  $5,781.19 \pm 91.75$  respectively, after the background subtraction. All the information can be found in Table 5.1.

STRANGE HADRONS	KINEMATIC REGIONS	HERA-II DATA	ARIADNE MC
$N(\Lambda)$	Low $Q^2$ DIS	$922.43 \pm 13.62$	$3,868.30 \pm 71.85$
	High $Q^2$ DIS	$334.29 \pm 23.55$	$1,350.68 \pm 45.55$
$N(\bar{\Lambda})$	Low $Q^2$ DIS	$940.15 \pm 36.55$	$3,702.93 \pm 70.60$
	High $Q^2$ DIS	$334.52 \pm 24.98$	$1,318.73 \pm 47.76$
$N(\Lambda/\bar{\Lambda})$	Low $Q^2$ DIS	$1,853.36 \pm 53.57$	$7,570.20 \pm 100.77$
	High $Q^2$ DIS	$661.87 \pm 36.95$	$2,663.33 \pm 67.50$
$N(K_s^0)$	Low $Q^2$ DIS	$5,781.19 \pm 91.75$	$25,243.27 \pm 171.55$
	High $Q^2$ DIS	$2,187.86 \pm 52.88$	$9,652.08 \pm 108.56$

**Table 5.2:** The number of reconstructed strange  $\Lambda$  ,  $\bar{\Lambda}$  and  $K_s^0$  particles at the detector level in HERA-II.

## 5.5 Efficiency, Purity and Acceptance

The correction of the reconstructed particle at the hadron level was done by taking consideration of the detector acceptance,  $A$ . Acceptance indicates how good the detector understanding of the process is. The detector miscalculates the number of particles when the acceptance is low and the detector record a lot of fake signals if the acceptance is high. The acceptance is evaluated with MC studies and defined as the relative ratio of the reconstructed candidates in the detector level,  $\varepsilon$  to the total generated particles at the hadron level,  $P$ ,

$$\text{Acceptance, } A = \frac{\varepsilon}{P}$$

where  $\varepsilon$  is the efficiency and  $P$  is the purity.

The efficiency is the fraction of the generated particles at the hadron level appearing in the reconstructed signal at the detector level. The efficiency is defined as

$$\text{Efficiency, } \varepsilon = \frac{N_{real}^{detector}}{N_{mc}^{hadron}}$$

where  $N_{real}^{detector}$  define the number of real particles of interest at the detector level and  $N_{mc}^{hadron}$  define the number of generated particles at the hadron level. The fraction of the hadron level measured by the detector becomes greater when the efficiency is high.

The purity is the fraction of the real particles among the total reconstructed particle candidates. The purity is defined as

$$\text{Purity, } P = \frac{N_{real}^{detector}}{N_{candidates}^{detector}}$$

where  $N_{candidates}^{detector}$  is the number of reconstructed candidates at the detector level. The impurity of the sample from events transferring from other bins is small when the purities is high.

The ARIADNE Monte Carlo sample was used to calculate the acceptance, efficiency and purity. Table 5.2 shows the  $\Lambda$ ,  $\bar{\Lambda}$ ,  $\Lambda + \bar{\Lambda}$  and  $K_s^0$  reconstruction acceptances for high  $Q^2$  DIS and low  $Q^2$  DIS events

<b>Kinematics regions</b>	$\Lambda + \bar{\Lambda}$ (%)	$\Lambda$ (%)	$\bar{\Lambda}$ (%)	$K_s^0$ (%)
High $Q^2$	17.5	8.8	13.1	13.9
Low $Q^2$	15.3	7.6	11.7	10.5

**Table 5.3:** The  $\Lambda$ ,  $\bar{\Lambda}$ ,  $\Lambda + \bar{\Lambda}$  and  $K_s^0$  reconstruction acceptances for high  $Q^2$  DIS and low  $Q^2$  DIS events.

# CHAPTER 6

## Results, Correlation and Discussion

The strangeness total cross section, the differential production cross-sections, the baryon-antibaryon production asymmetry and the baryon to meson ratio for  $Q_{DA}^2 > 25 \text{ GeV}^2$  and  $5 < Q_{DA}^2 < 25 \text{ GeV}^2$  have been measured using HERA-II data with the ZEUS detector at the HERA collider. The 2003 & 2007 running period data are used with an integrated luminosity of  $4.6 \text{ pb}^{-1}$  and compared with ARIADNE Monte Carlo (MC) predictions. The results then compared with the results from the HERA-I data. The baryon antibaryon rapidity correlation in  $ep$  collisions was measured in order to investigate local conservation of quark flavor and baryon number in hadronization process.

### 6.1 Total Cross-Sections

The  $ep$  neutral-current DIS differential cross-sections  $d\sigma/dQ^2$ ,  $d\sigma/dp_T$  and  $d\sigma/d\eta$  for  $Q_{DA}^2 > 25 \text{ GeV}^2$  and  $5 < Q_{DA}^2 < 25 \text{ GeV}^2$  have been measured using HERA-II data with the ZEUS detector at HERA. The  $K_s^0$ ,  $\Lambda$  and  $\bar{\Lambda}$  cross sections were measured in the laboratory frame as functions of the kinematic variable  $Q^2$ , the pseudorapidity  $\eta$  and transverse momentum  $p_T$ . They are compared to the mentioned Monte Carlo predictions.

In high energy physics experiments, the measured cross section represents a measure of the probability of interaction between small particles and expressed in units of area, barn. A barn is defined as  $10^{-28} \text{ m}^2 (100 \text{ fm}^2)$ . The measured total cross sections provide a quantitative view of the probability of the neutral strange particle production in the considered kinematic regimes of  $ep$  collisions at HERA.

The kinematic region of  $Q_{DA}^2 > 25 \text{ GeV}^2$  and  $0.04 \leq y \leq 0.95$  were chosen for the measurement of the cross sections in the high- $Q^2$  Deep Inelastic Scattering sample and  $5 < Q_{DA}^2 < 25 \text{ GeV}^2$  and  $0.04 \leq y \leq 0.95$  for the low- $Q^2$  sample. In all three samples there was a further kinematic requirement that  $0.6 < p_T(\Lambda, \bar{\Lambda}, K_s^0) < 2.5 \text{ GeV}$  and  $|\eta(\Lambda, \bar{\Lambda}, K_s^0)| < 1.2$ . The measured cross section was the luminosity-weighted average of the cross sections at  $\sqrt{s} = 318 \text{ GeV}$  centre-of-mass energies.

The total cross-section ( $\sigma$ ) is given by

$$\sigma \approx \frac{N}{A.L.B}, \quad (6.1)$$

where  $N$  is the number of the reconstructed strange particles at the detector level,  $A$  is the acceptance,  $L$  is the integrated luminosity and  $B$  is the branching ratio. The acceptance  $A$  was evaluated with Monte Carlo studies. The branching ratios were taken as  $68.6 \pm 0.27\%$  for  $K_s^0 \rightarrow \pi^+ \pi^-$  and  $63.9 \pm 0.5\%$  for  $\Lambda \rightarrow p^+ \pi^-$  and  $\bar{\Lambda} \rightarrow \bar{p} \pi^+$  decay channels [20], respectively.

The total inclusive production cross-sections in the high  $Q^2$  kinematic range are found to be:

$$\sigma_{\Lambda} = 1,292 \pm 91(stat) pb^{-1},$$

$$\sigma_{\Lambda^-} = 868 \pm 64(stat) pb^{-1},$$

$$\sigma_{\Lambda+\Lambda^-} = 1,286 \pm 71(stat) pb^{-1},$$

$$\sigma_{K_s^0} = 4,966 \pm 120(stat) pb^{-1}$$

The total inclusive production cross-sections in the low  $Q^2$  kinematic range are found to be:

$$\sigma_{\Lambda} = 4,129 \pm 60(stat) pb^{-1},$$

$$\sigma_{\Lambda^-} = 2,733 \pm 106(stat) pb^{-1},$$

$$\sigma_{\Lambda+\Lambda^-} = 4,121 \pm 119(stat) pb^{-1},$$

$$\sigma_{K_s^0} = 17,372 \pm 275(stat) pb^{-1}$$



## 6.2 Differential Cross-Sections

The differential cross-sections in the Deep Inelastic Scattering samples were measured as functions of  $\eta(\Lambda, \bar{\Lambda}, K_s^0)$ ,  $p_T(\Lambda, \bar{\Lambda}, K_s^0)$  and  $Q^2$ . The  $\Lambda, \bar{\Lambda}$  and  $K_s^0$  differential cross sections in any variable  $Y$  were calculated using a standard bin-by-bin correction as follows [54]:

$$\frac{d\sigma}{dY} = \frac{dN}{A.L.B.\Delta Y}, \quad (6.2)$$

where  $dN$  is the number of the strange hadrons in a bin of size  $\Delta Y$ ,  $A$  is the acceptance evaluated with MC studies,  $L$  is the integrated luminosity and  $B$  is the branching ratio. In this thesis, the variable  $Y$  were the kinematic variable  $p_T$ ,  $\eta$  and  $Q^2$  for DIS events.

### 6.2.1 $5 < Q_{DA}^2 < 25 \text{ GeV}^2$

The differential production cross-sections of  $\Lambda$ ,  $\bar{\Lambda}$  and  $K_s^0$  with  $0.6 < p_T < 2.5 \text{ GeV}$  and  $|\eta| < 1.2$  have been measured for events within kinematic range  $5 < Q_{DA}^2 < 25 \text{ GeV}^2$ ,  $0.04 \leq y \leq 0.95$  as a function of  $Q^2$  of the event and  $p_T$  and  $\eta$  of the particle concerned.

The differential cross section measurements decrease when the value of the variables  $Q^2$  and  $p_T$  increase. The  $\eta$  cross section rises in the forward region for  $\Lambda$ ,  $\bar{\Lambda}$  and  $K_s^0$ .

### 6.2.1.1 Inclusive $\Lambda$ baryon cross-sections in bins of $Q^2$ , $p_T(\Lambda)$ and $\eta(\Lambda)$ .

The differential  $\Lambda$  baryon cross-sections as a function of  $Q^2$ ,  $p_T(\Lambda)$  and  $\eta(\Lambda)$  are shown in Figure 6.1 and listed in Table 6.1 for data and Table 6.2 for MC. The mass plots used in the calculation of these differential cross sections can be found in Section 5.3.

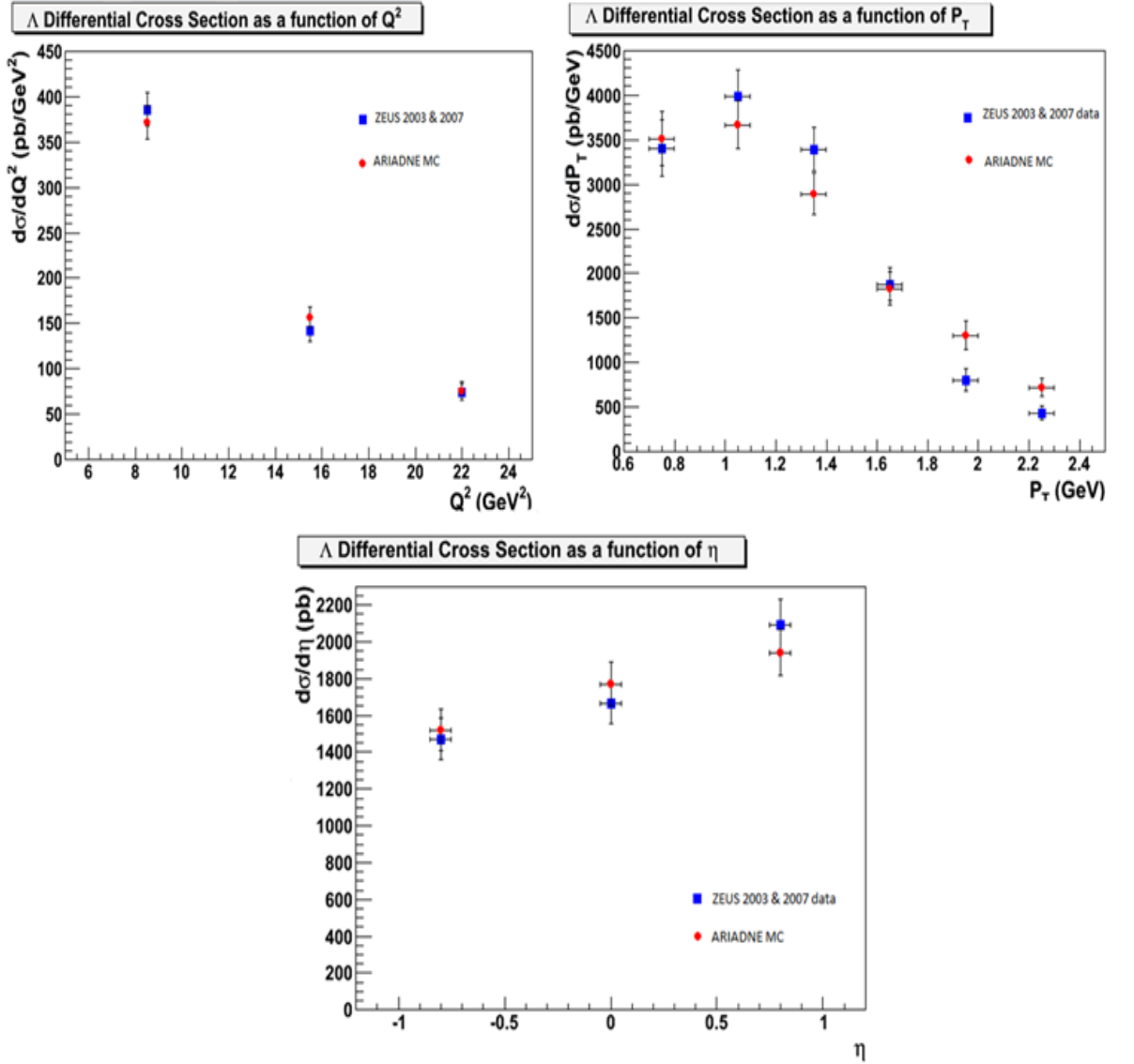


**Figure 6.1:** Differential cross-sections for  $\Lambda$  production in low  $Q^2$  DIS events with  $5 < Q_{DA}^2 < 25$  GeV $^2$  as a function of  $Q^2$ ,  $p_T(\Lambda)$  and  $\eta(\Lambda)$ . 2003 & 2007 HERA-II data and ARIADNE MC are shown.

$Q^2$ Range (GeV <sup>2</sup> )	$N(\Lambda)$	$d\sigma/dQ^2(\Lambda)$
5 – 12	602.92 $\pm$ 28.69	385.55 $\pm$ 18.34
12 – 19	222.92 $\pm$ 19.41	142.55 $\pm$ 12.41
19 – 25	99.90 $\pm$ 12.24	74.53 $\pm$ 9.13

$p_T$ Range (GeV)	$N(\Lambda)$	$d\sigma/dp_T(\Lambda)$ (pb/GeV)
0.6 – 0.9	228.08 $\pm$ 21.31	3,403.24 $\pm$ 317.97
0.9 – 1.2	267.06 $\pm$ 19.94	3,984.88 $\pm$ 297.53
1.2 – 1.5	227.38 $\pm$ 16.74	3,392.80 $\pm$ 249.78
1.5 – 1.8	125.53 $\pm$ 12.62	1,873.06 $\pm$ 188.30
1.8 – 2.1	53.91 $\pm$ 8.51	804.40 $\pm$ 126.97
2.1 – 2.5	39.02 $\pm$ 7.10	436.67 $\pm$ 79.45

$\eta$ Range	$N(\Lambda)$	$d\sigma/d\eta(\Lambda)$
(-1.2) – (-0.4)	262.72 $\pm$ 19.66	1,470.04 $\pm$ 110.00
(-0.4) – 0.4	297.62 $\pm$ 19.83	1,665.32 $\pm$ 110.95
0.4 – 1.2	373.68 $\pm$ 24.77	2,090.92 $\pm$ 138.60

**Table 6.1:** Differential  $\Lambda$  baryon cross-sections,  $d\sigma$ , measured as a function of  $Q^2$ ,  $p_T(\Lambda)$  and  $\eta(\Lambda)$  in data. The number of  $\Lambda$  baryons,  $N_\Lambda$  and the differential cross section  $d\sigma$  are listed for each range of  $Q^2$ ,  $p_T(\Lambda)$  and  $\eta(\Lambda)$ .

$Q^2$ Range (GeV <sup>2</sup> )	$N(\Lambda)$	$d\sigma/dQ^2(\Lambda)$
5 – 12	$2,426.20 \pm 58.69$	$1,595.56 \pm 38.59$
12 – 19	$1,022.25 \pm 36.58$	$672.27 \pm 24.05$
19 – 25	$424.62 \pm 26.61$	$325.78 \pm 20.41$

$p_T$ Range (GeV)	$N(\Lambda)$	$d\sigma/dp_T(\Lambda)$ (pb/GeV)
0.6 – 0.9	$987.17 \pm 41.22$	$15,148.07 \pm 632.51$
0.9 – 1.2	$1,030.07 \pm 36.42$	$15,806.36 \pm 558.86$
1.2 – 1.5	$812.14 \pm 31.55$	$12,462.24 \pm 484.13$
1.5 – 1.8	$512.93 \pm 24.89$	$7,870.88 \pm 381.93$
1.8 – 2.1	$366.46 \pm 20.95$	$5,623.30 \pm 321.47$
2.1 – 2.5	$270.66 \pm 18.38$	$3,114.94 \pm 211.52$

$\eta$ Range	$N(\Lambda)$	$d\sigma/d\eta(\Lambda)$
(-1.2) – (-0.4)	$1,127.07 \pm 38.60$	$6,485.56 \pm 222.11$
(-0.4) – 0.4	$1,310.67 \pm 42.35$	$7,542.06 \pm 243.69$
0.4 – 1.2	$1,434.28 \pm 44.39$	$8,253.35 \pm 255.43$

**Table 6.2:** Differential  $\Lambda$  baryon cross-sections,  $d\sigma$ , measured as a function of  $Q^2$ ,  $p_T(\Lambda)$  and  $\eta(\Lambda)$  in MC. The number of  $\Lambda$  baryons,  $N_\Lambda$  and the differential cross section  $d\sigma$  are listed for each range of  $Q^2$ ,  $p_T(\Lambda)$  and  $\eta(\Lambda)$ .

### 6.2.1.2 Inclusive $\bar{\Lambda}$ baryon cross-sections in bins of $Q^2$ , $p_T(\bar{\Lambda})$ and $\eta(\bar{\Lambda})$ .

The differential  $\bar{\Lambda}$  baryon cross-sections as a function of  $Q^2$ ,  $p_T(\bar{\Lambda})$  and  $\eta(\bar{\Lambda})$  are shown in Figure 6.2 and listed in Table 6.3 for data and Table 6.4 for MC. The mass plots used in the calculation of these differential cross sections can be found in Section 5.3.

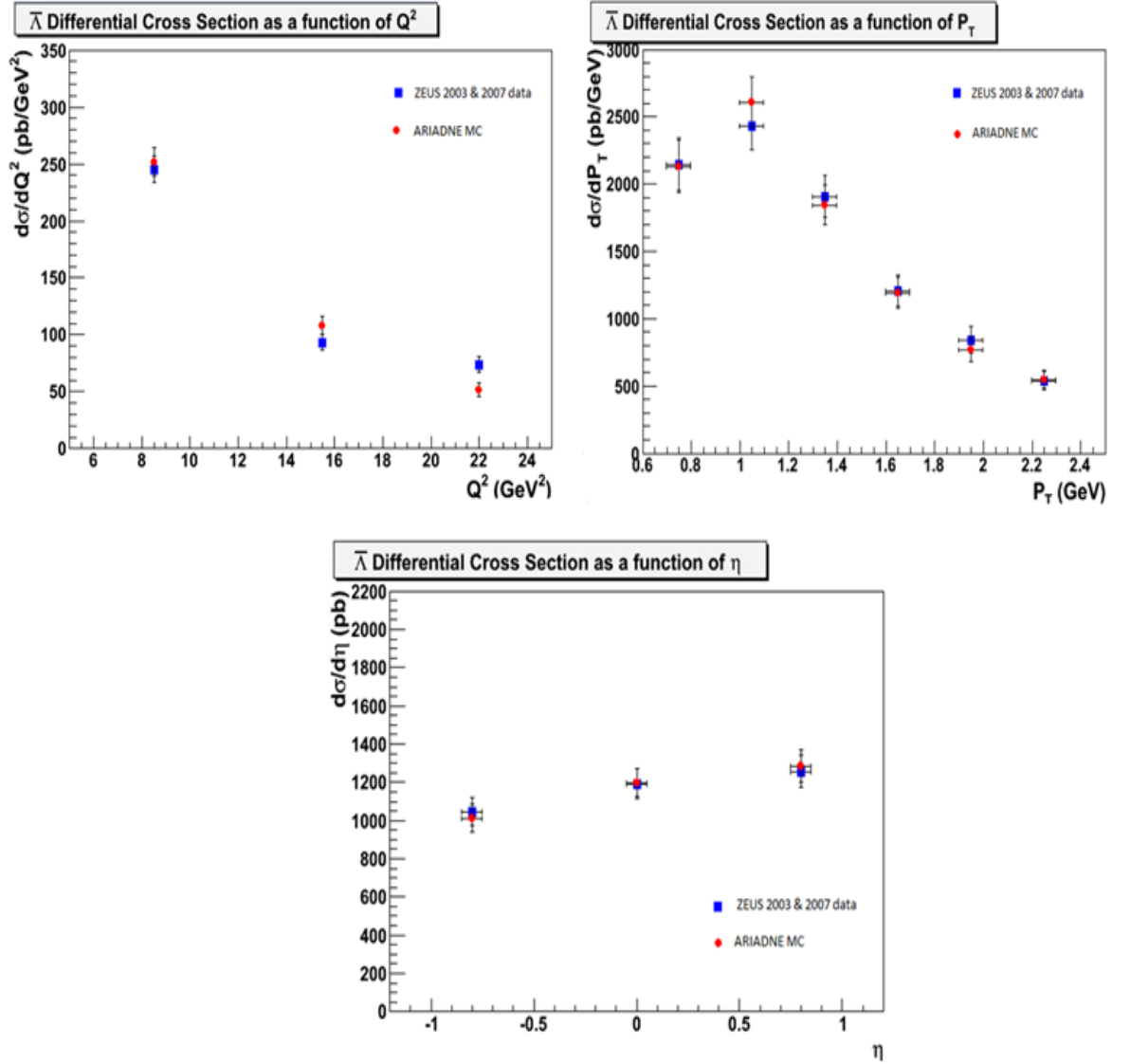


**Figure 6.2:** Differential cross-sections for  $\bar{\Lambda}$  production in low  $Q^2$  DIS events with  $5 < Q_{DA}^2 < 25$  GeV<sup>2</sup> as a function of  $Q^2$ ,  $p_T(\bar{\Lambda})$  and  $\eta(\bar{\Lambda})$ . 2003 & 2007 HERA-II data and ARIADNE MC are shown.

$Q^2$ Range (GeV <sup>2</sup> )	$N(\bar{\Lambda})$	$d\sigma/dQ^2(\bar{\Lambda})$
5 – 12	$588.71 \pm 28.73$	$244.54 \pm 11.93$
12 – 19	$224.06 \pm 17.73$	$93.07 \pm 7.36$
19 – 25	$151.83 \pm 14.06$	$73.58 \pm 6.81$

$p_T$ Range (GeV)	$N(\bar{\Lambda})$	$d\sigma/dp_T(\bar{\Lambda})$ (pb/GeV)
0.6 – 0.9	$221.12 \pm 19.87$	$2,143.19 \pm 192.58$
0.9 – 1.2	$250.71 \pm 18.40$	$2,429.99 \pm 178.34$
1.2 – 1.5	$196.96 \pm 15.72$	$1,909.02 \pm 152.36$
1.5 – 1.8	$124.23 \pm 12.23$	$1,204.09 \pm 118.53$
1.8 – 2.1	$86.46 \pm 10.28$	$838.01 \pm 99.63$
2.1 – 2.5	$73.41 \pm 9.46$	$533.64 \pm 68.76$

$\eta$ Range	$N(\bar{\Lambda})$	$d\sigma/d\eta(\bar{\Lambda})$
(-1.2) – (-0.4)	$287.90 \pm 19.95$	$1,046.42 \pm 72.51$
(-0.4) – 0.4	$327.19 \pm 20.94$	$1,189.22 \pm 76.10$
0.4 – 1.2	$344.93 \pm 22.50$	$1,253.70 \pm 81.77$

**Table 6.3:** Differential  $\bar{\Lambda}$  baryon cross-sections,  $d\sigma$ , measured as a function of  $Q^2$ ,  $p_T(\bar{\Lambda})$  and  $\eta(\bar{\Lambda})$  in data. The number of  $\bar{\Lambda}$  baryons,  $N_{\bar{\Lambda}}$  and the differential cross section  $d\sigma$  are listed for each range of  $Q^2$ ,  $p_T(\bar{\Lambda})$  and  $\eta(\bar{\Lambda})$ .

$Q^2$ Range (GeV <sup>2</sup> )	$N(\bar{\Lambda})$	$d\sigma/dQ^2(\bar{\Lambda})$
5 – 12	$2,313.73 \pm 57.94$	$988.39 \pm 24.75$
12 – 19	$993.59 \pm 36.44$	$424.44 \pm 15.56$
19 – 25	$405.20 \pm 24.53$	$201.94 \pm 12.22$

$p_T$ Range (GeV)	$N(\bar{\Lambda})$	$d\sigma/dp_T(\bar{\Lambda})$ (pb/GeV)
0.6 – 0.9	$853.32 \pm 39.95$	$8,505.60 \pm 398.20$
0.9 – 1.2	$1,047.63 \pm 38.07$	$10,442.41 \pm 379.46$
1.2 – 1.5	$739.83 \pm 30.33$	$7,374.37 \pm 302.31$
1.5 – 1.8	$478.76 \pm 24.22$	$4,772.11 \pm 241.41$
1.8 – 2.1	$307.51 \pm 19.66$	$3,065.15 \pm 195.96$
2.1 – 2.5	$290.07 \pm 19.58$	$2,168.48 \pm 146.37$

$\eta$ Range	$N(\bar{\Lambda})$	$d\sigma/d\eta(\bar{\Lambda})$
(-1.2) – (-0.4)	$1,073.89 \pm 39.30$	$4,014.06 \pm 146.89$
(-0.4) – 0.4	$1,270.47 \pm 40.83$	$4,748.85 \pm 152.61$
0.4 – 1.2	$1,363.67 \pm 45.76$	$5,097.22 \pm 171.04$

**Table 6.4:** Differential  $\bar{\Lambda}$  baryon cross-sections,  $d\sigma$ , measured as a function of  $Q^2$ ,  $p_T(\bar{\Lambda})$  and  $\eta(\bar{\Lambda})$  in MC. The number of  $\bar{\Lambda}$  baryons,  $N_{\bar{\Lambda}}$  and the differential cross section  $d\sigma$  are listed for each range of  $Q^2$ ,  $p_T(\bar{\Lambda})$  and  $\eta(\bar{\Lambda})$ .

### 6.2.1.3 Inclusive $\Lambda + \bar{\Lambda}$ baryon cross-sections in bins of $Q^2$ , $p_T(\Lambda + \bar{\Lambda})$ and $\eta(\Lambda + \bar{\Lambda})$ .

The differential  $\Lambda + \bar{\Lambda}$  baryon cross-sections as a function of  $Q^2$ ,  $p_T(\Lambda + \bar{\Lambda})$  and  $\eta(\Lambda + \bar{\Lambda})$  are shown in Figure 6.3 and listed in Table 6.5 for data and Table 6.6 for MC. The mass plots used in the calculation of these differential cross sections can be found in Section 5.3.

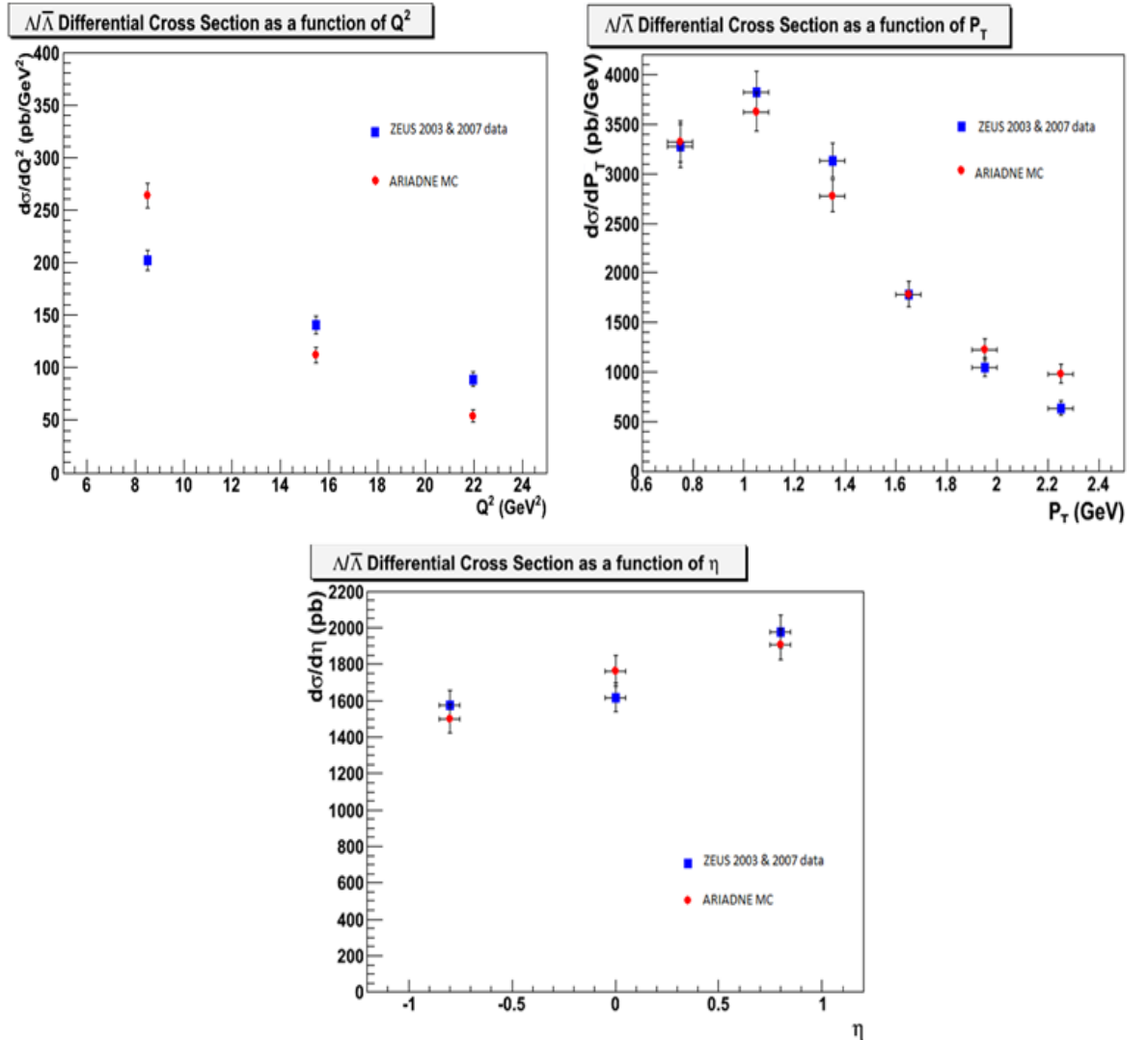


**Figure 6.3:** Differential cross-sections for  $\Lambda + \bar{\Lambda}$  production in low  $Q^2$  DIS events with  $5 < Q^2 < 25$  GeV<sup>2</sup> as a function of  $Q^2$ ,  $p_T(\Lambda + \bar{\Lambda})$  and  $\eta(\Lambda + \bar{\Lambda})$ . 2003 & 2007 HERA-II data and ARIADNE MC are shown.



$Q^2$ Range (GeV <sup>2</sup> )	$N(\Lambda + \bar{\Lambda})$	$d\sigma/dQ^2(\Lambda + \bar{\Lambda})$
5 – 12	633.13 ± 31.46	201.11 ± 9.99
12 – 19	439.67 ± 26.53	139.90 ± 8.42
19 – 25	237.21 ± 18.65	87.90 ± 6.91

$p_T$ Range (GeV)	$N(\Lambda + \bar{\Lambda})$	$d\sigma/dp_T(\Lambda + \bar{\Lambda})$ (pb/GeV)
0.6 – 0.9	441.72 ± 29.95	3,273.97 ± 221.98
0.9 – 1.2	515.04 ± 27.72	3,817.41 ± 205.45
1.2 – 1.5	422.11 ± 23.03	3,128.63 ± 170.69
1.5 – 1.8	241.17 ± 17.64	1,787.52 ± 130.74
1.8 – 2.1	141.50 ± 13.21	1,048.78 ± 97.91
2.1 – 2.5	114.50 ± 12.23	636.49 ± 67.98

$\eta$ Range	$N(\Lambda + \bar{\Lambda})$	$d\sigma/d\eta(\Lambda + \bar{\Lambda})$
(-1.2) – (-0.4)	566.87 ± 27.94	1,575.59 ± 77.65
(-0.4) – 0.4	581.64 ± 28.69	1,616.64 ± 79.74
0.4 – 1.2	710.40 ± 32.38	1,974.52 ± 89.99

**Table 6.5:** Differential  $\Lambda + \bar{\Lambda}$  baryon cross-sections,  $d\sigma$ , measured as a function of  $Q^2$ ,  $p_T(\Lambda + \bar{\Lambda})$  and  $\eta(\Lambda + \bar{\Lambda})$  in data. The number of  $\Lambda + \bar{\Lambda}$  baryons,  $N_{\Lambda + \bar{\Lambda}}$  and the differential cross section  $d\sigma$  are listed for each range of  $Q^2$ ,  $p_T(\Lambda + \bar{\Lambda})$  and  $\eta(\Lambda + \bar{\Lambda})$ .

$Q^2$ Range (GeV <sup>2</sup> )	$N(\Lambda + \bar{\Lambda})$	$d\sigma/dQ^2(\Lambda + \bar{\Lambda})$
5 – 12	4,739.31 $\pm$ 82.33	1,548.19 $\pm$ 26.89
12 – 19	2,008.21 $\pm$ 53.35	656.02 $\pm$ 17.42
19 – 25	828.50 $\pm$ 36.34	315.75 $\pm$ 13.84

$p_T$ Range (GeV)	$N(\Lambda + \bar{\Lambda})$	$d\sigma/dp_T(\Lambda + \bar{\Lambda})$ (pb/GeV)
0.6 – 0.9	1,837.59 $\pm$ 57.38	14,006.71 $\pm$ 437.36
0.9 – 1.2	2,004.55 $\pm$ 52.70	15,279.33 $\pm$ 401.69
1.2 – 1.5	1,533.92 $\pm$ 43.66	11,692.03 $\pm$ 332.79
1.5 – 1.8	987.85 $\pm$ 34.70	7,529.71 $\pm$ 264.49
1.8 – 2.1	682.52 $\pm$ 29.06	5,202.39 $\pm$ 221.50
2.1 – 2.5	542.49 $\pm$ 26.16	4,135.03 $\pm$ 199.39

$\eta$ Range	$N(\Lambda + \bar{\Lambda})$	$d\sigma/d\eta(\Lambda + \bar{\Lambda})$
(-1.2) – (-0.4)	2,199.71 $\pm$ 56.38	6,287.59 $\pm$ 161.15
(-0.4) – 0.4	2,578.27 $\pm$ 59.81	7,369.65 $\pm$ 170.95
0.4 – 1.2	2,797.27 $\pm$ 62.29	7,995.63 $\pm$ 178.04

**Table 6.6:** Differential  $\Lambda + \bar{\Lambda}$  baryon cross-sections,  $d\sigma$ , measured as a function of  $Q^2$ ,  $p_T(\Lambda + \bar{\Lambda})$  and  $\eta(\Lambda + \bar{\Lambda})$  in MC. The number of  $\Lambda + \bar{\Lambda}$  baryons,  $N_{\Lambda + \bar{\Lambda}}$  and the differential cross section  $d\sigma$  are listed for each range of  $Q^2$ ,  $p_T(\Lambda + \bar{\Lambda})$  and  $\eta(\Lambda + \bar{\Lambda})$ .

#### 6.2.1.4 Inclusive $K_s^0$ meson cross-sections in bins of $Q^2$ , $p_T(K_s^0)$ and $\eta(K_s^0)$ .

The differential  $K_s^0$  meson cross-sections as a function of  $Q^2$ ,  $p_T(K_s^0)$  and  $\eta(K_s^0)$  are shown in Figure 6.4 and listed in Table 6.7 for data and Table 6.8 for MC. The mass plots used in the calculation of these differential cross sections can be found in Section 5.4.

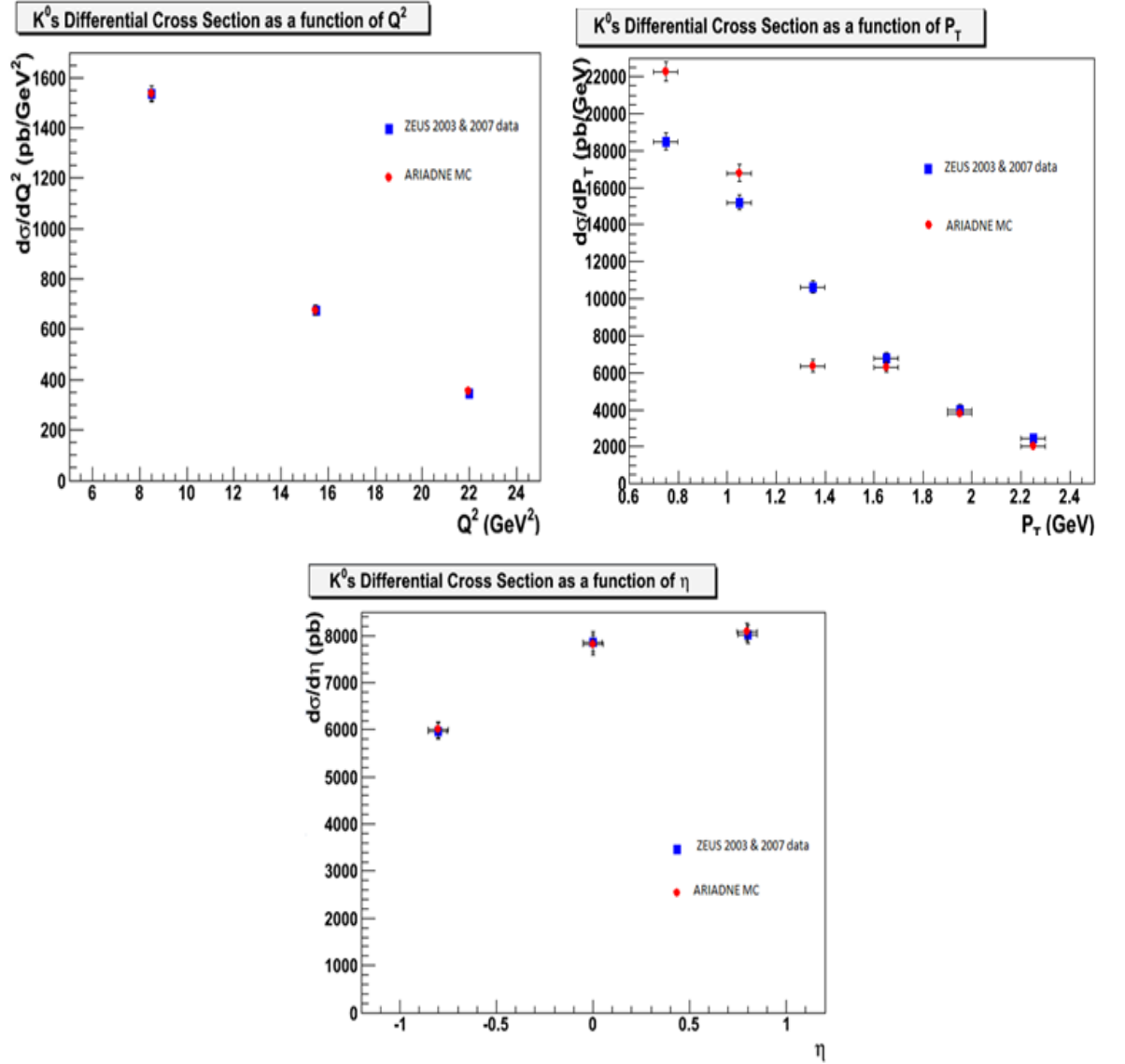


**Figure 6.4:** Differential cross-sections for  $K_s^0$  production in low  $Q^2$  DIS events with  $5 < Q_{DA}^2 < 25$  GeV<sup>2</sup> as a function of  $Q^2$ ,  $p_T(K_s^0)$  and  $\eta(K_s^0)$ . 2003 & 2007 HERA-II data and ARIADNE MC are shown.

$Q^2$ Range (GeV <sup>2</sup> )	$N(K_s^0)$	$d\sigma/dQ^2(K_s^0)$
5 – 12	3,577.76 ± 71.99	1,535.84 ± 30.90
12 – 19	1,568.49 ± 43.42	673.31 ± 18.63
19 – 25	689.37 ± 28.37	345.25 ± 14.20

$p_T$ Range (GeV)	$N(K_s^0)$	$d\sigma/dp_T(K_s^0)$ (pb/GeV)
0.6 – 0.9	1,845.89 ± 47.99	18,489.20 ± 480.68
0.9 – 1.2	1,513.88 ± 42.41	15,163.65 ± 424.79
1.2 – 1.5	1,060.41 ± 36.00	10,621.50 ± 360.59
1.5 – 1.8	675.96 ± 27.97	6,770.69 ± 280.15
1.8 – 2.1	394.90 ± 26.23	3,995.48 ± 262.73
2.1 – 2.5	324.61 ± 20.21	2,438.57 ± 151.82

$\eta$ Range	$N(K_s^0)$	$d\sigma/d\eta(K_s^0)$
(-1.2) – (-0.4)	1,588.66 ± 43.92	5,967.25 ± 164.97
(-0.4) – 0.4	2,094.54 ± 57.41	7,867.41 ± 215.64
0.4 – 0.4	2,135.15 ± 49.86	8,019.95 ± 187.28

**Table 6.7:** Differential  $K_s^0$  meson cross-sections,  $d\sigma$ , measured as a function of  $Q^2$ ,  $p_T(K_s^0)$  and  $\eta(K_s^0)$  in data. The number of  $K_s^0$  meson,  $N_{K_s^0}$  and the differential cross section  $d\sigma$  are listed for each range of  $Q^2$ ,  $p_T(K_s^0)$  and  $\eta(K_s^0)$ .

$Q^2$ Range (GeV <sup>2</sup> )	$N(K_s^0)$	$d\sigma/dQ^2(K_s^0)$
5 – 12	15,449.65 ± 133.71	6,820.45 ± 59.02
12 – 19	6,773.06 ± 95.41	2,990.05 ± 42.11
19 – 25	3,060.66 ± 59.97	1,576.36 ± 30.88

$p_T$ Range (GeV)	$N(K_s^0)$	$d\sigma/dp_T(K_s^0)$ (pb/GeV)
0.6 – 0.9	9,015.91 ± 107.51	92,871.16 ± 1,107.43
0.9 – 1.2	6,788.17 ± 88.39	69,923.64 ± 910.48
1.2 – 1.5	2,539.68 ± 70.47	26,160.75 ± 725.89
1.5 – 1.8	2,585.03 ± 59.32	26,627.89 ± 611.04
1.8 – 2.1	1,526.96 ± 43.25	15,728.92 ± 445.50
2.1 – 2.5	1,112.68 ± 37.75	8,596.12 ± 291.64

$\eta$ Range	$N(K_s^0)$	$d\sigma/d\eta(K_s^0)$
(-1.2) – (-0.4)	6,929.95 ± 90.70	26,769.03 ± 350.35
(-0.4) – 0.4	9,020.08 ± 113.20	34,842.79 ± 437.26
0.4 – 1.2	9,334.76 ± 102.29	36,058.34 ± 395.12

**Table 6.8:** Differential  $K_s^0$  meson cross-sections,  $d\sigma$ , measured as a function of  $Q^2$ ,  $p_T(K_s^0)$  and  $\eta(K_s^0)$  in MC. The number of  $K_s^0$  meson,  $N_{K_s^0}$  and the differential cross section  $d\sigma$  are listed for each range of  $Q^2$ ,  $p_T(K_s^0)$  and  $\eta(K_s^0)$ .

### 6.2.2 $Q_{DA}^2 > 25 \text{ GeV}^2$

The differential production cross-sections of  $\Lambda$ ,  $\bar{\Lambda}$  and  $K_s^0$  with  $0.6 < p_T < 2.5 \text{ GeV}$  and  $|\eta| < 1.2$  have been measured for events within kinematic range  $Q_{DA}^2 > 25 \text{ GeV}^2$ ,  $0.04 \leq y \leq 0.95$  as a function of  $Q^2$  of the event and  $p_T$  and  $\eta$  of the particle concerned.

The differential cross section measurements decrease when the value of the variables  $Q^2$  and  $p_T$  increase. The  $\eta$  cross section rises in the forward region for  $\Lambda$ ,  $\bar{\Lambda}$  and  $K_s^0$ .

### 6.2.2.1 Inclusive $\Lambda$ baryon cross-sections in bins of $Q^2$ , $p_T(\Lambda)$ and $\eta(\Lambda)$ .

The differential  $\Lambda$  baryon cross-sections as a function of  $Q^2$ ,  $p_T(\Lambda)$  and  $\eta(\Lambda)$  are shown in Figure 6.5 and listed in Table 6.9 for data and Table 6.10 for MC. The mass plots used in the calculation of these differential cross sections can be found in Section 5.3.

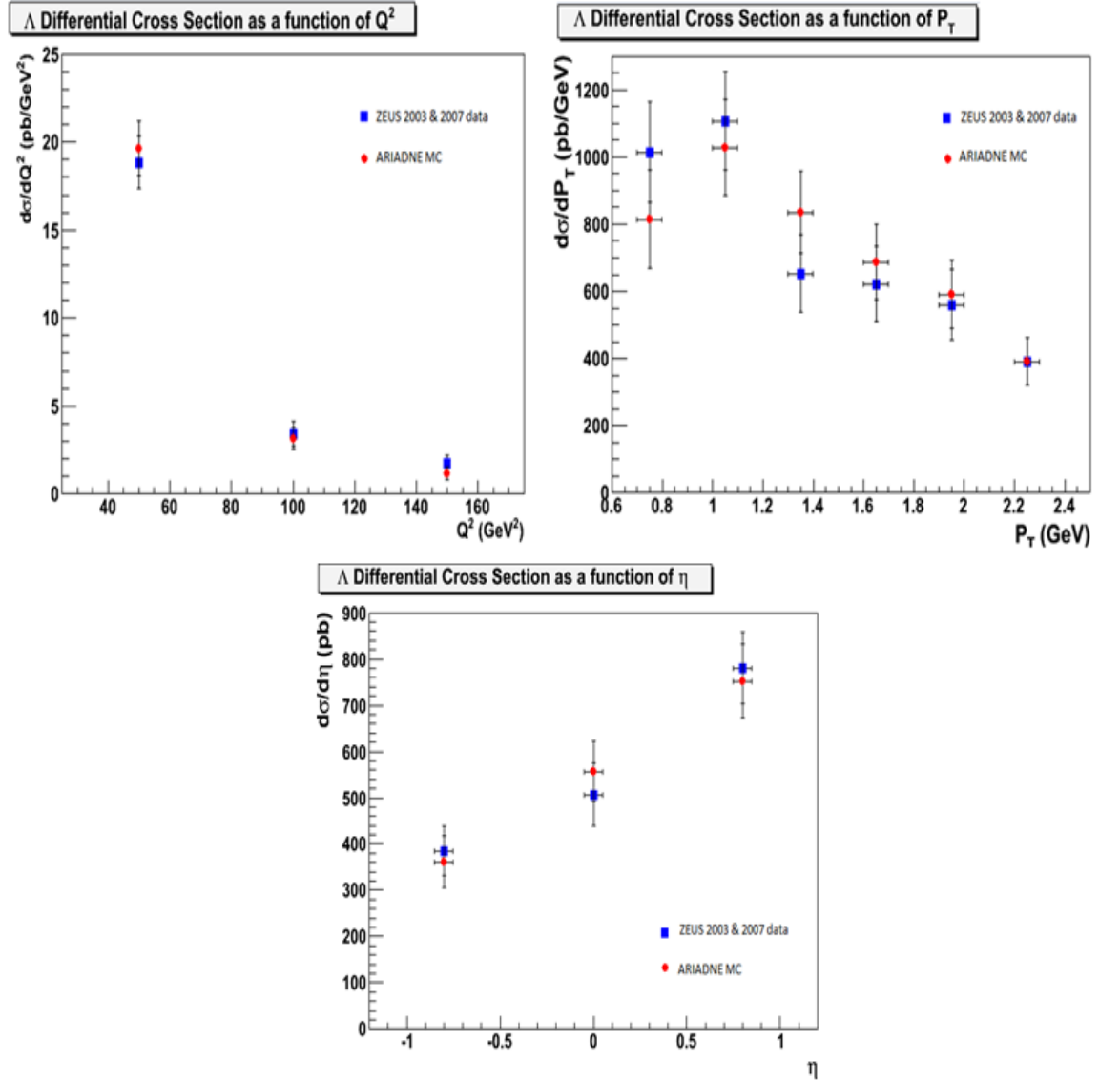


**Figure 6.5:** Differential cross-sections for  $\Lambda$  production in high- $Q^2$  DIS events with  $Q_{DA}^A > 25 \text{ GeV}^2$  as a function of  $Q^2$ ,  $p_T(\Lambda)$  and  $\eta(\Lambda)$ . 2003 & 2007 HERA-II data and ARIADNE MC are shown.

$Q^2$ Range (GeV <sup>2</sup> )	$N(\Lambda)$	$d\sigma/dQ^2(\Lambda)$
25 – 75	$243.31 \pm 19.37$	$18.81 \pm 1.49$
75 – 125	$44.20 \pm 8.75$	$3.41 \pm 0.67$
125 - 175	$23.00 \pm 5.71$	$1.77 \pm 0.43$

$p_T$ Range (GeV)	$N(\Lambda)$	$d\sigma/dp_T(\Lambda)$ (pb/GeV)
0.6 – 0.9	$78.57 \pm 11.66$	$1,012.49 \pm 150.25$
0.9 – 1.2	$85.92 \pm 11.38$	$1,107.21 \pm 146.64$
1.2 – 1.5	$50.58 \pm 8.83$	$651.80 \pm 113.78$
1.5 – 1.8	$48.10 \pm 8.74$	$619.84 \pm 112.62$
1.8 – 2.1	$43.45 \pm 8.02$	$559.92 \pm 103.35$
2.1 – 2.5	$40.39 \pm 7.20$	$390.36 \pm 69.58$

$\eta$ Range	$N(\Lambda)$	$d\sigma/d\eta(\Lambda)$
(-1.2) – (-0.4)	$79.57 \pm 11.23$	$384.51 \pm 54.26$
(-0.4) – 0.4	$104.53 \pm 14.13$	$505.13 \pm 68.28$
0.4 – 1.2	$161.22 \pm 16.11$	$779.08 \pm 77.85$

**Table 6.9:** Differential  $\Lambda$  baryon cross section,  $d\sigma$ , measured as a function of  $Q^2$ ,  $p_T(\Lambda)$  and  $\eta(\Lambda)$  in data. The number of  $\Lambda$  baryons,  $N_\Lambda$  and the differential cross section  $d\sigma$  are listed for each range of  $Q^2$ ,  $p_T(\Lambda)$  and  $\eta(\Lambda)$ .



$Q^2$ Range (GeV <sup>2</sup> )	$N(\Lambda)$	$d\sigma/dQ^2(\Lambda)$
25 – 75	1,030.26 $\pm$ 38.83	81.92 $\pm$ 3.08
75 – 125	165.90 $\pm$ 16.27	13.19 $\pm$ 1.29
125 - 175	61.61 $\pm$ 9.61	4.89 $\pm$ 0.76

$p_T$ Range (GeV)	$N(\Lambda)$	$d\sigma/dp_T(\Lambda)$ (pb/GeV)
0.6 – 0.9	249.95 $\pm$ 22.92	3,312.45 $\pm$ 303.74
0.9 – 1.2	314.54 $\pm$ 22.17	4,168.42 $\pm$ 293.80
1.2 – 1.5	256.05 $\pm$ 18.94	3,393.29 $\pm$ 251.00
1.5 – 1.8	210.66 $\pm$ 17.36	2,791.76 $\pm$ 230.06
1.8 – 2.1	180.85 $\pm$ 15.83	2,396.70 $\pm$ 209.78
2.1 – 2.5	159.12 $\pm$ 14.68	1,581.54 $\pm$ 145.90

$\eta$ Range	$N(\Lambda)$	$d\sigma/d\eta(\Lambda)$
(-1.2) – (-0.4)	295.02 $\pm$ 21.33	1,466.15 $\pm$ 106.00
(0.4) – 0.4	453.30 $\pm$ 25.76	2,252.75 $\pm$ 128.01
0.4 – 1.2	612.48 30.86	3,043.82 153.36

**Table 6.10:** Differential  $\Lambda$  baryon cross section,  $d\sigma$ , measured as a function of  $Q^2$ ,  $p_T(\Lambda)$  and  $\eta(\Lambda)$  in MC. The number of  $\Lambda$  baryons,  $N_\Lambda$  and the differential cross section  $d\sigma$  are listed for each range of  $Q^2$ ,  $p_T(\Lambda)$  and  $\eta(\Lambda)$ .

### 6.2.2.2 Inclusive $\bar{\Lambda}$ baryon cross-sections in bins of $Q^2$ , $p_T(\bar{\Lambda})$ and $\eta(\bar{\Lambda})$ .

The differential  $\bar{\Lambda}$  baryon cross-sections as a function of  $Q^2$ ,  $p_T(\bar{\Lambda})$  and  $\eta(\bar{\Lambda})$  are shown in Figure 6.6 and listed in Table 6.11 for data and Table 6.12 for MC. The mass plots used in the calculation of these differential cross sections can be found in Section 5.3.

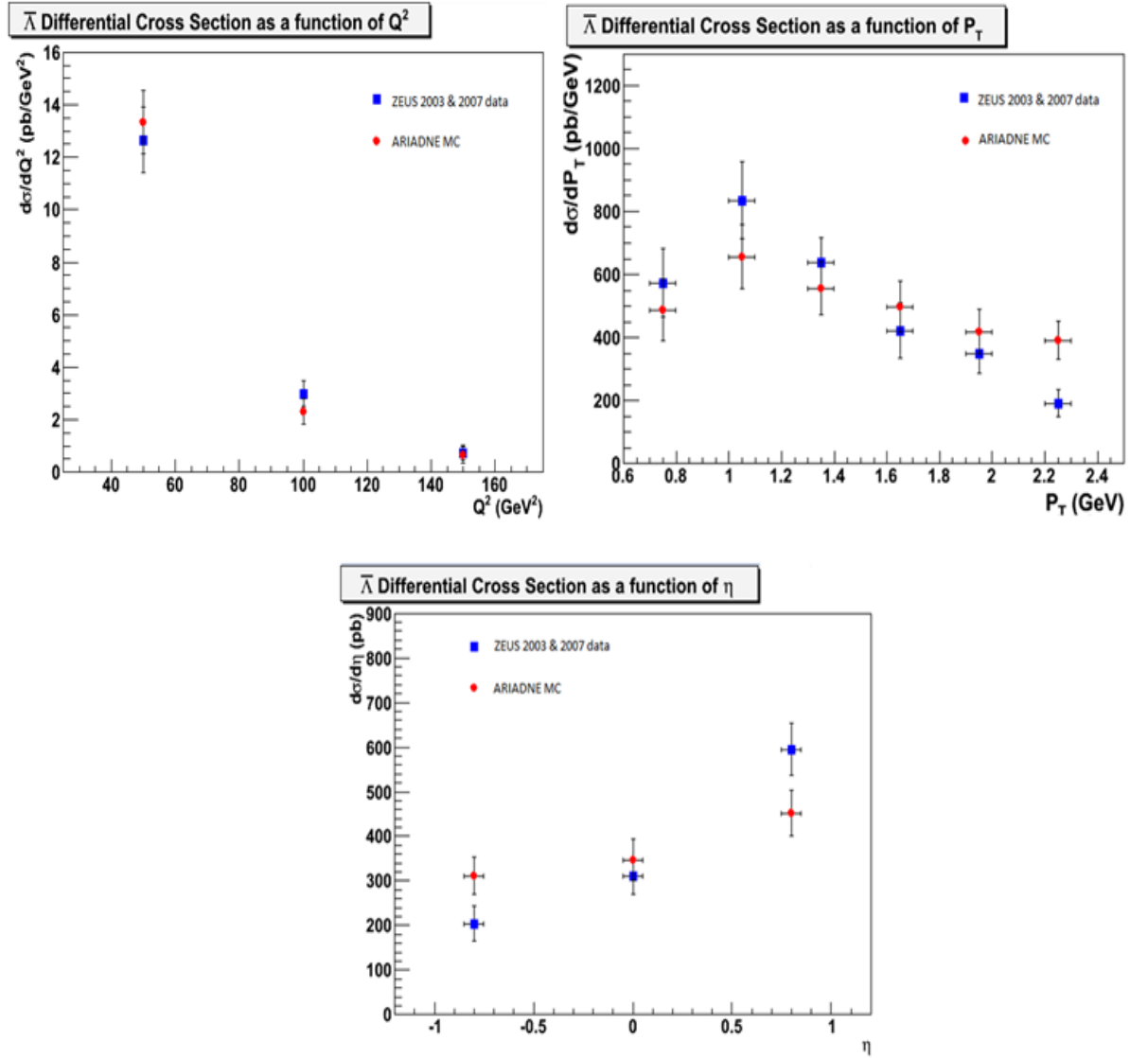


**Figure 6.6:** Differential cross-sections for  $\bar{\Lambda}$  production in high  $Q^2$  DIS events with  $Q_{DA}^2 > 25$  GeV<sup>2</sup>

as a function of  $Q^2$ ,  $p_T(\bar{\Lambda})$  and  $\eta(\bar{\Lambda})$ . 2003 & 2007 HERA-II data and ARIADNE MC are shown.

$Q^2$ Range (GeV <sup>2</sup> )	$N(\bar{\Lambda})$	$d\sigma/dQ^2(\bar{\Lambda})$
25 – 75	$243.32 \pm 24.54$	$12.63 \pm 1.27$
75 – 125	$57.02 \pm 9.34$	$2.96 \pm 0.48$
125 – 75	$14.21 \pm 5.39$	$0.73 \pm 0.27$

$p_T$ Range (GeV)	$N(\bar{\Lambda})$	$d\sigma/dp_T(\bar{\Lambda})$ (pb/GeV)
0.6 – 0.9	$66.15 \pm 12.56$	$572.63 \pm 108.72$
0.9 – 1.2	$96.23 \pm 14.01$	$833.02 \pm 121.27$
1.2 – 1.5	$73.57 \pm 9.99$	$636.86 \pm 86.47$
1.5 – 1.8	$48.46 \pm 8.78$	$419.50 \pm 76.00$
1.8 – 2.1	$40.42 \pm 7.41$	$349.90 \pm 64.14$
2.1 – 2.5	$29.36 \pm 6.46$	$190.61 \pm 41.93$

$\eta$ Range	$N(\bar{\Lambda})$	$d\sigma/d\eta(\bar{\Lambda})$
(-1.2) – (-0.4)	$62.43 \pm 12.33$	$202.66 \pm 40.02$
(-0.4) – 0.4	$95.73 \pm 12.50$	$310.76 \pm 40.57$
0.4 – 1.2	$183.12 \pm 17.87$	$594.45 \pm 58.01$

**Table 6.11:** Differential  $\bar{\Lambda}$  baryon cross section,  $d\sigma$ , measured as a function of  $Q^2$ ,  $p_T(\bar{\Lambda})$  and  $\eta(\bar{\Lambda})$  in data. The number of  $\bar{\Lambda}$  baryons,  $N_{\bar{\Lambda}}$  and the differential cross section  $d\sigma$  are listed for each range of  $Q^2$ ,  $p_T(\bar{\Lambda})$  and  $\eta(\bar{\Lambda})$ .

$Q^2$ Range (GeV <sup>2</sup> )	$N(\bar{\Lambda})$	$d\sigma/dQ^2(\bar{\Lambda})$
25 – 75	$1,009.51 \pm 40.42$	$53.92 \pm 2.15$
75 – 125	$175.92 \pm 16.55$	$9.39 \pm 0.88$
125 – 175	$52.02 \pm 10.30$	$2.77 \pm 0.54$

$p_T$ Range (GeV)	$N(\bar{\Lambda})$	$d\sigma/dp_T(\bar{\Lambda})$ (pb/GeV)
0.6 – 0.9	$207.29 \pm 21.63$	$1,845.38 \pm 192.55$
0.9 – 1.2	$278.46 \pm 22.69$	$2,478.96 \pm 201.99$
1.2 – 1.5	$237.32 \pm 18.55$	$2,112.72 \pm 165.13$
1.5 – 1.8	$211.41 \pm 18.21$	$1,882.05 \pm 162.11$
1.8 – 2.1	$178.32 \pm 15.61$	$1,587.47 \pm 138.96$
2.1 – 2.5	$222.02 \pm 17.60$	$1,482.38 \pm 117.51$

$\eta$ Range	$N(\bar{\Lambda})$	$d\sigma/d\eta(\bar{\Lambda})$
(-1.2) – (-0.4)	$374.97 \pm 23.73$	$1,251.80 \pm 79.22$
(-0.4) – 0.4	$418.31 \pm 25.91$	$1,396.48 \pm 86.49$
0.4 – 1.2	$546.83 \pm 29.25$	$1,825.53 \pm 97.64$

**Table 6.12:** Differential  $\bar{\Lambda}$  baryon cross section,  $d\sigma$ , measured as a function of  $Q^2$ ,  $p_T(\bar{\Lambda})$  and  $\eta(\bar{\Lambda})$  in MC. The number of  $\bar{\Lambda}$  baryons,  $N_{\bar{\Lambda}}$  and the differential cross section  $d\sigma$  are listed for each range of  $Q^2$ ,  $p_T(\bar{\Lambda})$  and  $\eta(\bar{\Lambda})$ .

### 6.2.2.3 Inclusive $\Lambda + \bar{\Lambda}$ baryon cross-sections in bins of $Q^2$ , $p_T(\Lambda + \bar{\Lambda})$ and $\eta(\Lambda + \bar{\Lambda})$ .

The differential  $\Lambda + \bar{\Lambda}$  baryon cross-sections as a function of  $Q^2$ ,  $p_T(\Lambda + \bar{\Lambda})$  and  $\eta(\Lambda + \bar{\Lambda})$  are shown in Figure 6.7 and listed in Table 6.13 for data and Table 6.14 for MC. The mass plots used in the calculation of these differential cross sections can be found in Section 5.3.

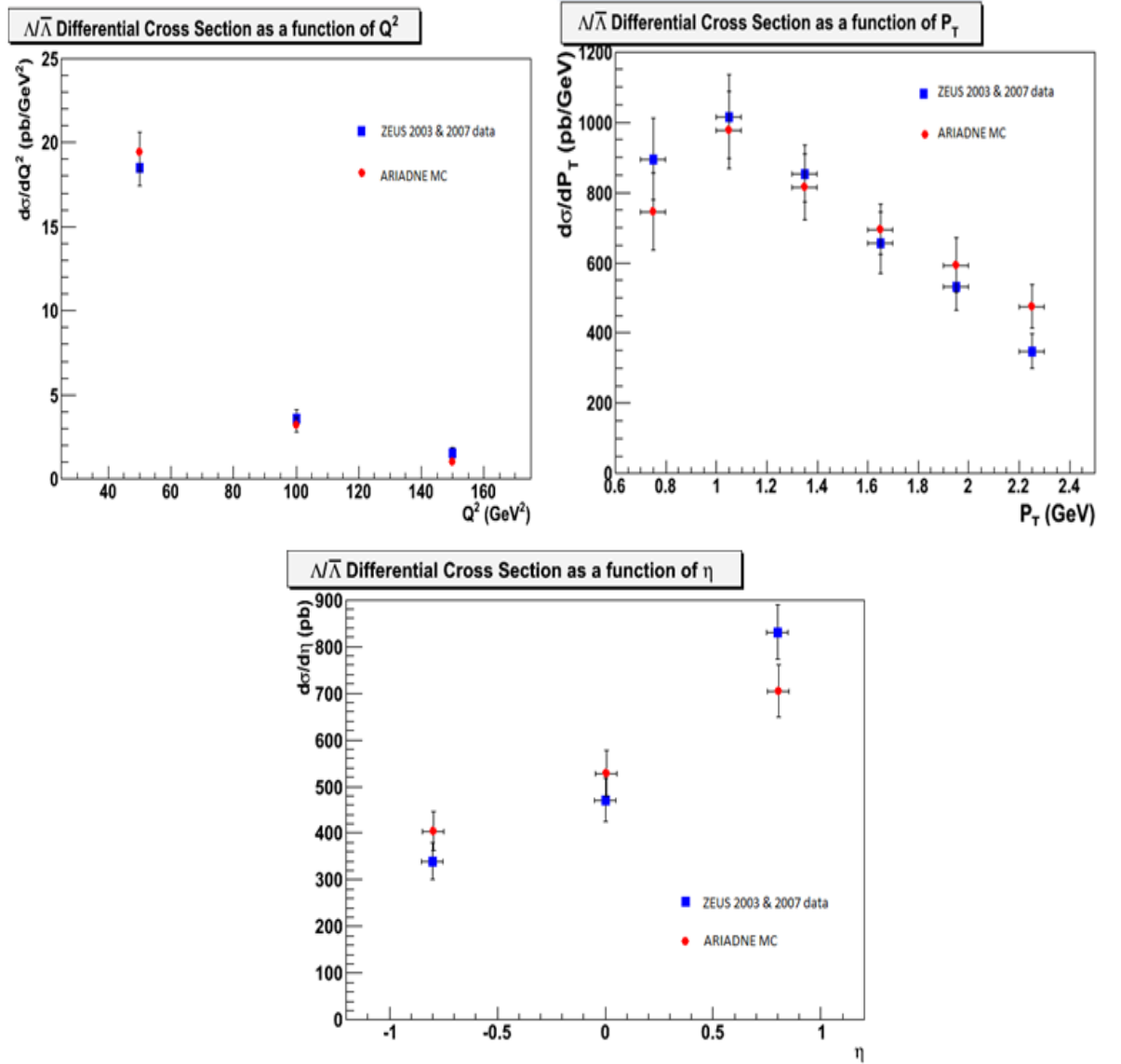


**Figure 6.7:** Differential cross-sections for  $\Lambda + \bar{\Lambda}$  production in high  $Q^2$  DIS events with  $Q_{DA}^2 > 25$  GeV<sup>2</sup> as a function of  $Q^2$ ,  $p_T(\Lambda + \bar{\Lambda})$  and  $\eta(\Lambda + \bar{\Lambda})$ . 2003 & 2007 HERA-II data and ARIADNE MC are shown.

$Q^2$ Range (GeV <sup>2</sup> )	$N(\Lambda + \bar{\Lambda})$	$d\sigma/dQ^2(\Lambda + \bar{\Lambda})$
25 – 75	$475.33 \pm 28.16$	$18.48 \pm 1.09$
75 – 125	$92.87 \pm 12.34$	$3.61 \pm 0.47$
125 – 175	$39.50 \pm 7.72$	$1.53 \pm 0.29$

$p_T$ Range (GeV)	$N(\Lambda + \bar{\Lambda})$	$d\sigma/dp_T(\Lambda + \bar{\Lambda})$ (pb/GeV)
0.6 – 0.9	$138.00 \pm 18.02$	$894.25 \pm 116.77$
0.9 – 1.2	$156.66 \pm 18.27$	$1,015.17 \pm 118.39$
1.2 – 1.5	$131.78 \pm 13.51$	$853.94 \pm 87.54$
1.5 – 1.8	$101.11 \pm 12.73$	$655.20 \pm 82.49$
1.8 – 2.1	$81.97 \pm 10.75$	$531.17 \pm 69.66$
2.1 – 2.5	$71.69 \pm 10.16$	$348.41 \pm 49.37$

$\eta$ Range	$N(\Lambda + \bar{\Lambda})$	$d\sigma/d\eta(\Lambda + \bar{\Lambda})$
(-1.2) – (-0.4)	$140.00 \pm 16.49$	$340.20 \pm 40.07$
(-0.4) – 0.4	$193.36 \pm 19.52$	$469.87 \pm 47.43$
0.4 – 1.2	$341.28 \pm 24.18$	$829.32 \pm 58.75$

**Table 6.13:** Differential  $\Lambda + \bar{\Lambda}$  baryon cross section,  $d\sigma$ , measured as a function of  $Q^2$ ,  $p_T(\Lambda + \bar{\Lambda})$  and  $\eta(\Lambda + \bar{\Lambda})$  in data. The number of  $\Lambda + \bar{\Lambda}$  baryons,  $N_{\Lambda + \bar{\Lambda}}$  and the differential cross section  $d\sigma$  are listed for each range of  $Q^2$ ,  $p_T(\Lambda + \bar{\Lambda})$  and  $\eta(\Lambda + \bar{\Lambda})$ .

$Q^2$ Range (GeV <sup>2</sup> )	$N(\Lambda + \bar{\Lambda})$	$d\sigma/dQ^2(\Lambda + \bar{\Lambda})$
25 – 75	$2,307.04 \pm 58.12$	$81.48 \pm 2.32$
75 – 125	$334.95 \pm 23.17$	$13.39 \pm 0.92$
125 - 175	$108.55 \pm 13.64$	$4.34 \pm 0.54$

$p_T$ Range (GeV)	$N(\Lambda + \bar{\Lambda})$	$d\sigma/dp_T(\Lambda + \bar{\Lambda})$ (pb/GeV)
0.6 – 0.9	$448.73 \pm 31.31$	$2,990.37 \pm 208.65$
0.9 – 1.2	$587.53 \pm 30.83$	$3,915.35 \pm 205.45$
1.2 – 1.5	$491.18 \pm 26.59$	$3,273.26 \pm 177.19$
1.5 – 1.8	$418.45 \pm 24.05$	$2,788.58 \pm 136.53$
1.8 – 2.1	$355.84 \pm 22.17$	$2,371.35 \pm 147.74$
2.1 – 2.5	$381.54 \pm 23.17$	$1,906.96 \pm 115.80$

$\eta$ Range	$N(\Lambda + \bar{\Lambda})$	$d\sigma/d\eta(\Lambda + \bar{\Lambda})$
(-1.2) – (-0.4)	$661.34 \pm 31.87$	$1,652.71 \pm 79.64$
(-0.4) – 0.4	$864.63 \pm 36.48$	$2,160.73 \pm 91.16$
0.4 – 1.2	$1,152.27 \pm 42.43$	$2,879.56 \pm 106.03$

**Table 6.14:** Differential  $\Lambda + \bar{\Lambda}$  baryon cross section,  $d\sigma$ , measured as a function of  $Q^2$ ,  $p_T(\Lambda + \bar{\Lambda})$  and  $\eta(\Lambda + \bar{\Lambda})$  in MC. The number of  $\Lambda + \bar{\Lambda}$  baryons,  $N_{\Lambda + \bar{\Lambda}}$  and the differential cross section  $d\sigma$  are listed for each range of  $Q^2$ ,  $p_T(\Lambda + \bar{\Lambda})$  and  $\eta(\Lambda + \bar{\Lambda})$ .

#### 6.2.2.4 Inclusive $K_s^0$ meson cross-sections in bins of $Q^2$ , $p_T(K_s^0)$ and $\eta(K_s^0)$ .

The differential  $K_s^0$  meson cross-sections as a function of  $Q^2$ ,  $p_T(K_s^0)$  and  $\eta(K_s^0)$  are shown in Figure 6.8 and listed in Table 6.15 for data and Table 6.16 for MC. The mass plots used in the calculation of these differential cross sections can be found in Section 5.4.

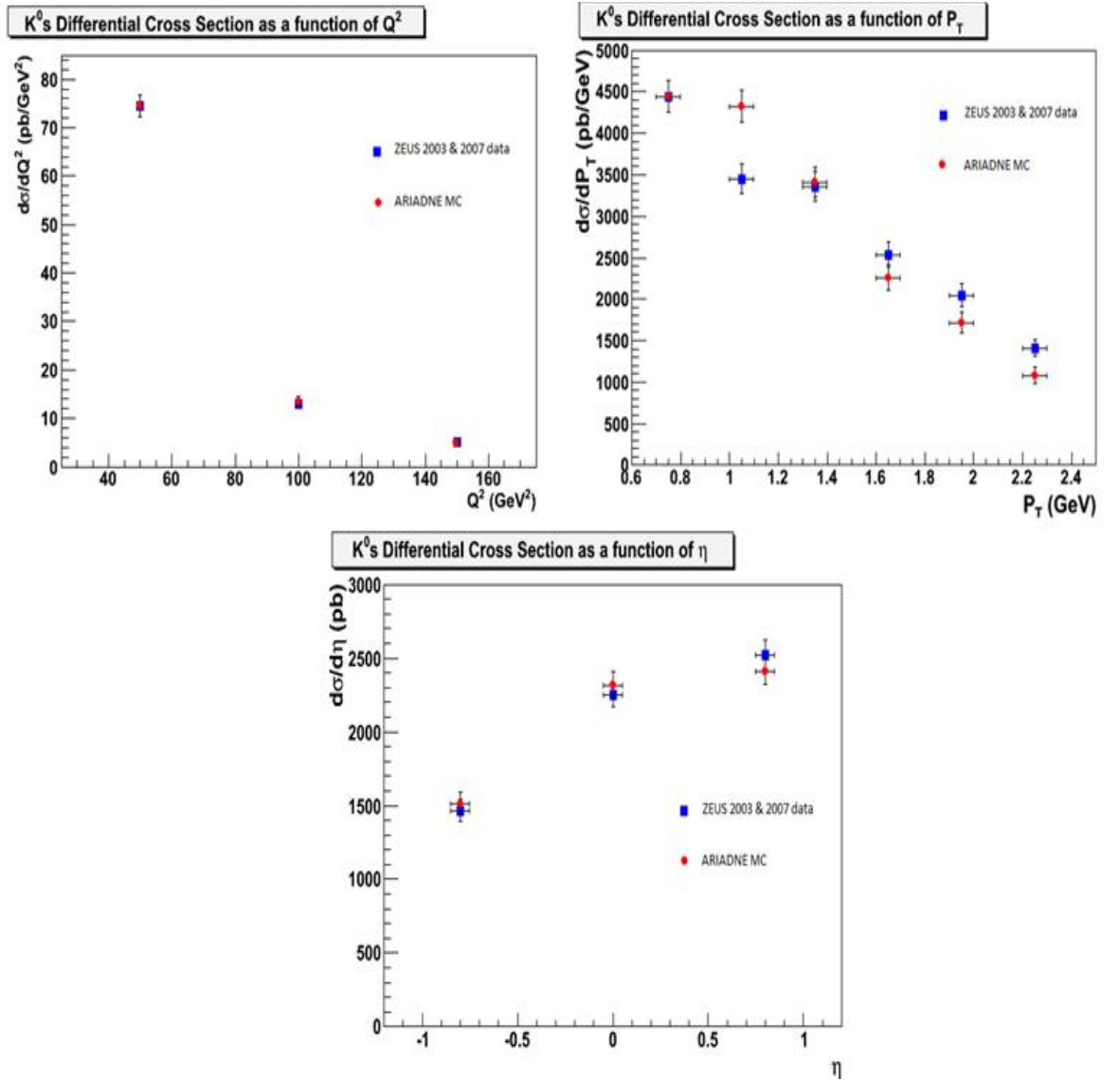


**Figure 6.8:** Differential cross-sections for  $K_s^0$  production in high  $Q^2$  DIS events with  $Q_{DA}^2 > 25$  GeV<sup>2</sup> as a function of  $Q^2$ ,  $p_T(K_s^0)$  and  $\eta(K_s^0)$ . 2003 & 2007 HERA-II data and ARIADNE MC are shown.



$Q^2$ Range (GeV <sup>2</sup> )	$N(K_s^0)$	$d\sigma/dQ^2(K_s^0)$
25 – 75	1,642.52 $\pm$ 51.11	74.56 $\pm$ 2.31
75 – 125	287.32 $\pm$ 20.55	13.04 $\pm$ 0.93
125 – 175	109.86 $\pm$ 12.02	4.98 $\pm$ 0.54

$p_T$ Range (GeV)	$N(K_s^0)$	$d\sigma/dp_T(K_s^0)$ (pb/GeV)
0.6 – 0.9	586.49 $\pm$ 24.54	4,437.59 $\pm$ 185.67
0.9 – 1.2	455.51 $\pm$ 23.75	3,446.55 $\pm$ 179.70
1.2 – 1.5	443.73 $\pm$ 23.14	3,357.42 $\pm$ 175.08
1.5 – 1.8	334.47 $\pm$ 20.46	2,530.71 $\pm$ 154.80
1.8 – 2.1	270.23 $\pm$ 17.77	2,044.65 $\pm$ 134.45
2.1 – 2.5	247.56 $\pm$ 17.88	1,404.84 $\pm$ 101.46

$\eta$ Range	$N(K_s^0)$	$d\sigma/d\eta(K_s^0)$
(-1.2) – (-0.4)	515.61 $\pm$ 25.75	1,462.98 $\pm$ 73.06
(-0.4) – 0.4	793.15 $\pm$ 30.63	2,250.47 $\pm$ 86.90
0.4 – 1.2	888.88 $\pm$ 34.54	2,522.09 $\pm$ 98.00

**Table 6.15:** Differential  $K_s^0$  meson cross section,  $d\sigma$ , measured as a function of  $Q^2$ ,  $p_T(K_s^0)$  and  $\eta(K_s^0)$  in data. The number of  $K_s^0$  meson,  $N_{K_s^0}$  and the differential cross section  $d\sigma$  are listed for each range of  $Q^2$ ,  $p_T(K_s^0)$  and  $\eta(K_s^0)$ .

$Q^2$ Range (GeV <sup>2</sup> )	$N(K_s^0)$	$d\sigma/dQ^2(K_s^0)$
25 – 75	7,191.27 $\pm$ 100.03	335.73 $\pm$ 4.66
75 – 125	1,295.66 $\pm$ 45.71	60.49 $\pm$ 2.13
125 - 175	462.80 $\pm$ 25.39	21.60 $\pm$ 1.18

$p_T$ Range (GeV)	$N(K_s^0)$	$d\sigma/dp_T(K_s^0)$ (pb/GeV)
0.6 – 0.9	2,533.25 $\pm$ 54.22	19,711.69 $\pm$ 421.89
0.9 – 1.2	2,470.01 $\pm$ 53.12	19,219.60 $\pm$ 413.33
1.2 – 1.5	1,943.96 $\pm$ 50.25	15,126.31 $\pm$ 391.00
1.5 – 1.8	1,289.64 $\pm$ 43.02	10,034.92 $\pm$ 334.74
1.8 – 2.1	977.83 $\pm$ 34.44	7,608.67 $\pm$ 267.98
2.1 – 2.5	820.68 $\pm$ 37.39	4,789.39 $\pm$ 218.20

$\eta$ Range	$N(K_s^0)$	$d\sigma/d\eta(K_s^0)$
(-1.2) – (-0.4)	2,344.74 $\pm$ 53.49	6,841.82 $\pm$ 156.08
(-0.4) – 0.4	3,596.51 $\pm$ 68.56	10,494.41 $\pm$ 200.05
0.4 – 1.2	3,744.20 $\pm$ 68.96	10,925.36 $\pm$ 201.22

**Table 6.16:** Differential  $K_s^0$  meson cross section,  $d\sigma$ , measured as a function of  $Q^2$ ,  $p_T(K_s^0)$  and  $\eta(K_s^0)$  in MC. The number of  $K_s^0$  meson,  $N_{K_s^0}$  and the differential cross section  $d\sigma$  are listed for each range of  $Q^2$ ,  $p_T(K_s^0)$  and  $\eta(K_s^0)$ .

### 6.3 Baryon-to-Antibaryon Production Asymmetry

The Baryon Number (BN) transfer from the initial proton to a final baryon can be determined by measuring the production asymmetry of a baryon to its anti-partner. The impact of the initial proton on the baryon to antibaryon production asymmetry could be small or negligible in the central part of the detector region at HERA since the Baryon Number (BN) is expected to escape the detector in a different region.

The results from the baryon-antibaryon production asymmetry could give a hint on how the presence of the initial proton affects the  $\Lambda$  production in the final state. In the first place we assume the sea quarks in the proton will not result in any production difference for  $\Lambda$  baryon to its anti-partner,  $\bar{\Lambda}$ . Because of  $\bar{\Lambda}$  does not have any valence quarks in common with the initial proton, it acts as a reference for  $\Lambda$  baryon production.

The baryon-antibaryon asymmetry  $A$  is defined as [54]:

$$A = \frac{N(\Lambda) - N(\bar{\Lambda})}{N(\Lambda) + N(\bar{\Lambda})}, \quad (7.3)$$

where  $N(\Lambda)$ ,  $N(\bar{\Lambda})$  is the number of  $\Lambda$  and  $\bar{\Lambda}$  baryons, respectively. The ARIADNE MC prediction was used to compared the baryon-antibaryon asymmetry  $A$ . The results are shown below:

- At high  $Q^2$ :  $A = -0.03 \pm 5.1\%$ , compared to the ARIADNE prediction of  $1.19 \pm 2.5\%$  ;
- At Low  $Q^2$ :  $A = -0.95 \pm 2.1\%$ , compared to the ARIADNE prediction of  $2.18 \pm 1.3\%$  ;

The baryon-antibaryon asymmetry for both high  $Q^2$  and low  $Q^2$  DIS events showed there are no asymmetries detected and agreeable with asymmetries expected by Monte Carlo.

This HERA-II baryon-antibaryon production asymmetry was different compared to the previous studies on HERA-I data. This is due to difference center of mass energy, integrated luminosity for the data and difference momentum value of the proton.

The baryon-antibaryon asymmetry for HERA-II data is negative compared to HERA-I. The following values were obtained from HERA-I data [54]:

- At high  $Q^2$ :  $A = 0.3 \pm 1.3\%$ , compared to the ARIADNE prediction of  $0.4 \pm 0.2\%$ ;
- At Low  $Q^2$ :  $A = 1.2 \pm 1.6\%$ , compared to the ARIADNE prediction of  $1.0 \pm 0.2\%$ ;

In conclusion, no asymmetry  $\Lambda - \bar{\Lambda}$  was found though it can be expected in the case of the baryon number transport from initial proton to baryon system. Further studies can be done to HERA-II data to give a better value for the baryon-antibaryon production asymmetry.

The results below showed the  $\Lambda - \bar{\Lambda}$  asymmetry for ZEUS 2003 & 2007 data and ARIADNE Monte Carlo samples as a function of  $\eta$ ,  $Q^2$  and  $P_T$  in the laboratory frame for low  $Q^2$  and high  $Q^2$  Deep Inelastic Scattering events. The error bars represent the statistical errors for the measurements.

### 6.3.1 Low $Q^2$ DIS Events ( $5 < Q_{DA}^2 < 25 \text{ GeV}^2$ )

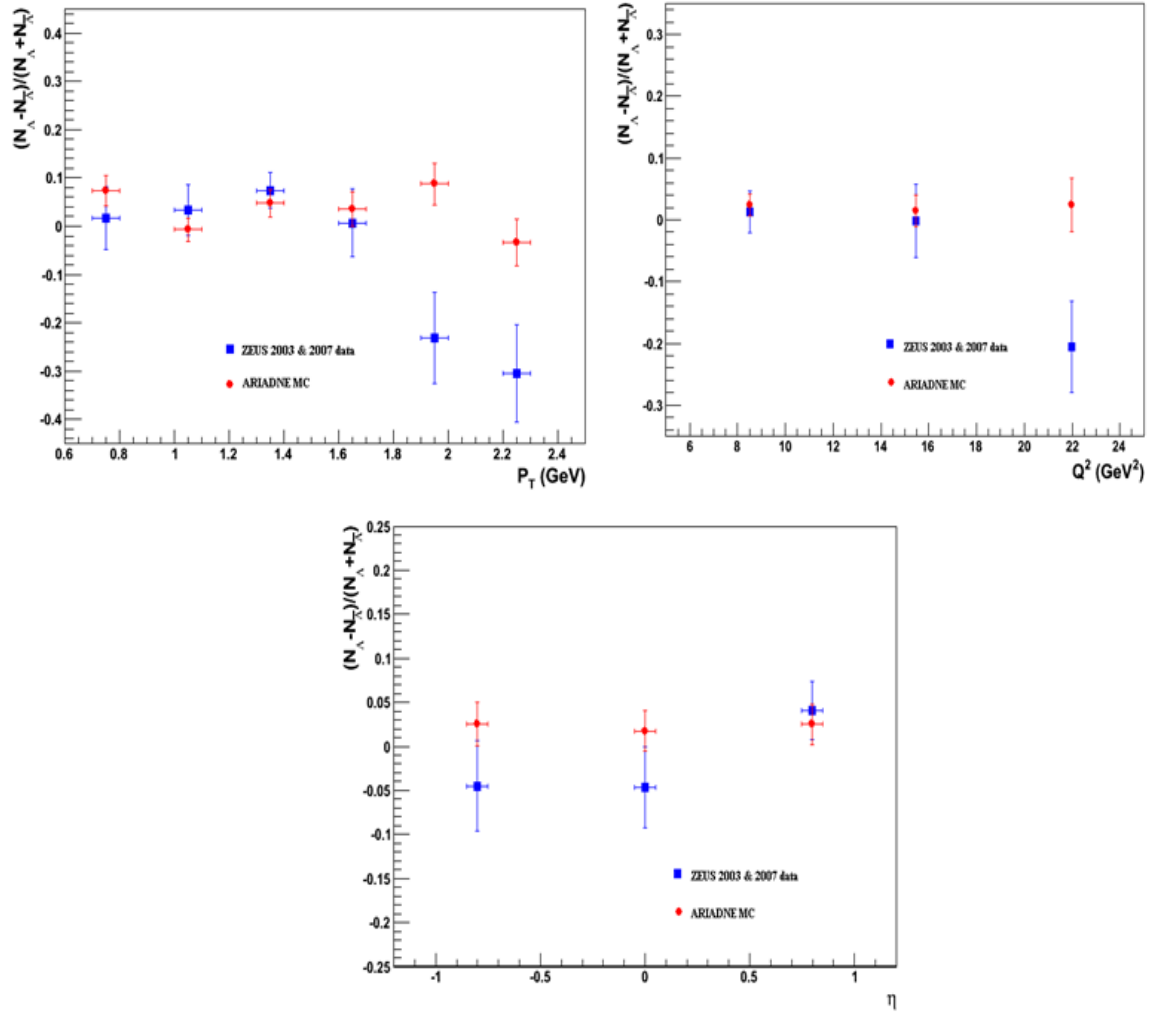


**Figure 6.9:** The  $\Lambda - \bar{\Lambda}$  asymmetry for ZEUS 2003 & 2007 data and ARIADNE Monte Carlo samples as a function of  $\eta$ ,  $Q^2$  and  $p_T$  in the laboratory frame for Low  $Q^2$  DIS events with  $5 < Q_{DA}^2 < 25 \text{ GeV}^2$ . The  $N(\Lambda)$ ,  $N(\bar{\Lambda})$  is the number of  $\Lambda$  and  $\bar{\Lambda}$  baryons, respectively. The error bars represent the statistical errors for the measurements.

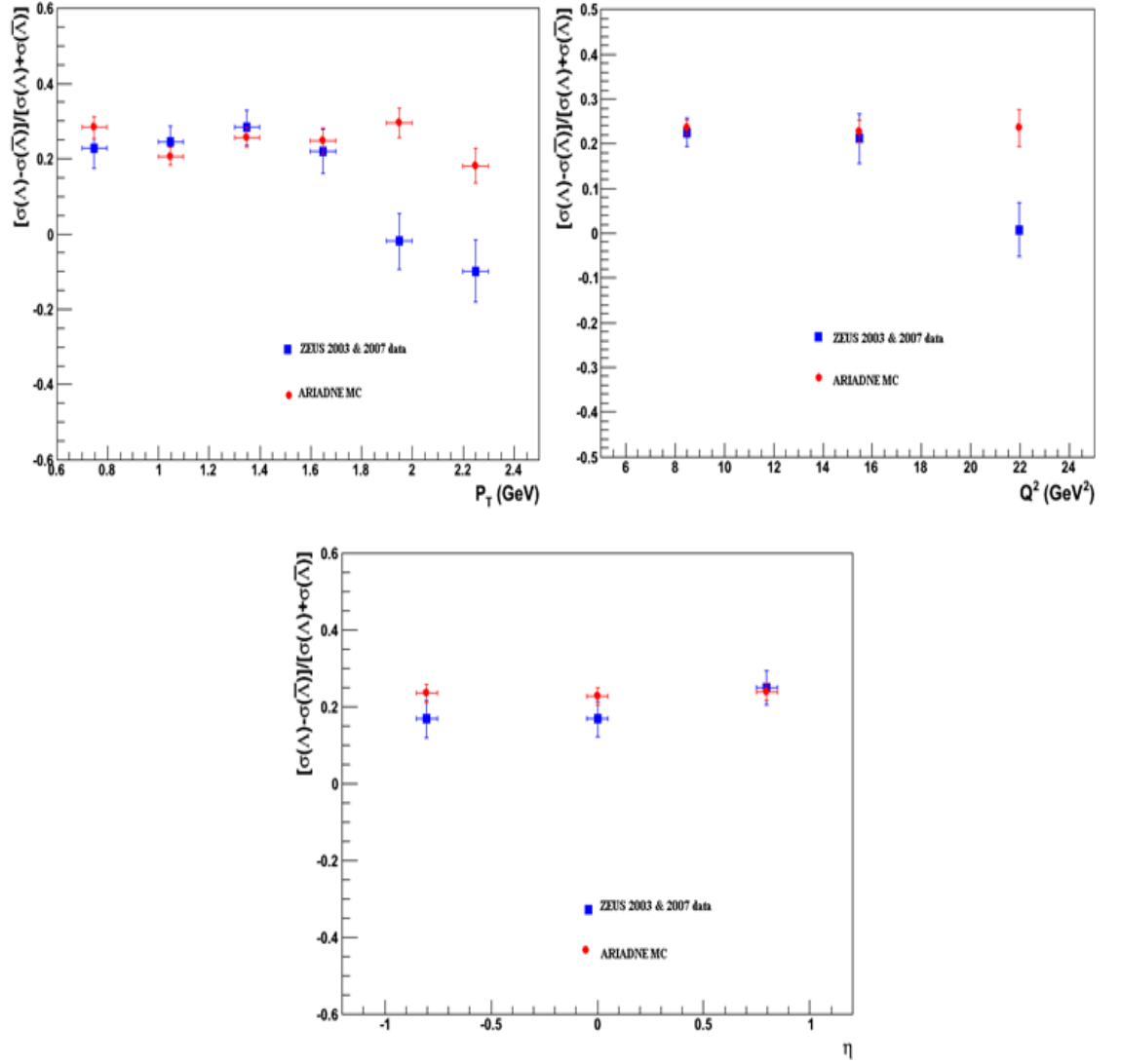


**Figure 6.10:** The  $\Lambda - \bar{\Lambda}$  asymmetry for ZEUS 2003 & 2007 data and ARIADNE Monte Carlo samples as a function of  $\eta$ ,  $Q^2$  and  $p_T$  in the laboratory frame for Low  $Q^2$  DIS events with  $5 < Q_{DA}^2 < 25$  GeV<sup>2</sup>. The  $\sigma(\Lambda)$ ,  $\sigma(\bar{\Lambda})$  is the differential cross section of  $\Lambda$  and  $\bar{\Lambda}$  baryons, respectively. The error bars represent the statistical errors for the measurements.

### 6.3.2 High $Q^2$ DIS Events ( $Q_{DA}^2 > 25 \text{ GeV}^2$ )

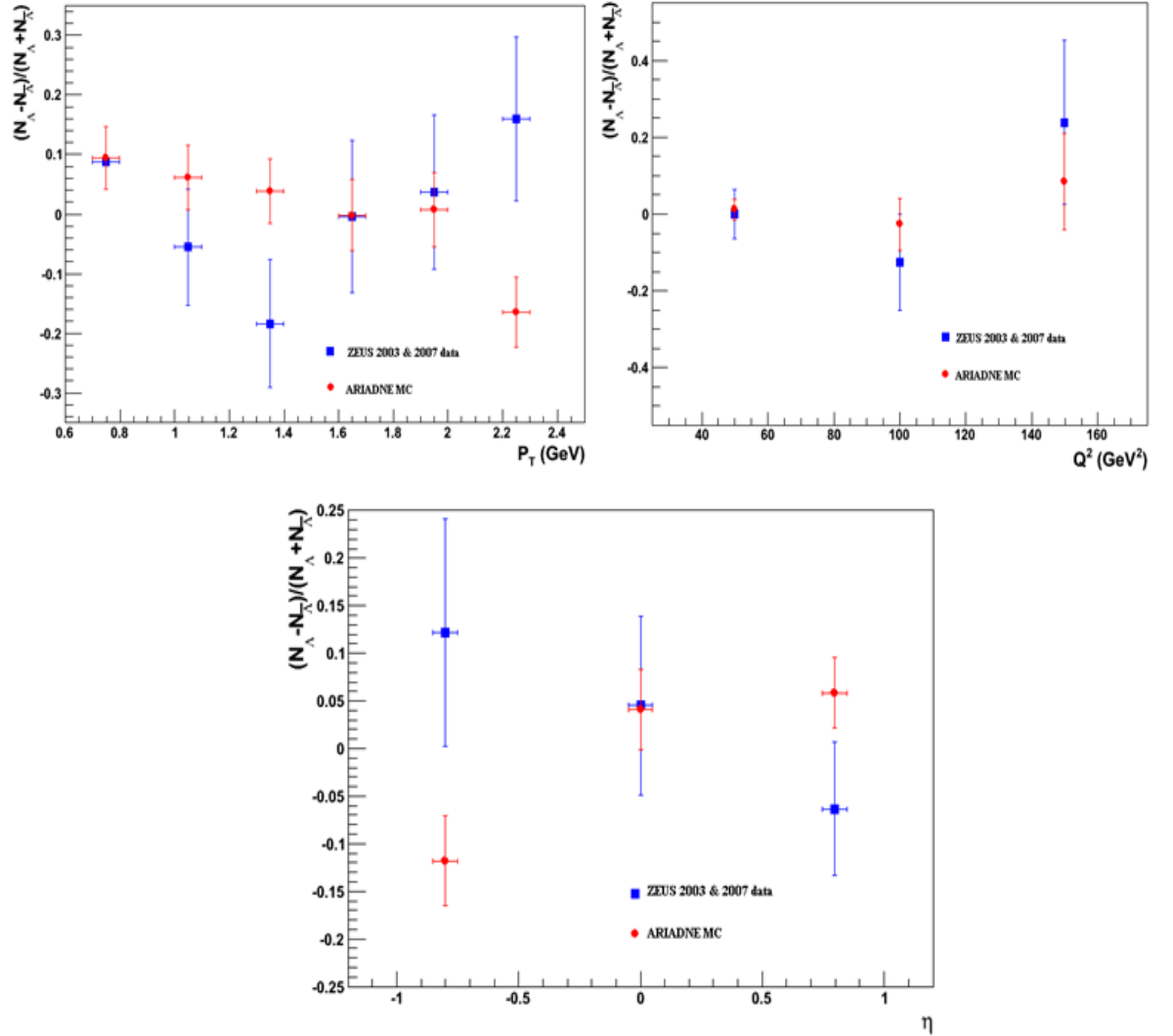


**Figure 6.11:** The  $\Lambda - \bar{\Lambda}$  asymmetry for ZEUS 2003 & 2007 data and ARIADNE Monte Carlo samples as a function of  $\eta$ ,  $Q^2$  and  $P_T$  in the laboratory frame for High  $Q^2$  DIS events with  $Q_{DA}^2 > 25 \text{ GeV}^2$ . The  $N(\Lambda)$ ,  $N(\bar{\Lambda})$  is the number of  $\Lambda$  and  $\bar{\Lambda}$  baryons, respectively. The error bars represent the statistical errors for the measurements.

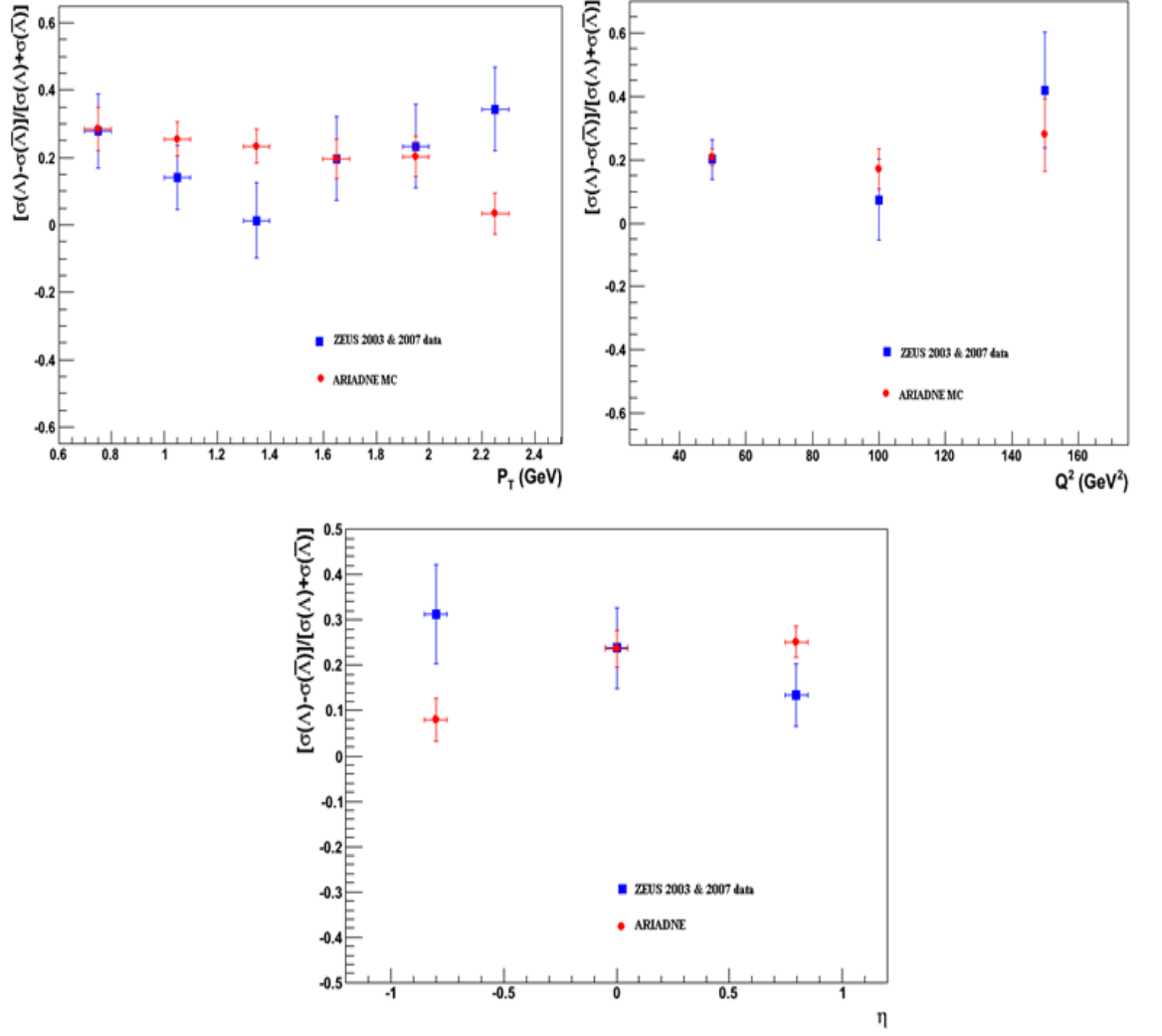


**Figure 6.12:** The  $\Lambda - \bar{\Lambda}$  asymmetry for ZEUS 2003 & 2007 data and ARIADNE Monte Carlo samples as a function of  $\eta$ ,  $Q^2$  and  $P_T$  in the laboratory frame for High  $Q^2$  DIS events with  $Q_{DA}^2 > 25 \text{ GeV}^2$ . The  $\sigma(\Lambda)$ ,  $\sigma(\bar{\Lambda})$  is the differential cross section of  $\Lambda$  and  $\bar{\Lambda}$  baryons, respectively. The error bars represent the statistical errors for the measurements.



## 6.4 Baryon-to-Meson Ratio

The baryon to meson ratio cannot be explained by the standard fragmentation approach because the values become so large in various regions of the heavy ion collision phase space in Relativistic Heavy Ion Collider (RHIC) experiments [49]. The parton recombination model was produced as an alternative to the fragmentation model. In this model, if the quarks are produced so close together, the quarks can combine to form baryons or mesons without having to pull more quarks out of the vacuum.

The  $ep$  collision provided by HERA should be able to provide useful information on the various mechanisms that lead to baryon and meson formation.

The baryon to meson ratio,  $\mathfrak{R}$  in the  $\Lambda - K_s^0$  system is defined as:

$$\mathfrak{R} = \frac{\sigma(\Lambda) + \sigma(\bar{\Lambda})}{\sigma(K_s^0)}, \quad (7.4)$$

where  $\sigma(\Lambda)$ ,  $\sigma(\bar{\Lambda})$  and  $\sigma(K_s^0)$  is the differential cross section of  $\Lambda$  and  $\bar{\Lambda}$  baryons and  $K_s^0$  meson, respectively. The differential cross sections presented in Section 6.2 are used to obtain this ratio as a function of the same variables,  $\eta$ ,  $Q^2$  and  $p_T$ .

The average baryon to meson ratio  $\mathfrak{R}$  has been measured using HERA-II data and compared to MC prediction from ARIADNE. The results are shown below:

- At High  $Q^2$ :  $\mathfrak{R} = 43.49 \pm 2.07\%$ , compared to the ARIADNE prediction of  $39.45 \pm 0.92\%$ ;
- At Low  $Q^2$ :  $\mathfrak{R} = 39.50 \pm 0.33\%$ , compared to the ARIADNE prediction of  $37.02 \pm 0.44\%$ ;

The value of baryon to meson ratio for HERA-II data was larger compared to the previous results for HERA-I data. This is due to different center of mass energy, integrated luminosity for the data and the difference momentum value of the proton. Table 6.17 shows the average  $\Lambda$  to  $K_s^0$  production ratio for HERA-II data compared to the previous HERA-I data.

The following values were obtained from HERA-I data:

- At high  $Q^2$ :  $\mathfrak{R} = 36.44 \pm 0.51\%$  , compared to the ARIADNE prediction of  $33.17 \pm 0.14\%$  ;
- At Low  $Q^2$ :  $\mathfrak{R} = 36.57 \pm 0.60\%$  , compared to the ARIADNE prediction of  $36.49 \pm 0.18\%$  ;

KINEMATICS REGIONS	DATA	$\mathfrak{R}(\%)$
High $Q^2$ DIS ( $Q_{DA}^2 > 25 \text{ GeV}^2$ )	HERA-II (ZEUS 03 & 07)	$43.49 \pm 2.07$
	HERA-I (ZEUS 96-00)	$36.44 \pm 0.51$
Low $Q^2$ DIS ( $5 < Q_{DA}^2 < 25 \text{ GeV}^2$ )	HERA-II (ZEUS 03 & 07)	$39.50 \pm 0.33$
	HERA-I (ZEUS 96-00)	$36.57 \pm 0.60$

**Table 6.17:** The average  $\Lambda$  to  $K_s^0$  production ratio for HERA-II data compared to the previous HERA-I data. The statistical uncertainties are shown for the data.

In conclusion, HERA-II data gives a larger value for baryon to meson ratio compared to the HERA-I data. This is due to the luminosity upgrade and the tracking detector upgrade during the HERA-II running period. Further studies can be done to HERA-II data to give a better understanding on how the meson and baryon produces in the HERA-II data.

The results below showed the  $(\Lambda + \bar{\Lambda})/K_s^0$  ratio for ZEUS 2003 & 2007 data and ARIADNE Monte Carlo samples as a function of  $\eta$ ,  $Q^2$  and  $p_T$  in the laboratory frame for low  $Q^2$  and high  $Q^2$  Deep Inelastic Scattering events. The error bars represent the statistical errors for the measurements.

#### 6.4.1 Low $Q^2$ DIS Events ( $5 < Q_{DA}^2 < 25 \text{ GeV}^2$ )

The baryon to meson ratio in the Low  $Q^2$  sample as a function of  $\eta$ ,  $Q^2$  and  $p_T$  can be seen in Figure 6.11, with the expectation from the ARIADNE MC shown for the comparison.

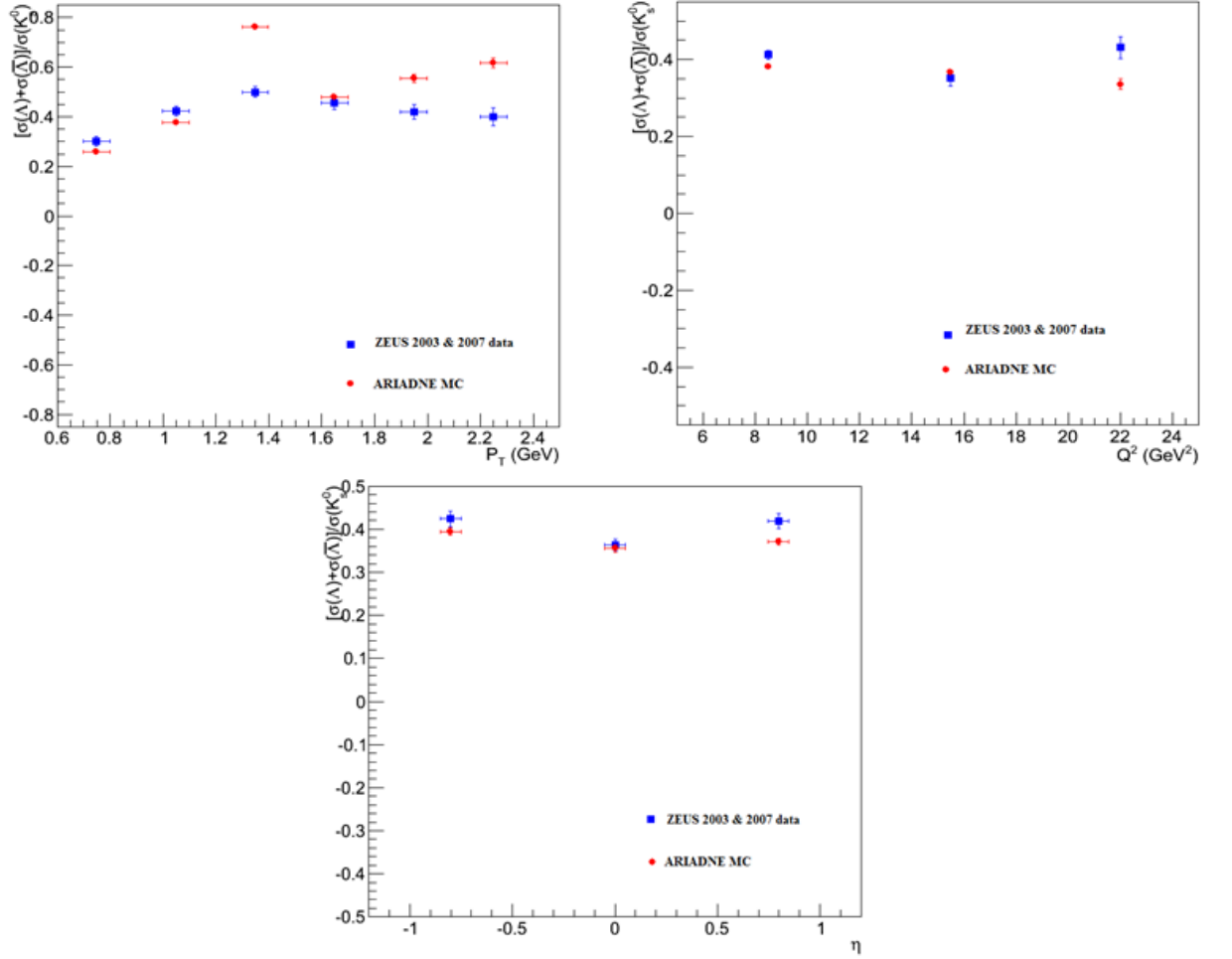


**Figure 6.13:** The  $(\Lambda + \bar{\Lambda})/K_s^0$  ratio for ZEUS 2003 & 2007 data and ARIADNE Monte Carlo samples as a function of  $\eta$ ,  $Q^2$  and  $p_T$  in the laboratory frame for Low  $Q^2$  DIS events with  $5 < Q_{DA}^2 < 25 \text{ GeV}^2$ . The  $\sigma(\Lambda)$ ,  $\sigma(\bar{\Lambda})$  and  $\sigma(K_s^0)$  is the differential cross section of  $\Lambda$  and  $\bar{\Lambda}$  baryons, and  $K_s^0$  meson respectively. The error bars represent the statistical errors for the measurements.

### 6.4.2 High $Q^2$ DIS Events ( $Q_{DA}^2 > 25 \text{ GeV}^2$ )

The baryon to meson ratio in the High  $Q^2$  sample as a function of  $\eta$ ,  $Q^2$  and  $P_T$  can be seen in Figure 6.12, with the expectation from the ARIADNE MC shown for the comparison.

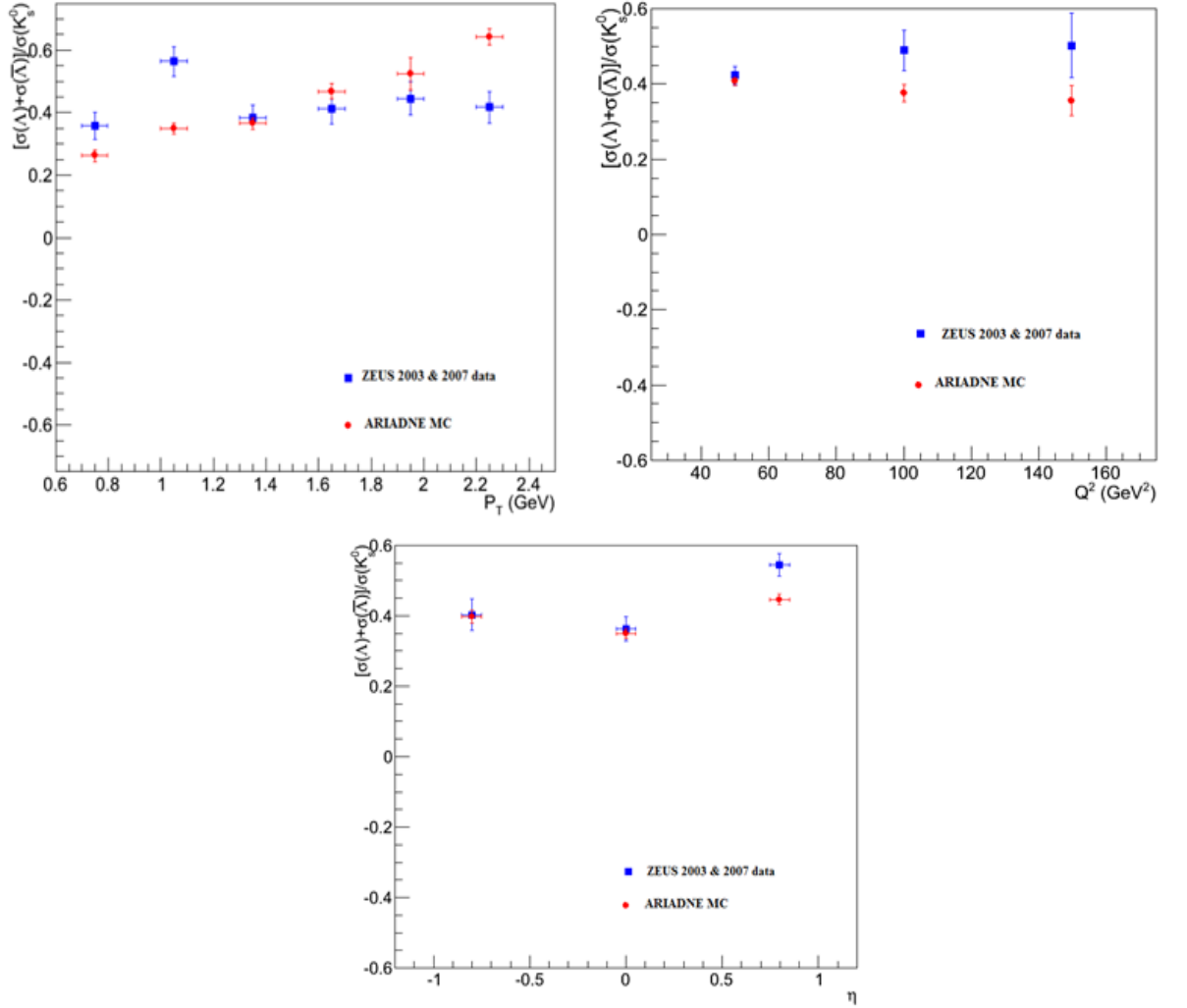


**Figure 6.14:** The  $(\Lambda + \bar{\Lambda})/K_s^0$  ratio for ZEUS 2003 & 2007 data and ARIADNE Monte Carlo samples as a function of  $\eta$ ,  $Q^2$  and  $P_T$  in the laboratory frame for High  $Q^2$  DIS events with  $Q_{DA}^2 > 25 \text{ GeV}^2$ .

The  $\sigma(\Lambda)$ ,  $\sigma(\bar{\Lambda})$  and  $\sigma(K_s^0)$  is the differential cross section of  $\Lambda$  and  $\bar{\Lambda}$  baryons, and  $K_s^0$  meson respectively. The error bars represent the statistical errors for the measurements.

## 6.5 Baryon Antibaryon Rapidity Correlations

In high energy physics, the baryon production process is not well understood yet and therefore it relies much on phenomenological models like the cluster and string models. The string and cluster models differ in many aspects, though some common features exist. One of the common features is the local compensation of quantum numbers (the electric charge or flavor or baryon number) between the neighbouring created hadrons. Correlation happened when the hadrons are expected to be produced close in rapidity if they share the same string break-up [11].

Due to the high mass of strange baryons, its inclusive production rates give direct test of various hadronization model, while their flavor correlations probe the detailed color confinement mechanism in the baryon formation process [24].

Baryon production in  $ep$  collision events not only provides a tool to investigate the process of quarks fragmentation into hadrons, but also because baryons are heavy and suffer relatively little momentum spreading due to resonance decays, they provided a convenient probe to study the dynamics leading for the production of primary hadrons from the color field of the initial quarks.

Plentiful production of strange particles at HERA provides useful information to understand the strangeness production in hadronization process. Rapidity correlation between particles is used to investigate local conservation of quark flavor and baryon number in hadronization process.

### 6.5.1 Rapidity Correlation

The particle rapidity correlations can be used to study the local quantum number conservation during the hadronization process [28]. For example, in the case of strangeness, several question has been asked, whether a strange particle and a corresponding anti-strange particle tend to produced “close” to each other within the event, or whether those particles are associated with the initial  $s$  and  $\bar{s}$  quarks, respectively in  $s\bar{s}$  events or with the initial  $u$  and  $\bar{u}$  in  $u\bar{u}$  events, or whether the strange and anti-strange particles are distributed randomly throughout the event [56]. By studying the rapidity correlation between two particles, we can obtain a further dynamic picture of the hadronization stage.

Measurements of the rapidity correlations between  $\Lambda\bar{\Lambda}$  pairs provide good test of baryon production in fragmentation models. Models of baryon formation in the fragmentation process, such as “di-quarks” and “popcorn” models, predict different baryon-antibaryon correlations [24].

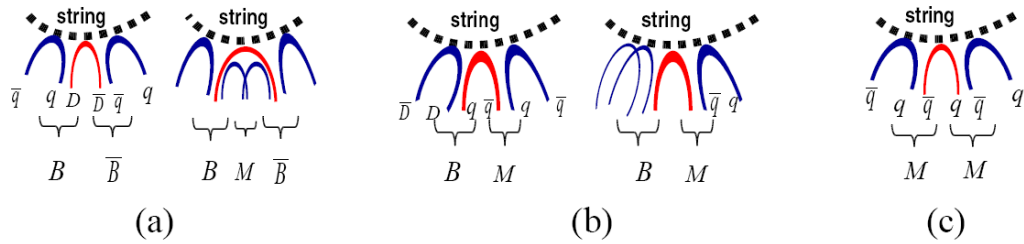


**Figure 6.15:** An illustration of the particle pair correlations proposed in the string model due to sharing of a common string break-up. The dotted line represents a string and the solid curves describe the development of a  $q\bar{q}$  or  $D\bar{D}$  pair created at some break-up points in a string. Here  $q$ ,  $\bar{q}$ ,  $D$ ,  $\bar{D}$ ,  $B$ ,  $\bar{B}$  and  $M$  denote a quark, antiquark, diquark, antidiquark, baryon, antibaryon and meson, respectively. Figure (a) shows the correlation between a baryon-antibaryon pair. The figures (b) and (c) show such correlation for baryon-meson and meson-meson pairs, respectively [42].

### 6.5.2 Events Selection and Strangeness Production

In this thesis we present data on baryon-baryon and baryon-antibaryon correlations, based on the analysis of events containing two or more  $\Lambda$  or  $\bar{\Lambda}$ . The data were recorded with the ZEUS detector at HERA  $ep$  collider using an integrated luminosity of  $4.60 \text{ pb}^{-1}$ .

The same selection criteria were used to select the events for this analysis as in Section 3.5.2, except for the value of transverse momentum,  $p_T$  and pseudorapidity  $\eta$ . Alternatively, the  $p_T$  and  $\eta$  for the correlation measurements were loosely restricted to be  $0.3 < p_T < 5.0 \text{ GeV}$  and  $|\eta| < 1.5$  in order to obtain an event sample with larger statistics.

The number of  $\Lambda$  and  $\bar{\Lambda}$  must be equal to one in order to exclude possible uncorrelated background. The particle pair  $\Lambda$  and  $\bar{\Lambda}$  do not share a same track. This study of baryon correlations uses  $\Lambda$  and  $\bar{\Lambda}$  reconstructed using two oppositely charged tracks associated with a displaced secondary vertex.

The  $\Lambda(\bar{\Lambda})$  candidates were reconstructed by their charged decay mode to  $p\pi^- (\bar{p}\pi^+)$  (branching ratio  $63.9 \pm 0.5\%$  [30]). The track with the larger momentum was assigned the mass of the proton, while the other was assigned the mass of the charged pion, as the decay proton always has a larger momentum than the pion, provided the  $\Lambda(\bar{\Lambda})$  momentum is greater than  $0.3 \text{ GeV}$ . For accurate invariant mass reconstruction, the momentum vectors need to be given at the decay vertex. All tracks used in invariant mass reconstruction must be vertex tracks.



### 6.5.3 Results and Discussion

Baryon Antibaryon correlation in Deep Inelastic Scattering events were studied using the ZEUS 2003 & 2007 data with an integrated luminosity =  $4.60 \text{ pb}^{-1}$ .

Table 6.18 shows the correlation between several pairs of  $\Lambda$  and  $\bar{\Lambda}$  in ZEUS 2003 & 2007 data while Table 6.19 for the ARIADNE MC. Figure 6.16 shows the relation between the number of lambda and the number of antilambda. There is a positive correlation between these two particles.

Figure 6.17 shows the  $\Lambda\bar{\Lambda}$  rapidity distribution for the Deep Inelastic Scattering events. The peak near to 0 rapidity difference shows us at the interaction point during the collision,  $\Lambda$  and  $\bar{\Lambda}$  tends to produce close to each other. Correlation happened when the hadrons are expected to be produced close in rapidity if they share the same string break-up. There is symmetry between the data and the MC. The data agree with the popcorn model from ARIADNE, which uses the Lund string model for the hadronization process.

		$\bar{\Lambda}$	$\bar{\Lambda}\bar{\Lambda}$	$\bar{\Lambda}\bar{\Lambda}\bar{\Lambda}$	$\bar{\Lambda}\bar{\Lambda}\bar{\Lambda}\bar{\Lambda}$
	4,205,730	1,848	13	1	0
$\Lambda$	1,782	96	19	1	1
$\Lambda\Lambda$	0	0	0	0	0
$\Lambda\Lambda\Lambda$	0	0	0	0	0
$\Lambda\Lambda\Lambda\Lambda$	0	0	0	0	0

**Table 6.18:** The number of  $\Lambda$  and  $\bar{\Lambda}$  for ZEUS 2003 & 2007 data.

		$\bar{\Lambda}$	$\bar{\Lambda}\bar{\Lambda}$	$\bar{\Lambda}\bar{\Lambda}\bar{\Lambda}$	$\bar{\Lambda}\bar{\Lambda}\bar{\Lambda}\bar{\Lambda}$
	5,454,110	5,913	38	1	0
$\Lambda$	5,963	288	54	3	3
$\Lambda\Lambda$	0	0	0	0	0
$\Lambda\Lambda\Lambda$	0	0	0	0	0
$\Lambda\Lambda\Lambda\Lambda$	0	0	0	0	0

**Table 6.19:** The number of  $\Lambda$  and  $\bar{\Lambda}$  for ARIADNE.

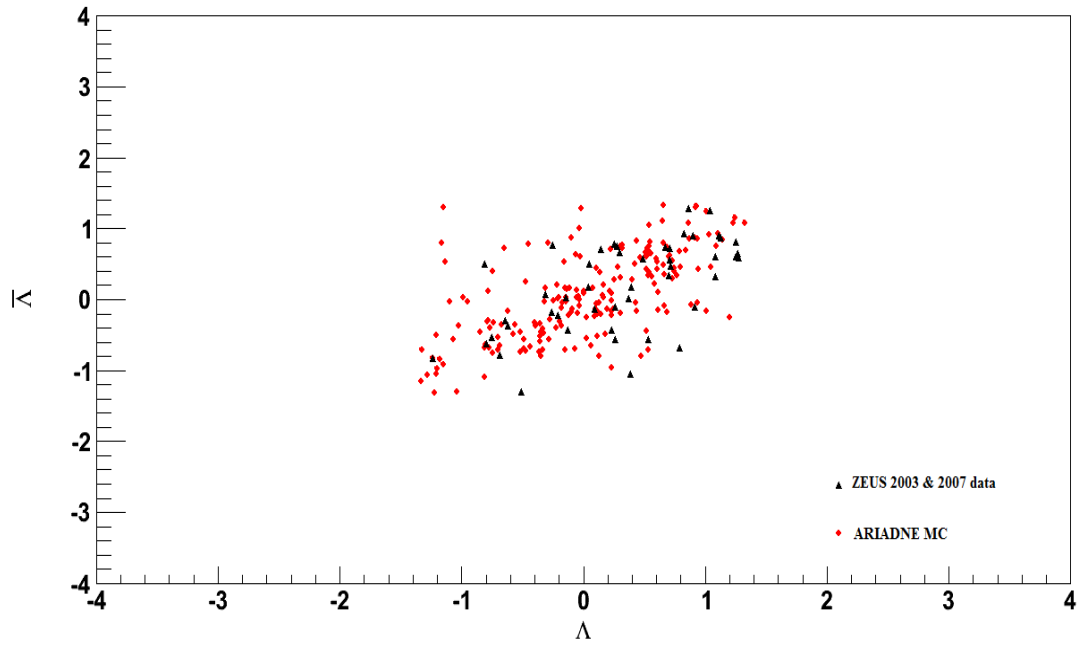


**Figure 6.16:** The  $\Lambda\bar{\Lambda}$  correlation for ZEUS 2003 & 2007 data compared to the ARIADNE data. The black triangles represent the data while the red circles for the MC. The figure clearly shows correlation between baryon and its antiparticle, antibaryon.

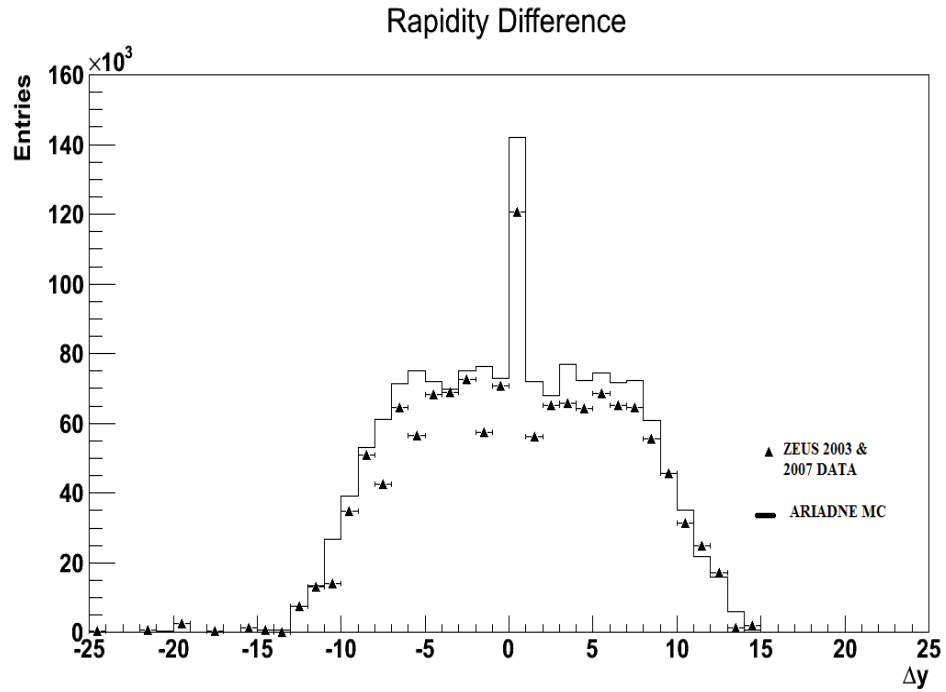


**Figure 6.17:** The  $\Lambda\bar{\Lambda}$  rapidity distribution for the Deep Inelastic Scattering events. The MC is normalized to the data and represents by the line while the pulse represents the ZEUS data.  $\Lambda\bar{\Lambda}$  clearly correlated at low rapidity difference.

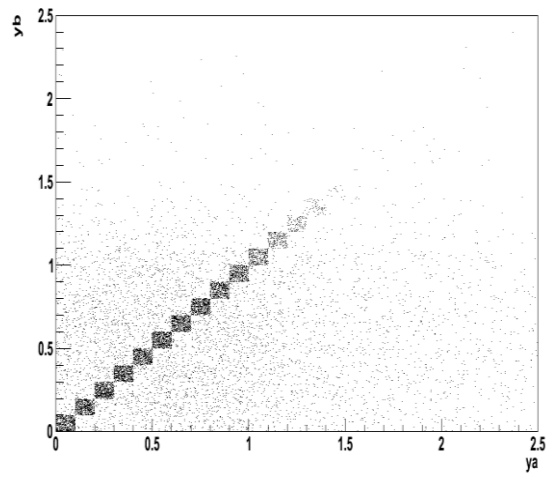
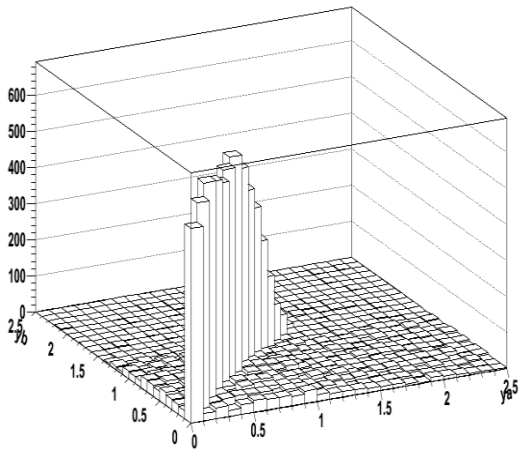
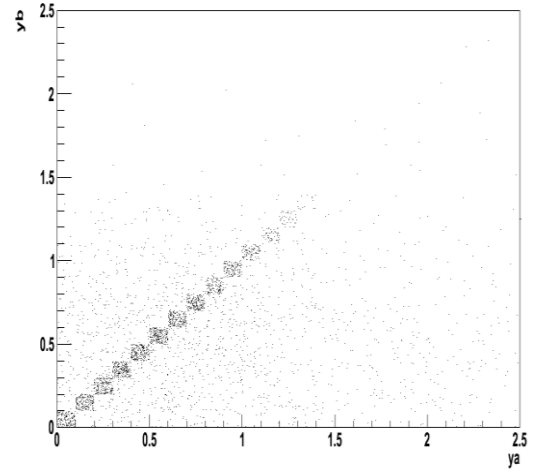
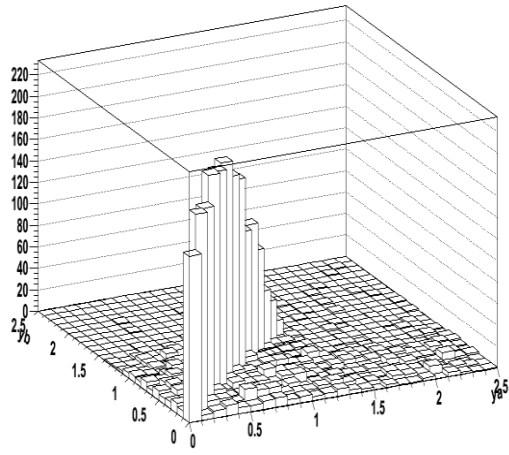


**Figure 6.18:** Rapidity distributions for  $\Lambda$  vs  $\bar{\Lambda}$ . The upper figures represent the distribution for ZEUS 2003 & 2007 data sample while the below figures for ARIADNE MC data sample.

#### **6.5.4 Conclusion**

In conclusion, results clearly show positive correlation between baryon and antibaryon. In the case of strangeness, the strange particle and its corresponding anti-strange particles proved to be produced “close” to each other within the event. The data agree with the popcorn model from ARIADNE, which uses the Lund string model for the hadronization process. Correlation happened when the hadrons are expected to be produced close in rapidity if they share the same string break-up.

# CHAPTER 7

## Conclusion

The strangeness total cross section for  $ep$  neutral current deep inelastic scattering (DIS) has been measured using HERA-II data at a center-of-mass energy of  $\sqrt{s} = 318$  GeV with the ZEUS detector at HERA. The 2003 & 2007 running period data were used with an integrated luminosity of  $4.6 \text{ pb}^{-1}$  and compared with ARIADNE Monte Carlo (MC) predictions. The kinematic region of  $Q_{DA}^2 > 25 \text{ GeV}^2$  and  $0.04 \leq y \leq 0.95$  were chosen for the measurement of the cross sections in the high- $Q^2$  Deep Inelastic Scattering sample and  $5 < Q_{DA}^2 < 25 \text{ GeV}^2$  and  $0.04 \leq y \leq 0.95$  for the low- $Q^2$  sample. The total inclusive production cross-sections in the high  $Q^2$  kinematic range are found to be:

$$\sigma_{\Lambda} = 1,292 \pm 91(stat) pb^{-1},$$

$$\sigma_{\Lambda^-} = 868 \pm 64(stat) pb^{-1},$$

$$\sigma_{\Lambda+\Lambda^-} = 1,286 \pm 71(stat) pb^{-1},$$

$$\sigma_{K_s^0} = 4,966 \pm 120(stat) pb^{-1}$$

The total inclusive production cross-sections in the low  $Q^2$  kinematic range are found to be:

$$\sigma_{\Lambda} = 4,129 \pm 60(stat) pb^{-1},$$

$$\sigma_{\bar{\Lambda}} = 2,733 \pm 106(stat) pb^{-1},$$

$$\sigma_{\Lambda+\bar{\Lambda}} = 4,121 \pm 119(stat) pb^{-1},$$

$$\sigma_{K_s^0} = 17,372 \pm 275(stat) pb^{-1}$$

The differential production cross-sections of  $\Lambda$ ,  $\bar{\Lambda}$ ,  $\Lambda+\bar{\Lambda}$  and  $K_s^0$  are measured in two different kinematic regions,  $Q_{DA}^2 > 25 \text{ GeV}^2$  for high  $Q^2$  DIS sample and  $5 < Q_{DA}^2 < 25 \text{ GeV}^2$  for low  $Q^2$  DIS sample and measured as functions of  $\eta(\Lambda, \bar{\Lambda}, K_s^0)$ ,  $p_T(\Lambda, \bar{\Lambda}, K_s^0)$  and  $Q^2$ . The differential cross section measurements decrease when the value of the variables  $Q^2$  and  $p_T$  increase. The  $\eta$  cross section rises in the forward region for  $\Lambda$ ,  $\bar{\Lambda}$  and  $K_s^0$ .

The baryon-antibaryon production asymmetry, defined as  $\frac{(\Lambda - \bar{\Lambda})}{(\Lambda + \bar{\Lambda})}$ , is studied and the results are compared with ARIADNE MC prediction. The obtained results shown below:

- At high  $Q^2$ :  $A = -0.03 \pm 5.1\%$ , compared to the ARIADNE prediction of  $1.19 \pm 2.5\%$  ;
- At Low  $Q^2$ :  $A = -0.95 \pm 2.1\%$ , compared to the ARIADNE prediction of  $2.18 \pm 1.3\%$  ;

The baryon-antibaryon asymmetry for both high  $Q^2$  and low  $Q^2$  DIS events showed there are no asymmetries detected and agreeable with asymmetries expected by Monte Carlo. The baryon-antibaryon asymmetry for HERA-II data is negative compare to HERA-I. The following values were obtained from HERA-I data [54]:

- At high  $Q^2$ :  $A = 0.3 \pm 1.3\%$ , compared to the ARIADNE prediction of  $0.4 \pm 0.2\%$ ;
- At Low  $Q^2$ :  $A = 1.2 \pm 1.6\%$ , compared to the ARIADNE prediction of  $1.0 \pm 0.2\%$ ;

In conclusion, no asymmetry  $\Lambda - \bar{\Lambda}$  was found though it can be expected in the case of the baryon number transport from initial proton to baryon system. Further studies can be done to HERA-II data to give a better value for the baryon-antibaryon production asymmetry.

The average baryon to meson ratio  $\frac{(\Lambda + \bar{\Lambda})}{K_s^0}$  is studied using HERA-II data and

the results are compared with ARIADNE MC prediction and the previous HERA-I data.

The obtained results shown below:

- At High  $Q^2$ :  $\mathfrak{R} = 43.49 \pm 2.07\%$ , compared to the ARIADNE prediction of  $39.45 \pm 0.92\%$ ;
- At Low  $Q^2$ :  $\mathfrak{R} = 39.50 \pm 0.33\%$ , compared to the ARIADNE prediction of  $37.02 \pm 0.44\%$ ;

The value of baryon to meson ratio for HERA-II data was larger compared to the previous results for HERA-I data. The following values were obtained from HERA-I data:

- At high  $Q^2$ :  $\mathfrak{R} = 36.44 \pm 0.51\%$ , compared to the ARIADNE prediction of  $33.17 \pm 0.14\%$ ;
- At Low  $Q^2$ :  $\mathfrak{R} = 36.57 \pm 0.60\%$ , compared to the ARIADNE prediction of  $36.49 \pm 0.18\%$ ;



In conclusion, HERA-II data gives larger value for baryon to meson ratio compared to the HERA-I data. This is due to the luminosity upgrade and the tracking detector upgrade during the HERA-II running period. Further studies can be done to HERA-II data to give a better understanding on how the meson and baryon produces in the HERA-II data.

The tracking information from the Micro Vertex Detector (MVD) was used to observe the effect on the strange particles production when using this extra tracking information during the observation of  $\Lambda$  baryons and  $K_s^0$  mesons production at the ZEUS detector, in addition to the Central Tracking Detector. In order to study the performance and the effect of MVD tracking information in the production of strange particles, the signal to background ratio were investigated. The signal to background ratio of  $\Lambda$ ,  $\bar{\Lambda}$ ,  $\Lambda + \bar{\Lambda}$  baryon and  $K_s^0$  meson has been measured and shown in Figure 4.1 and compared to MC prediction from ARIADNE. For Low  $Q^2$  DIS events, the background for the events with MVD cuts got the small value of background to signal ratio compared to the mass plot without MVD cut and for the High  $Q$  DIS events, cuts on MVD give improvements for both meson and baryon production.

The signal to background ratio in Table 4.1 shows that the number of particles produced after the MVD cuts applied was higher than the value before the cuts. It prove that the performance of using the MVD as the extra tracking information gives a higher number of strange particles production compared to the CTD only.

In conclusion, the MVD improves the tracking information and gives a good result to find tracks in addition to the CTD in ZEUS detector. The performance of MVD + CTD in tracking charged particle is better than the performance of CTD only. The number of strange particle produced with this additional MVD tracking information was higher than the previous CTD only tracking information. Micro Vertex Detector

(MVD) improves tracking resolution and allows us to reconstruct strange particles decay vertex.

KINEMATICS RANGES	PARTICLES	DATA	MVD + CTD	CTD
Low $Q^2$ DIS	$\Lambda + \bar{\Lambda}$	ZEUS 2003 & 2007	$5.01 \pm 0.25$	$3.73 \pm 0.10$
		ARIADNE	$7.30 \pm 0.20$	$4.76 \pm 0.06$
	$\Lambda$	ZEUS 2003 & 2007	$6.67 \pm 0.42$	$4.66 \pm 0.16$
		ARIADNE	$7.08 \pm 0.27$	$4.84 \pm 0.08$
	$\bar{\Lambda}$	ZEUS 2003 & 2007	$5.73 \pm 0.39$	$4.70 \pm 0.16$
		ARIADNE	$7.79 \pm 0.30$	$4.69 \pm 0.08$
	$K_s^0$	ZEUS 2003 & 2007	$10.77 \pm 0.31$	$8.78 \pm 0.12$
		ARIADNE	$13.69 \pm 0.21$	$11.21 \pm 0.07$
High $Q^2$ DIS	$\Lambda + \bar{\Lambda}$	ZEUS 2003 & 2007	$3.06 \pm 0.30$	$2.26 \pm 0.10$
		ARIADNE	$4.91 \pm 0.25$	$2.89 \pm 0.06$
	$\Lambda$	ZEUS 2003 & 2007	$3.45 \pm 0.44$	$2.57 \pm 0.16$
		ARIADNE	$4.88 \pm 0.33$	$3.00 \pm 0.09$
	$\bar{\Lambda}$	ZEUS 2003 & 2007	$2.90 \pm 0.41$	$2.06 \pm 0.13$
		ARIADNE	$5.55 \pm 0.39$	$2.80 \pm 0.09$
	$K_s^0$	ZEUS 2003 & 2007	$16.15 \pm 0.65$	$7.26 \pm 0.16$
		ARIADNE	$10.40 \pm 0.27$	$8.61 \pm 0.09$

**Table 4.1:** The signal to background ratio for the MVD+CTD compared to the CTD. The performance of the MVD+CTD detector is better than the CTD only detector.

The particle rapidity correlations can be used to study the local quantum number conservation during the hadronization process [28]. Measurements of the rapidity correlations between  $\Lambda\bar{\Lambda}$  pairs provide good test of baryon production in fragmentation models. Models of baryon formation in the fragmentation process, such as “di-quarks” and “popcorn” models, predict different baryon-antibaryon correlations [24].

Baryon Antibaryon correlation in Deep Inelastic Scattering events were studied using the ZEUS 2003 & 2007 data with an integrated luminosity =  $4.60 \text{ pb}^{-1}$ . Table 6.18 shows the correlation between several pairs of  $\Lambda$  and  $\bar{\Lambda}$  in ZEUS 2003 & 2007 data while Table 6.19 for the ARIADNE data. Figure 6.16 shows the relation between

the number of lambda and the number of antilambda. There is a positive correlation between these two particles.

Figure 6.17 shows the  $\Lambda\bar{\Lambda}$  rapidity distribution for the Deep Inelastic Scattering events. The peak near to 0 rapidity difference shows us at the interaction point during the collision,  $\Lambda$  and  $\bar{\Lambda}$  tends to produced close to each other. Correlation happened when the hadrons are expected to be produced close in rapidity if they share the same string break-up. There is symmetry between the data and the MC. The data agree with the popcorn model from ARIADNE, which uses the Lund string model for the hadronization process.

In conclusion, results clearly show positive correlation between baryon and its antiparticle, antibaryon. In the case of strangeness, the strange particle and its corresponding anti-strange particles proved to be produced “close” to each other within the event. The data agree with the popcorn model from ARIADNE, which uses the Lund string model for the hadronization process. Correlation happened when the hadrons are expected to be produced close in rapidity if they share the same string break-up.

# BIBLIOGRAPHY

- [1] A. De Angelis, CERN-PPE-95-135 (and references herein), presented at the 1995 EPS-HEP meeting, Brussels, Belgium.
- [2] ALEPH collaboration, EPS-422, presented at the 1995 EPS-HEP meeting, Brussels, Belgium.
- [3] A. Kwiatkowski, H. Spiesberger, and H.J. Mohring, *Comp. Phys. Commun.* **69** (1992) 155; H. Spiesberger, *HERACLES – An Event Generator for ep Interactions at HERA Including Radiative Process (Version 4.6)*, 1996, available on <http://www.desy.de/~hspiesb/heracles.html>
- [4] A. Polini et al., *Nucl. Inst. Meth.***A 581**, 656 (2007).
- [5] Available on <http://www-zeus.desy.de/physics/lumi/>.
- [6] B. Anderson, G. Gustafson, G. Ingelman, T. Sjostrand, *Phys. Rep.* **97** (1983) 31
- [7] B. Andersson, G. Gustafson, T. Sjostrand, *Nucl. Phys.* **B187** (1982) 45  
B. Andersson, G. Gustafson, G. Ingelman, T. Sjostrand, *Z. Phys.* **C13** (1982) 361
- [8] B. Andersson, G. Gustafson, T. Sjostrand, *Phys. Scripta* **32** (1985) 574
- [9] B. Foster et al., *The performance of the ZEUS central tracking detector z-by-Timing electronics in a transputer based data acquisition system*, *Nucl. Phys. Proc. Suppl.* **B 32**(1993) 181.
- [10] B.Foster, *ZEUS AT HERA II*, DIS01'LANL: submitted to World Scientific on 7<sup>th</sup> February 2008
- [11] Chuanlei Liu et al., *Neutral Strangeness Production with the ZEUS Detector at HERA*, (2007).
- [12] F. Jacquet and A. Blondel, *Proceeding of the Study for an ep Facility for Europe*,  
U. Amaldi(ed.), p. 391, Hamburg, Germany(1979). Also in preprint DESY 79/48
- [13] Frank Close, *Particle Physics: A Very Short Introduction [OXFORD]*.
- [14] G.F Hartner et al., *VCTRAK Briefing: Program and Math*, ZEUS-Note 98-058
- [15] G. Ingelman, A. Edin, and J. Rathsmann, *Comp. Phys. Commun.* **101** (1997) 108.

- [16] Halina Abramowicz , Allen Caldwell, *HERA Collider Physics*
- [17] H. Abramowicz, A. Caldwell and R. Sinkus, Nucl. Inst. Meth.**A 365**, 508 (1995).
- [18] High Energy Physics-Experiment (hep-ex), *QCD Physics with ZEUS and H1 at HERA*, *Mod.Phys.Lett.A22:317-332,2007*
- [19] J.D. Bjorken, *Proceedings 3<sup>rd</sup> International Conference on Electron and Photon Interactions, Stanford, (1967)*, Phys. Rev. 185 (1969) 1975 (with E.A Paschos)
- [20] Julie Laines et al.,*Measurement of  $\Xi^-$  and  $\Sigma(1385)$  baryon production in deep inelastic scattering with the ZEUS detector at HERA,(2003).*
- [21] K..C Höger, *Proc. Workshop on Physics at HERA*, W. Buchmüller and G. Ingelman (eds), Vol. 1, p. 43. Hamburg, Germany, DESY (1992)
- [22] K. Charchula, G.A. Schuler and H. Spiesberger, Comp. Phys. Commun. **81** (1994) 381; H. Spiesberger, *DJANGO6 version 2.4 – A Monte Carlo Generator for Deep Inelastic Lepton Proton Scattering Including QED and QCD Radiative Effects*, 1996, available on <http://www.desy.de/~hspiesb/django6.html>
- [23] L. Lonnblad, Comp. Phys. Commun. **71** (1992) 15.
- [24] Michael T. Ronan et al., *Meson and Baryon Correlation Studies Using the PEP-TPC/2 $\gamma$  Facility*, CA 94720
- [25] N. Coppola, B. Kahle, and F. Karstens, Member, IEEE “*Charm Particle Finders with the ZEUS Micro-Vertex Detector*”, IEE Transactions on Nuclear Science, Vol. 54, No. 5, October 2007
- [26] N. Harnew et al., Nucl. Inst. Meth.**A 279**, 290 (1989);  
B. Foster et al., Nucl. Phys. Proc. Suppl. **B 32**, 181 (1993);  
B. Foster et al., Nucl. Inst. Meth.**A 338**, 254 (1994).
- [27] N. Harnew et al.,*Vertex triggering using time difference measurements in the ZEUS central tracking detector*, Nucl. Instrum.Meth.**A 279** (1989) 290 [SPIRES].
- [28] OPAL Collab., P.D. Acton et al., *Evidence for Chain-Like Production of Strange Baryon Pairs In Jets*, Phys. Lett. **B 305**, 415 (1993)
- [29] Particle Data Group, S Eidelman et al., *Review of Particle Physics*, Phys. Lett. **B 592**, 1 (2004)
- [30] Particle DataGroup, S. Eidelman et al., *Review of Particle Physics*, Phys. Lett. **B 592**, 1 (2004)
- [31] P. Eden, G. Gustafson, *Baryon Production in the String Fragmentation Picture*, LU TP 96-20, June 1996,available on arXiv:hep-ph/9606454v1
- [32] P.Hansson, KTH et al., *The Parton Model*, November 18, 2004
- [33] R. Brun et al., CERN-DD/EE/84-1 (1987)

- [34] R. Clanner, *Test program for the ZEUS Calorimeter*, Nucl. Meth.Phys.A **265**, (1998) 211-209.
- [35] R.P. Feynman, *Phys. Rev. Lett.* **23** (1969) 1415
- [36] S. Bentvelsen, J. Engelen and P. Kooijman, *Proc. Workshop on Physics at HERA*, W. Buchmüller and G. Ingelman (eds), Vol. 1, p. 23. Hamburg, Germany, DESY (1992)
- [37] SLD collaboration, SLAC-PUB-95-6920, presented at the 1995 EPS-HEP meeting, Brussels, Belgium.
- [38] S. Sjostrand, *Comp. Phys. Commun.* **39** (1986) 347; S. Sjostrand and M. Bengtsson, *Comp. Phys. Commun.* **43** (1987) 367; S. Sjostrand, *Comp. Phys. Commun.* **82** (1994) 74.
- [39] S.T. Boogert, “Photoproduction of  $K_s^0$  mesons and  $\Lambda$  baryons in electron proton collisions at ZEUS”, DPhil thesis, Oxford University, 2002 ← CHAPTER 4
- [40] TPC collaboration, H. Aihara et al., *Phys. Rev. Lett.* **55** (1985) 1047
- [41] TPC/Two-Gamma Collaboration, H. Aihara et al., *Study of Baryon Correlations in  $e^+e^-$  Annihilation at 29 GeV*, Physical Review Letters, Volume 57, Number 25 (1986)
- [42] ZEUS Coll., “A Microvertex Detector for ZEUS”, ZEUS note 1997-2006, 1997.
- [43] ZEUS Collaboration, B. Foster et al., *The design and construction of the ZEUS central tracking detector*, *Nucl. Instrum.Meth.A* **338** (1994) 254 [SPIRES].
- [44] ZEUS Collaboration, edited by U. Holm, *The ZEUS Detector*. Status report (unpublished), DESY (1993), available on <http://www-zeus.desy.de/bluebook/bluebook.html>
- [45] ZEUS Collaboration, U. Holm(ed.), *The ZEUS Detector. Status report (unpublished)*, DESY, 1993, available at <http://www-zeus.desy.de/bluebook/bluebook.html>
- [46] ZEUS Coll., U. Schneekloth (ed), *The HERA Luminosity Upgrade*, DESY-HERA 98-05, 1998.
- [47] Franck Wilczek, *QCD Made Simple*, Physics Today (August 2000)
- [48] Bo Andersson, Haiming Hu, *Few-Body States in Lund String Fragmentation Model*. Available on arXiv:hep-ph/9910285v1 (8 Oct 1999)
- [49] Andrew C. Cottrell, Lincoln College, Oxford, *Strange Particle Production at the ZEUS Detector*. 2005
- [50] Available on <http://www.desy.de/~heramc/mclist.html>
- [51] ZEUS Collaboration; J. Breitweg et al. *Measurement of High  $Q^2$  Charged-Current  $e^+p$  Deep Inelastic Scattering Cross Sections at HERA*. DESY 99-059 (July 1999)

- [52] Torbjorn Sjostrand et al. *PYTHIA 6.4 physics and manual*. JHEP05 (2006) 026
- [53] PETER J. BUSSEY. *QCD Physics with ZEUS and H1 at HERA*. Mod. Phys. Lett. A, **22**, 317 (2007)
- [54] S. Chekanov. *Measurement of  $K_s^0$ ,  $\Lambda$  and  $\bar{\Lambda}$  production at HERA*. The European Physical Journal C, June 2007, Volume 51, Issue 1, 1-23
- [55] ZEUS Collaboration, *High- $Q^2$  neutral current cross sections in  $e^+p$  deep inelastic scattering at  $\sqrt{s} = 318$  GeV*. DESY-03-214, December 2003
- [56] The SLD Collaboration, *A Study of Correlations between Identified Charged Hadrons in Hadronic  $Z^0$  Decays*, SLAC-PUB-9288, July 2002
- [57] Available on <http://www-zeus.desy.de/components/offline/>
- [58] Available on [http://www-zeus.desy.de/ZEUS\\_ONLY/analysis/orange/](http://www-zeus.desy.de/ZEUS_ONLY/analysis/orange/)